The Rotation Curve of the Brightest SMM Galaxy Behind the Bullet Cluster: a.k.a the Cosmic Seagull

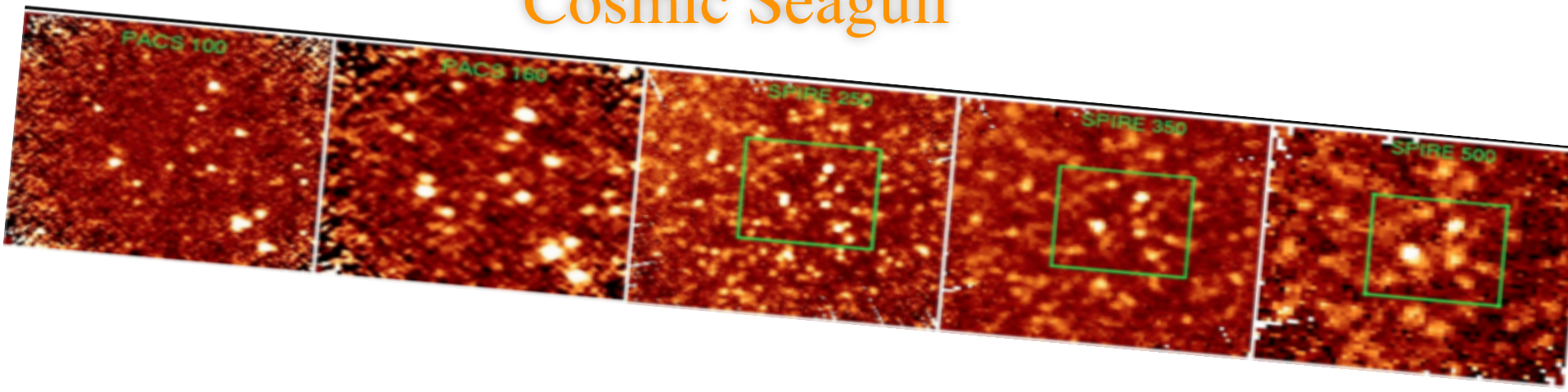

Dr. Omar López-Cruz

Coordinación de Astrofísica,

Instituto Nacional de Astrofísica, Optica y Electrónica (INAOE)

omarlx@inaoep.mx

Some Definitions

$$1\ \mathrm{Mpc} = 3.0857 \times 10^{22}\ \mathrm{m}$$

Friedman-Lamaître-Robison-Walker Metric

FLRW metric

$$ds^2 = -dt^2 + a(t)\left(\frac{dr^2}{1-kr} + r^2 d\theta^2 + r^2 \sin^2\theta d\phi^2\right)$$

$$z = \frac{a(t_o)}{a(t_e)} = \frac{\lambda_o}{\lambda_e} \sim \frac{v}{c}$$

$v = H_o d$ Hubble-Lamaître Law

$H_o = 100h\ \mathrm{km\,s^{-1}Mpc^{-1}};\ h = 0.7$

$$\Omega_M = \frac{8\pi G\rho_0}{3H_o^2} = 0.3$$

$$\Omega_\Lambda = \frac{\Lambda_{vac}c^2}{3H_o^2} = 0.7$$

Zwicky, 1937, Apj, 86, 217

"The observation of such gravitational lens effects promises to furnish us with the simplest and most accurate determination of nebular masses. No thorough search for these effects has as yet been undertaken. It would seem, perhaps, that if the masses of field nebulae were, on the average, as great as the masses of cluster nebulae obtained in section iii, gravitational lens effects among nebulae should have been long since discovered. Until many plates of rich nebular fields taken under excellent conditions of seeing have been carefully examined it would be dangerous, however, to draw any definite conclusions."

Apparent deflection angle α

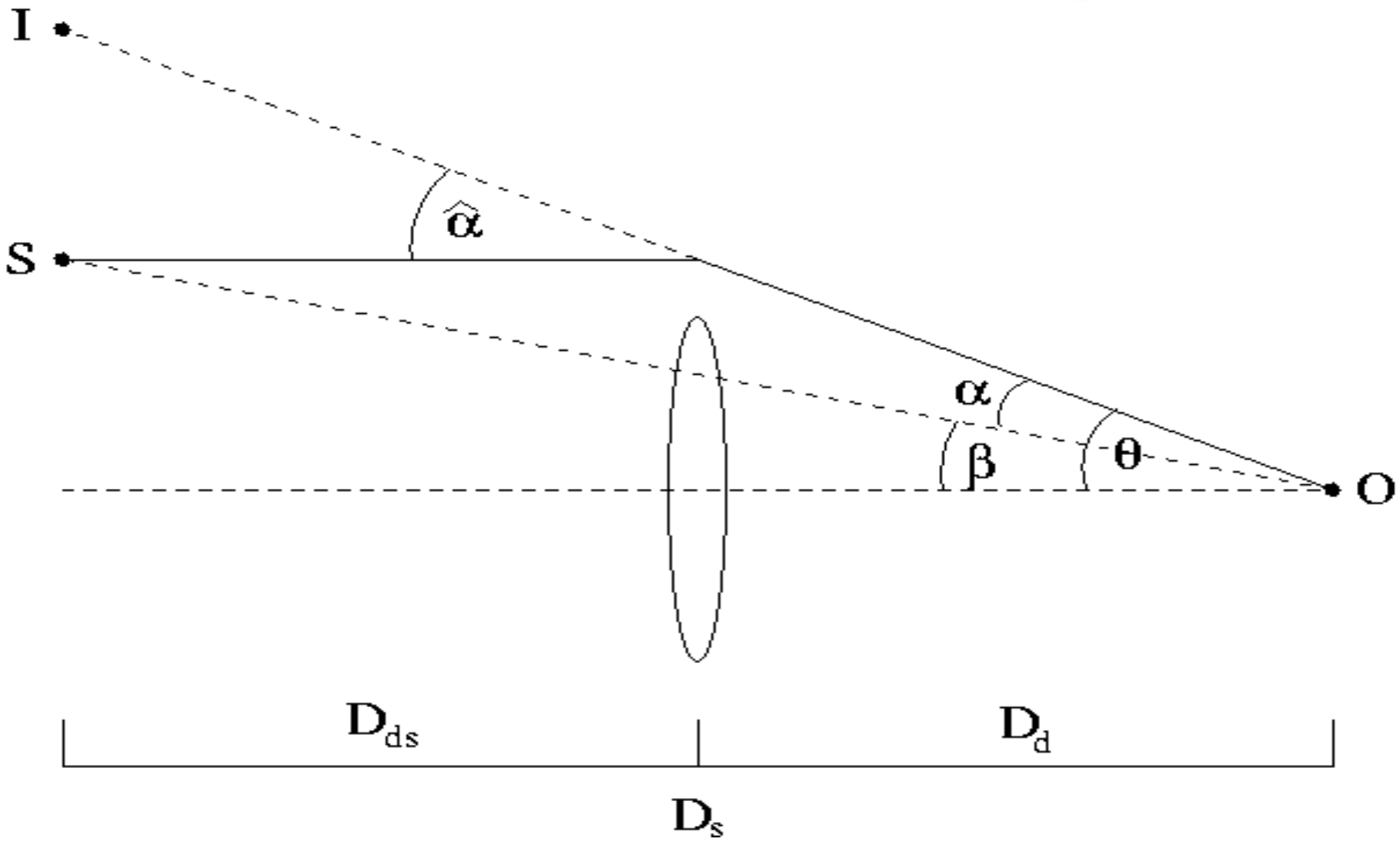

Lensing and Time Delays

- Images seen in directions perpendicular to the wavefronts

- Wavefronts from the same event in the object arrive at different times

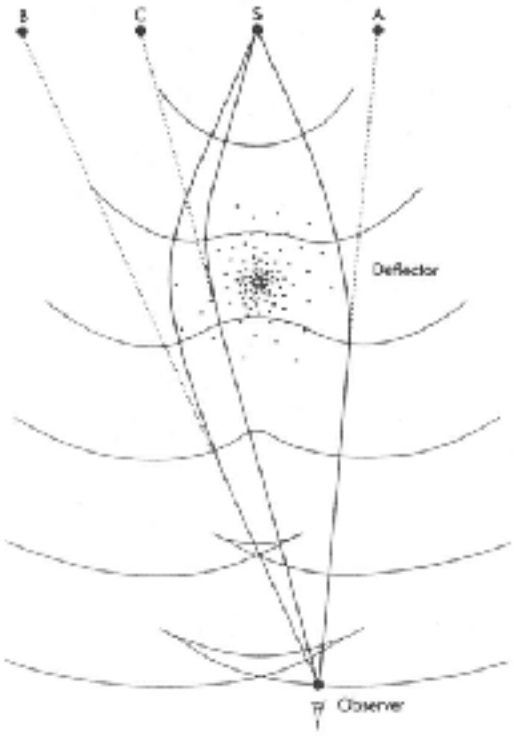

First Extragalactic Observations

- 1979 Walsh, Carswell, & Weyman serendipitously discovered the first multiple image quasar. Two quasar images at z=1.41, lens galaxy at z=0.36.
- Lynds & Petrosian (1986), Soucail et al. (1987) discovered giant luminous arcs in the cluster of galaxies A371.

Galaxy Cluster Abell 2218

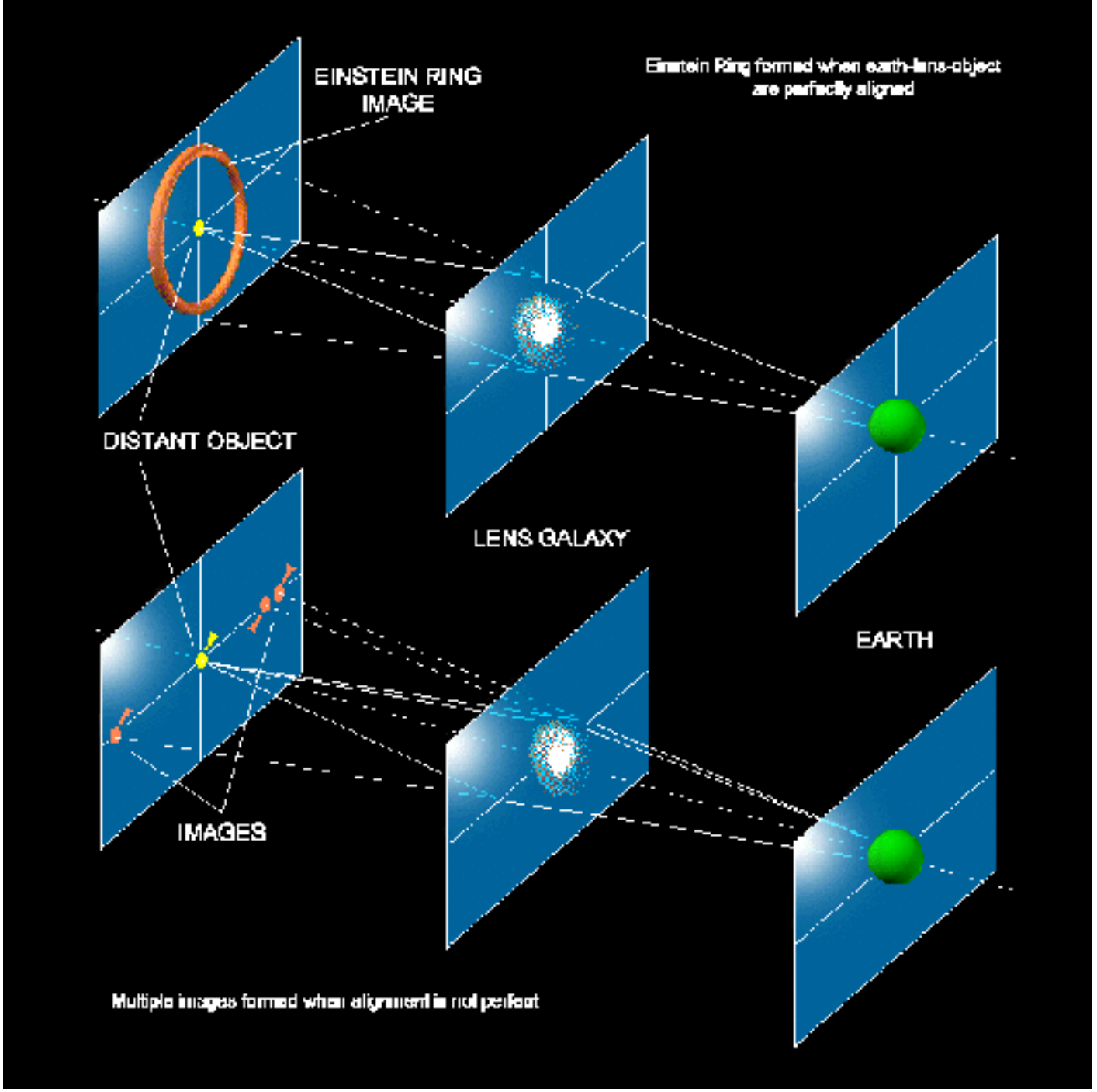
EINSTEIN RING
IMAGE
Einstein Ring formed when earth-lens-object are perfectly aligned
DISTANT OBJECT
LENS GALAXY
EARTH
IMAGES
Multiple images formed when alignment is not perfect

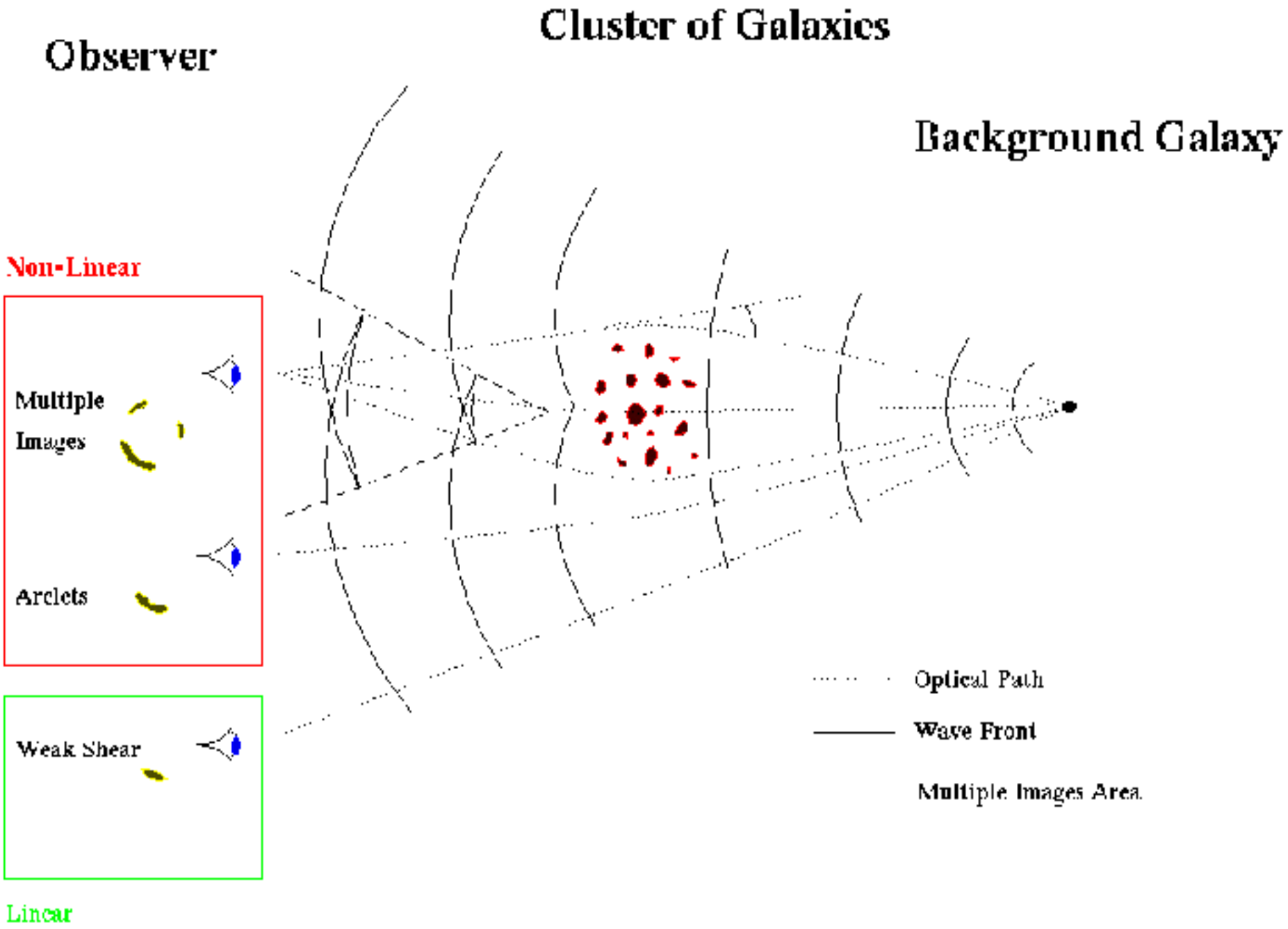
Observer
Cluster of Galaxies
Background Galaxy
Non-Linear
Multiple
Images
Arclets
Weak Shear
Linear
Optical Path
Wave Front
Multiple Images Area

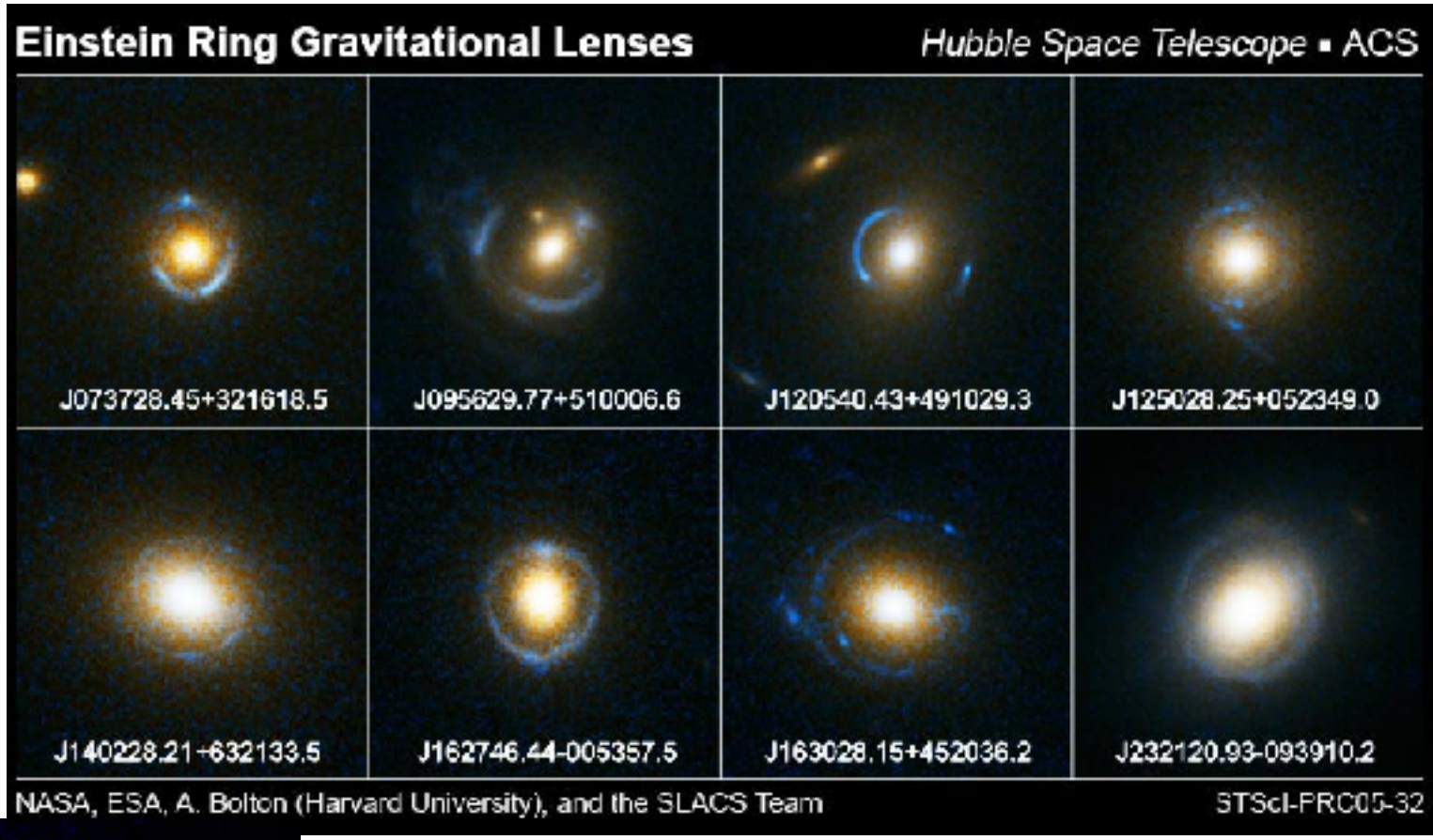
Einstein Ring Gravitational Lenses
Hubble Space Telescope ▪ ACS
J073728.45+321618.5
J095629.77+510006.6
J120540.43+491029.3
J125028.25+052349.0
J140228.21+632133.5
J162746.44-005357.5
J163028.15+452036.2
J232120.93-093910.2
NASA, ESA, A. Bolton (Harvard University), and the SLACS Team
STScI-PRC05-32

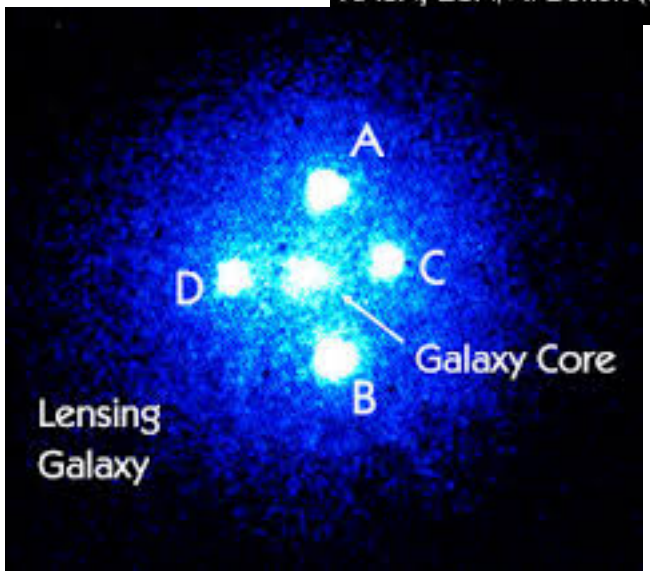
A
C
D
B
Galaxy Core
Lensing
Galaxy

A Gravitational Lens Analogy (see Refsdal & Surdej 1994)

$$n = \frac{\sin(i)}{\sin(r)} \simeq \frac{i}{r}$$

$$i = \epsilon(\xi) + r = \frac{4GM(\xi)}{c^2\,\xi}$$

$$\frac{d\Delta}{d\xi} = -r \rightarrow \frac{d\Delta}{d\xi} = \frac{-4GM(\xi)}{(n-1)c^2\xi}$$

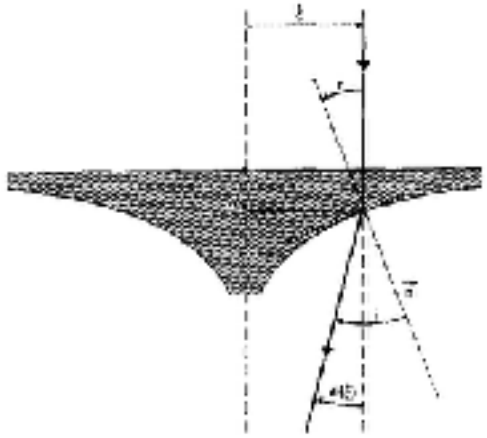

for a point $-$ mass lens we have $M(\xi) = M \rightarrow$

$$\Delta(\xi) = \Delta(\xi_0) + \frac{2R_{sc}}{n-1}\ln\left(\frac{\xi_0}{\xi}\right)$$

Lenses for Different Mass Distributions

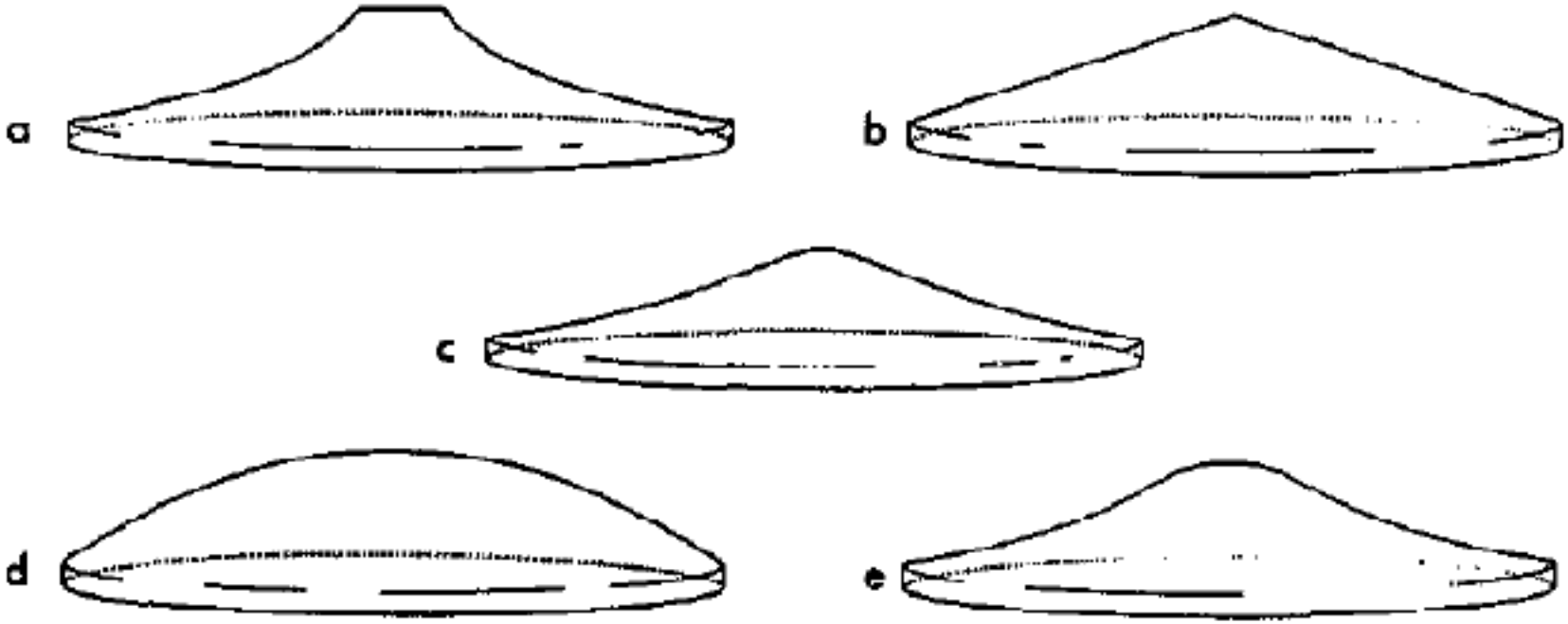

Figure 7. Several examples of axially symmetric optical lenses simulating the light deflection properties due to a point mass (*a*), an sis galaxy (*b*), a spiral galaxy (*c*), a uniform disk (*d*) and a truncated uniform disk of matter (*e*).

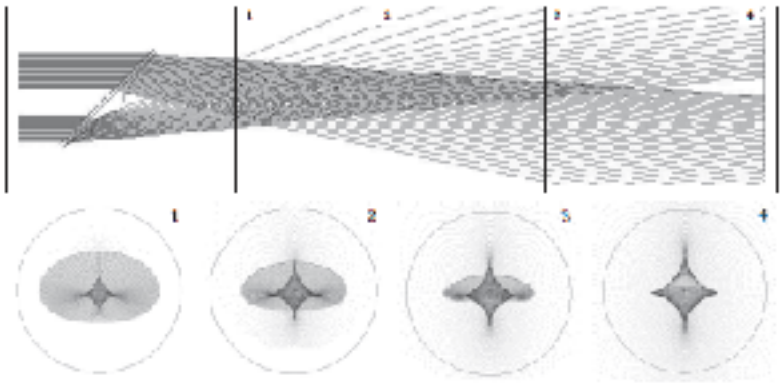

Figure 1.3: *Ray-tracing diagram for a non-symmetric point-mass lens produced with ZEMAX. The shape of the lens, given similar to the foot of a wine glass. The vertical lines indicate the positions of different planes with respect to the lens. The n each of these planes (perpendicular cuts of the 3D light ray intercalt between the lens and the observer) are included at igure.*

Zemax Modeling

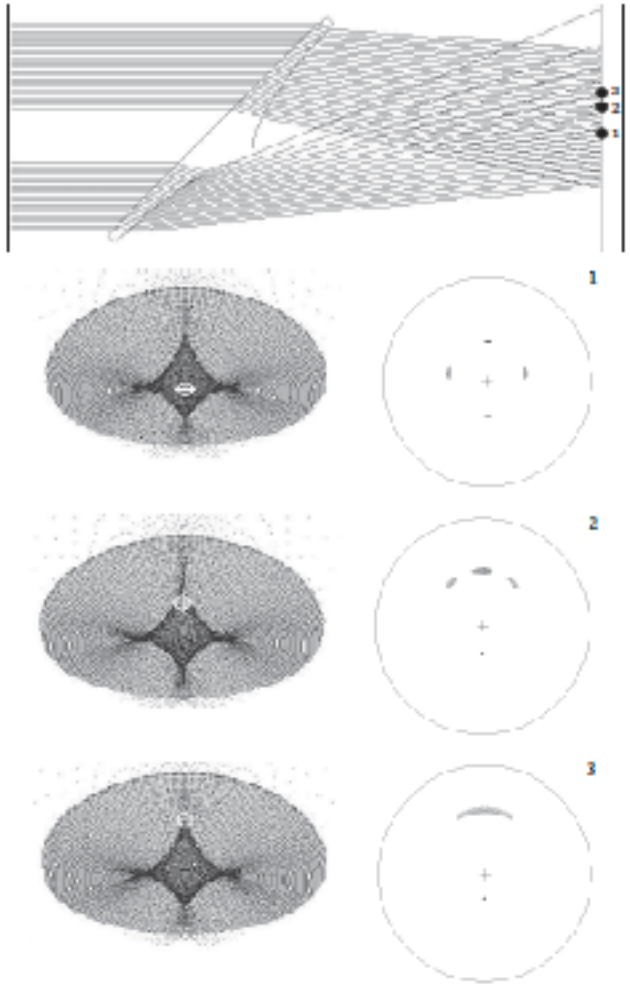

Figure 1.5 *Effect of the size and position of the observer with respect to the caustic pattern. The ray tracing diagram corresponds to the non-symmetric point-mass lens. The black dots indicate different positions of the observer with respect to the optical axis. The panels below indicate the observer size and position with respect to the caustic pattern (left) and the corresponding image configuration (right) for each black dot.*

The Optimal Gravitational Lens Telescope (OGLT)

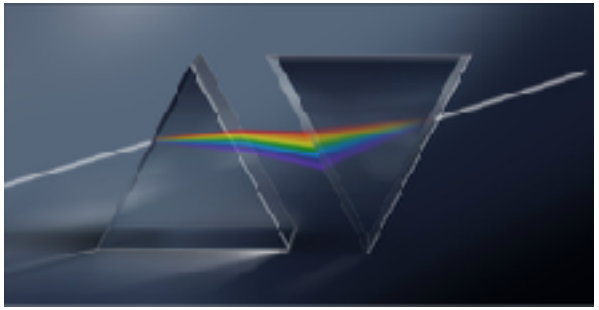

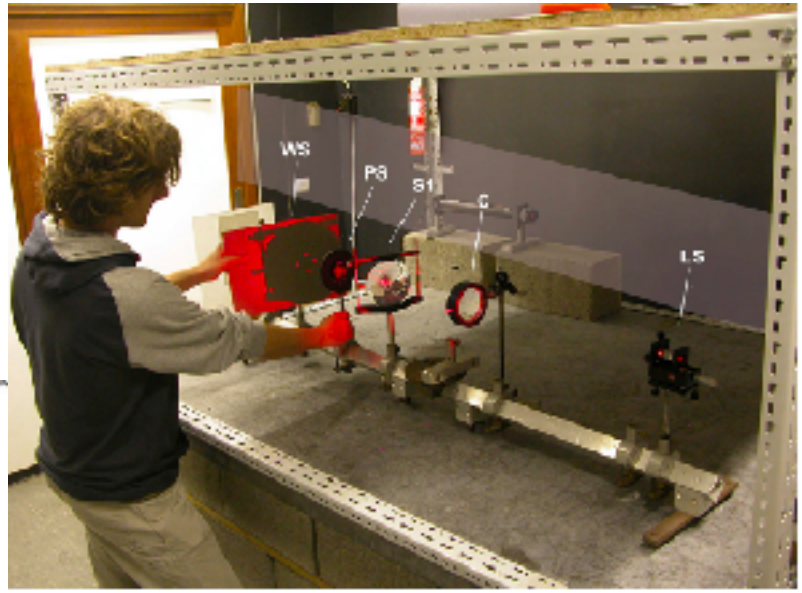

Surdej et al. 2010

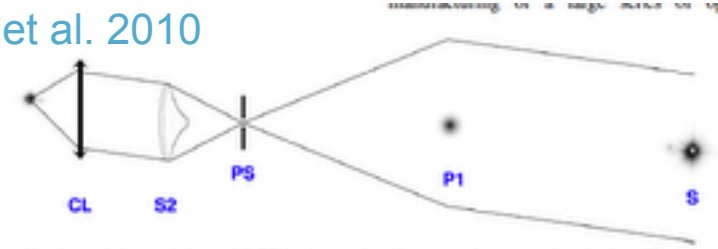

Figure 6. Same as Figure 4 but the small size cosmic lens at left (P2) has been replaced by an optical point mass lens simulator (S2) corresponding to the same mass. Since the separation between the two outgoing parallel beams of light rays is now reduced to several tens of centimeters, or even smaller, it is easy to place at left a classical converging lens (CL) so that a perfect, lens inverted, image of the distant source at right (S) is formed in its focal plane.
(A color version of this figure is available in the online journal.)

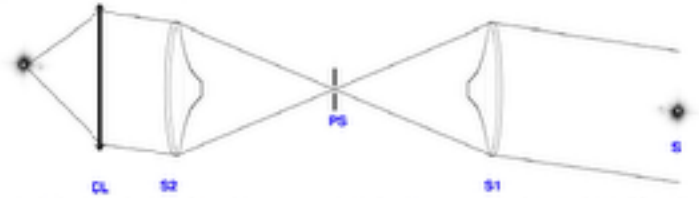

Figure 7. First point mass gravitational lens simulator (S1) at right produces a doubly imaged source as seen from the pinhole (PS), while the second lens simulator (S2) inverts the mirage into two parallel beams of light rays which are then focused at left by a classical converging lens (CL).
(A color version of this figure is available in the online journal.)

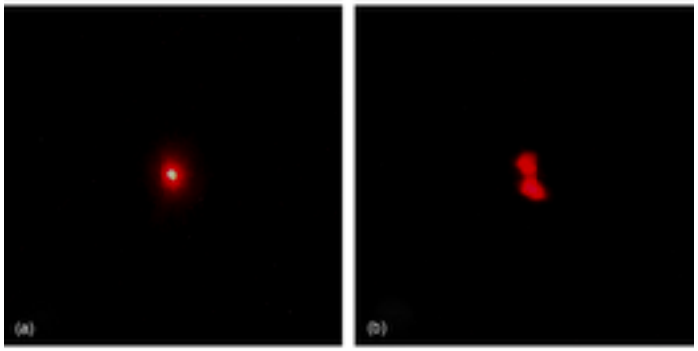

GTM as a Segmented Vortex Telescope could become an OGLT

Treviño, López-Cruz, & Chávez-Cerda,2013

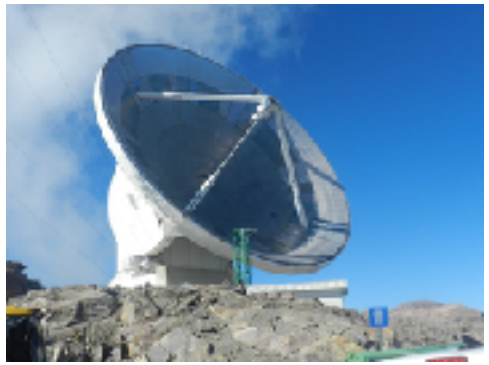

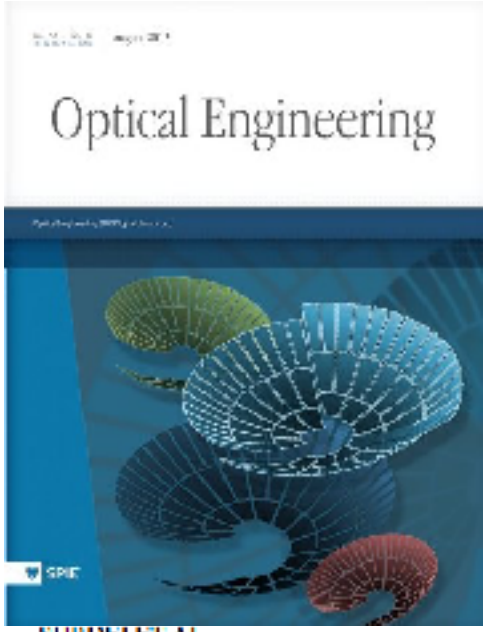

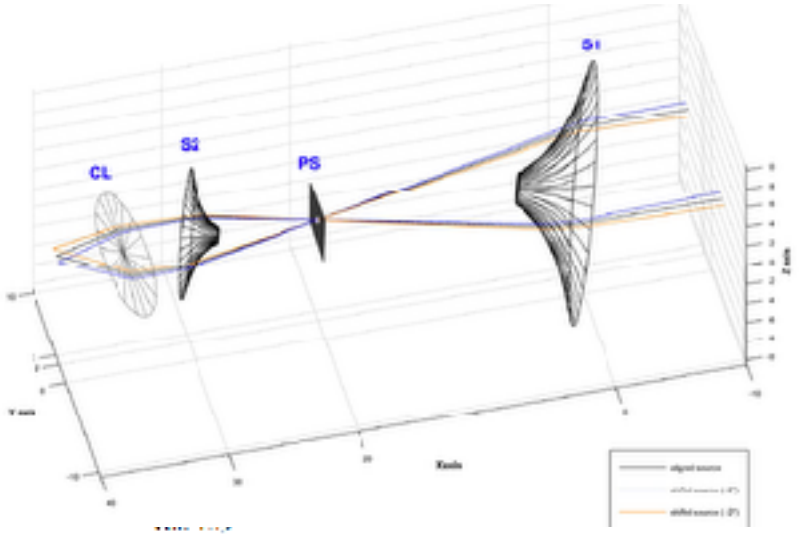

1940 SUROEJ ET AL.

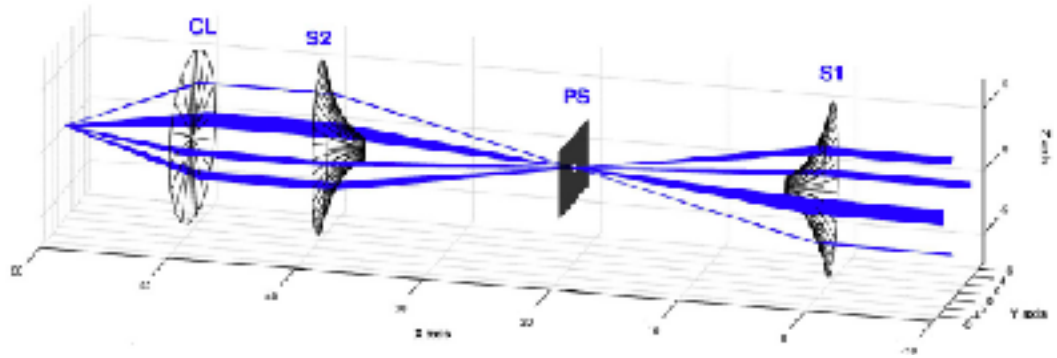

Gravitational Lensing by a Black Hole

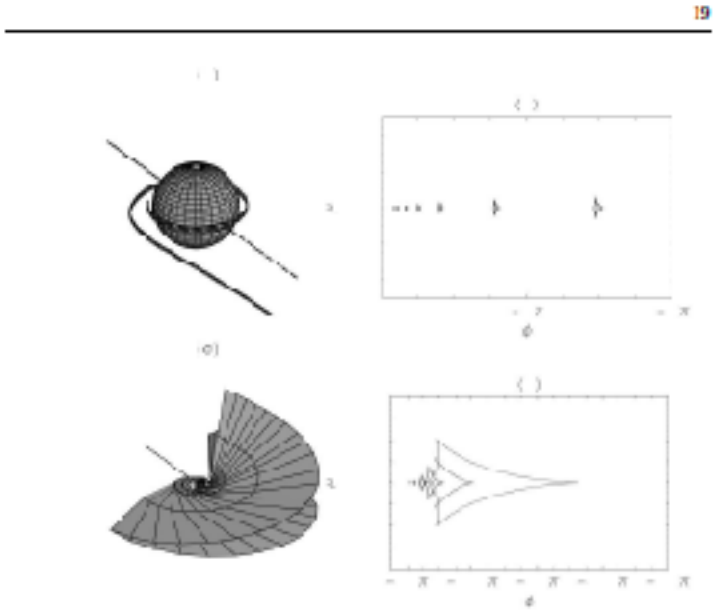

Fig. 7 (a) The primary caustic tube for $a = 0.9998M$ and $\mu_O = 0$ in a 3-dimensional representation, with pseudo-cartesian coordinates $x = r\sin\vartheta\cos\psi$, $y = r\sin\vartheta\sin\psi$, $z = r\cos\vartheta$. The spin axis is directed toward the top. The straight solid line indicates the direction towards the observer, whereas the dashed line points in the opposite direction. The primary caustic for a Schwarzschild black hole ($a = 0$) coincides with this dashed line. (b) Cross section of the same primary caustic at various distances. From left to right, the radial coordinate is $r = 5M, 4.5M, 4M, 3.5M, 3.3M, 1.92M, 1.42M, 1.23M$. (c) 3 dimensional picture of the second order caustic surface of an extremal Kerr black hole for an observer on the equatorial plane in the direction indicated by the solid line. The surface has been plotted for radial distances in the range $[2.2M, 20M]$. (d) Second order asymptotic caustic for an equatorial observer $\mu_o = 0$ and different values of the spin. From left to right, $a = 0.05M, 0.2M, 0.4M, 0.6M, 0.8M, 0.9998M$.

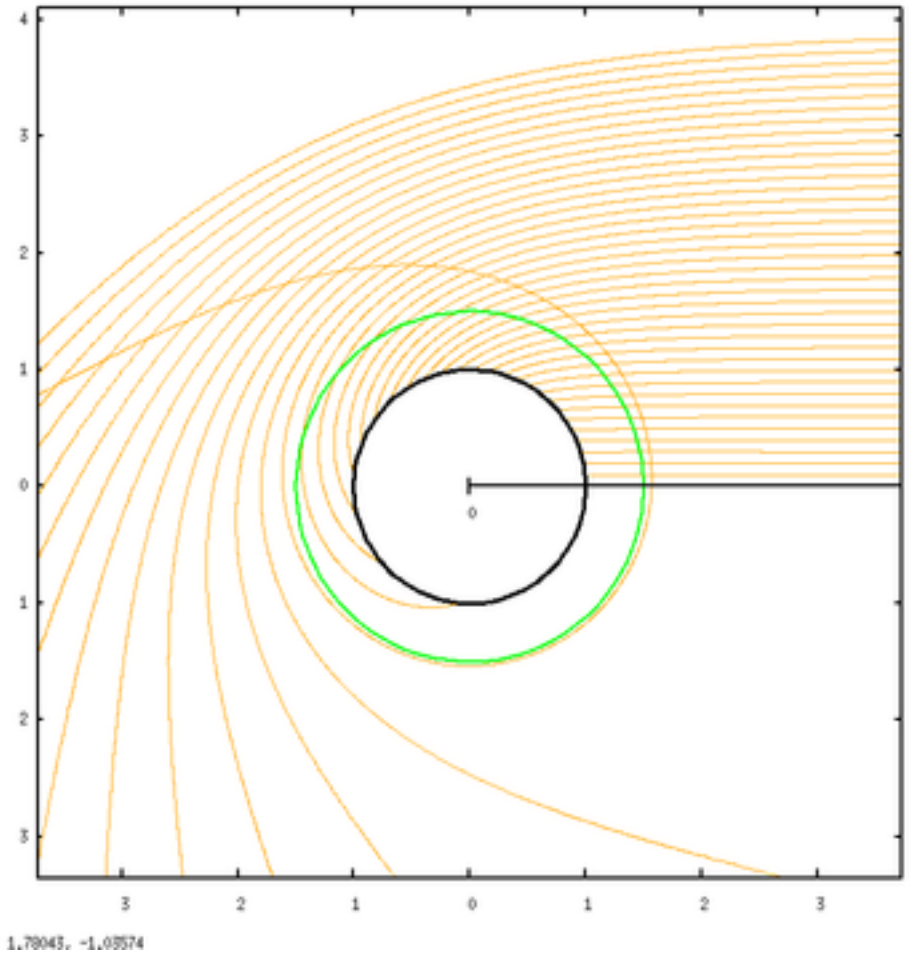

Can we push our analogy based on refractions?

Orbiting Rays of Light

What kind of refractive index is needed?

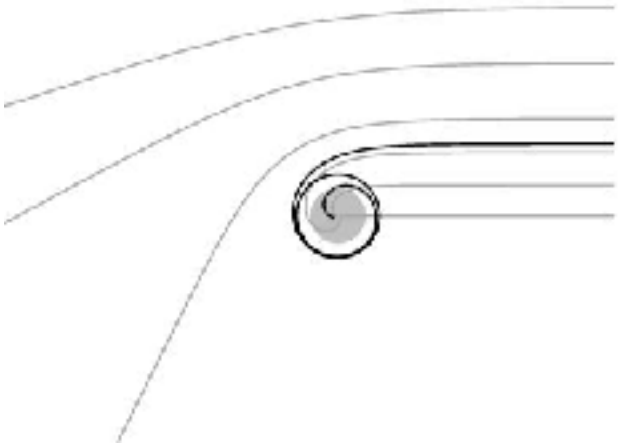

$$\frac{d}{ds}\left(n\frac{d\mathbf{r}}{ds}\right) = \nabla n \rightarrow$$

$$n(r) = \frac{constant}{r}$$

Caustic Network in the Universe

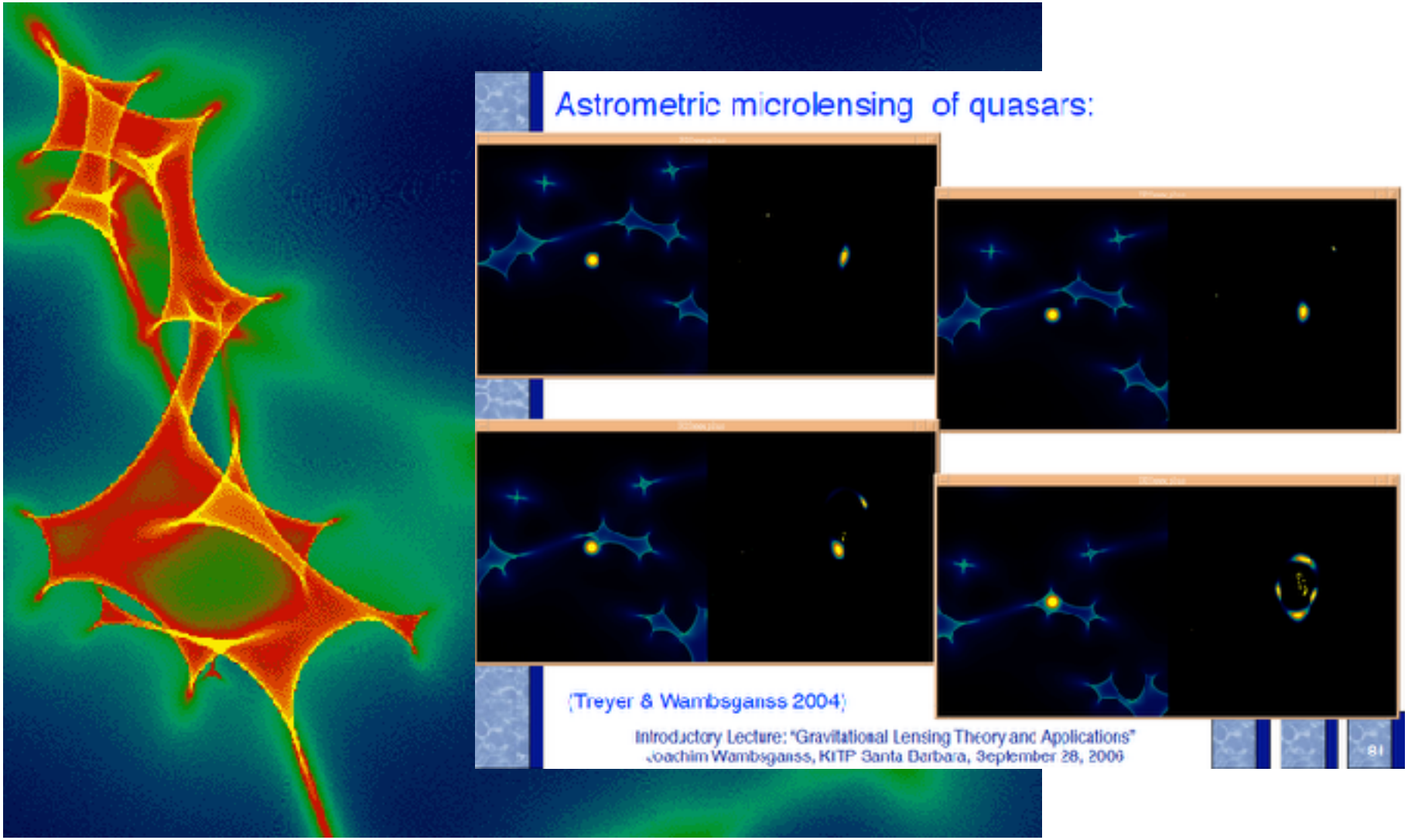

History

- Mysterious 'Giant arcs' in A370,Cl2244

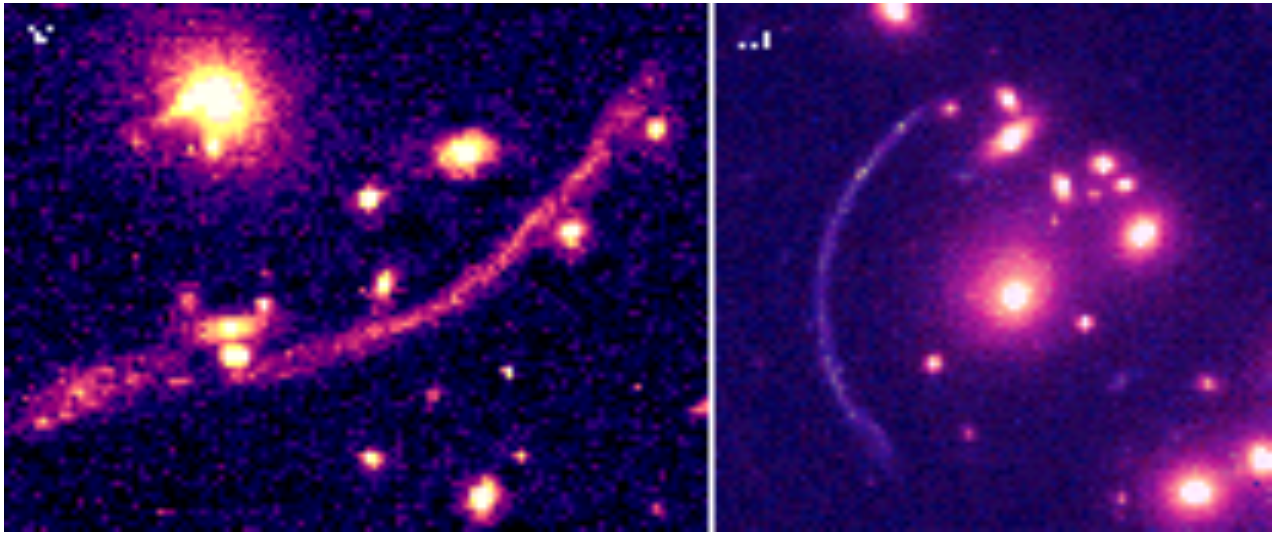

  - Paczynski suggests lensing
  - 1987 Fort et al. confirm. Spectroscopy.

- Clusters are more massive than expected

Historically: first source interpretation of a giant arc

CL2244

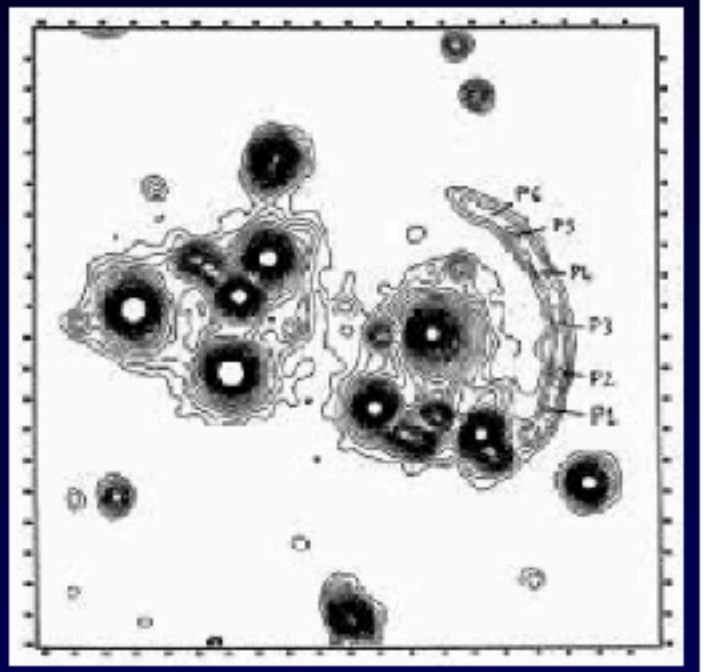

First spatially resolved source interpretation from the identification of bright clumps in a giant gravitational arc *Hammer et al. 1989*

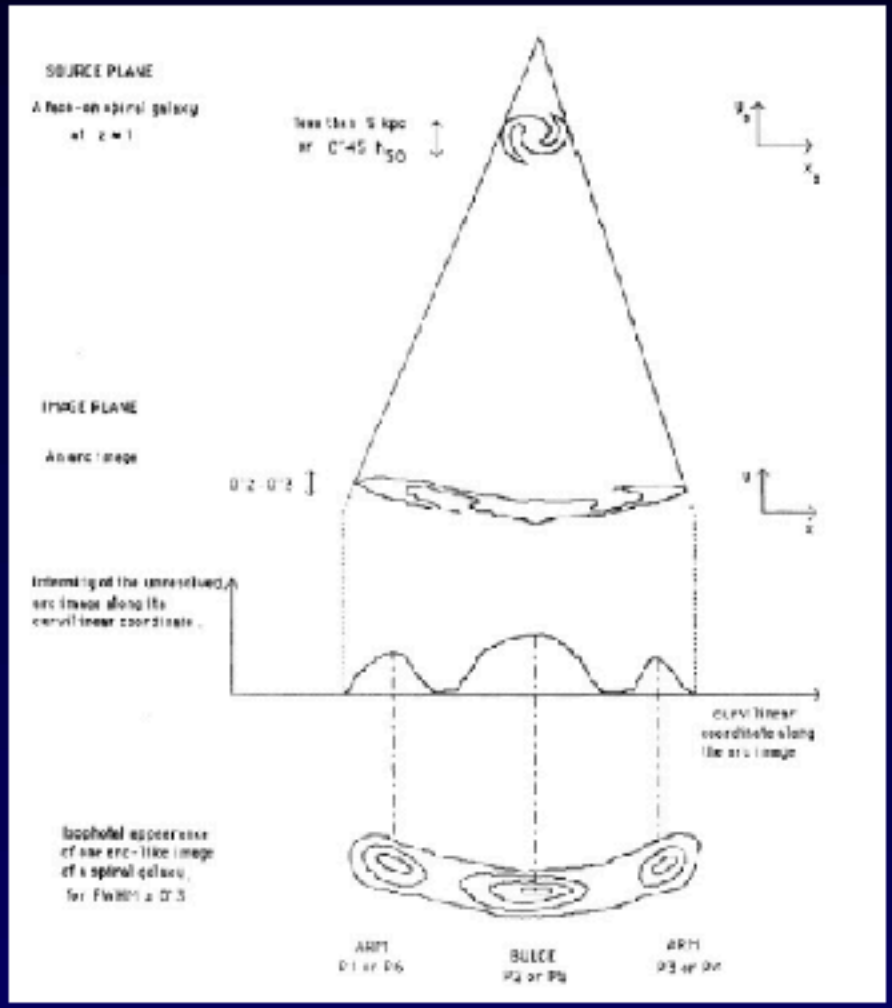

Hammer & Rigaut 1989

Advantages of magnification

$$\mu = \frac{1}{\det A} = \frac{1}{[(1-\kappa)^2 - \gamma^2]}$$

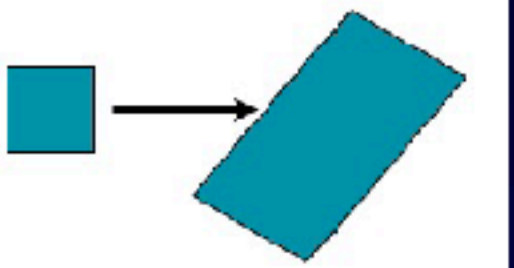

Magnification

- increase of the observed angular size: better spatial resolution in the intrinsic source.

- increase of total flux: better sensitivity.

The gain in resolution is anisotropic: along the shear direction it varies between $\sqrt{\mu}$ and μ.

Strong lensing and magnification effect

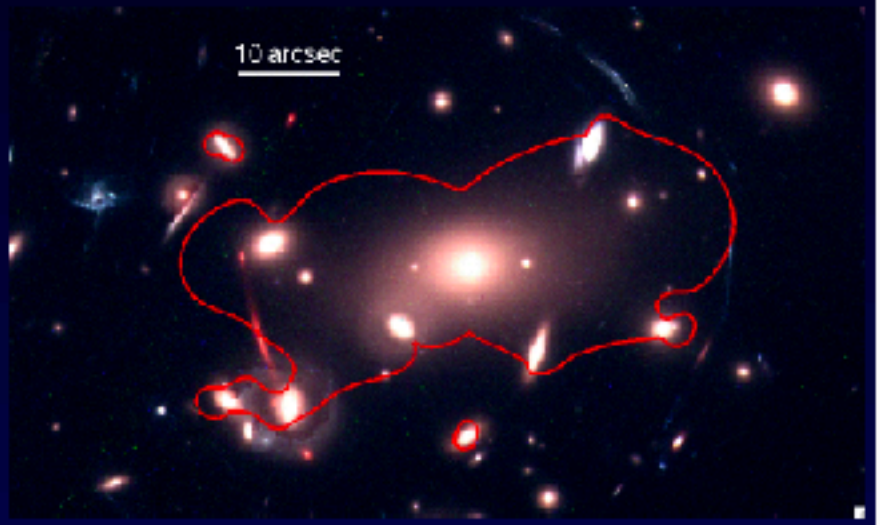

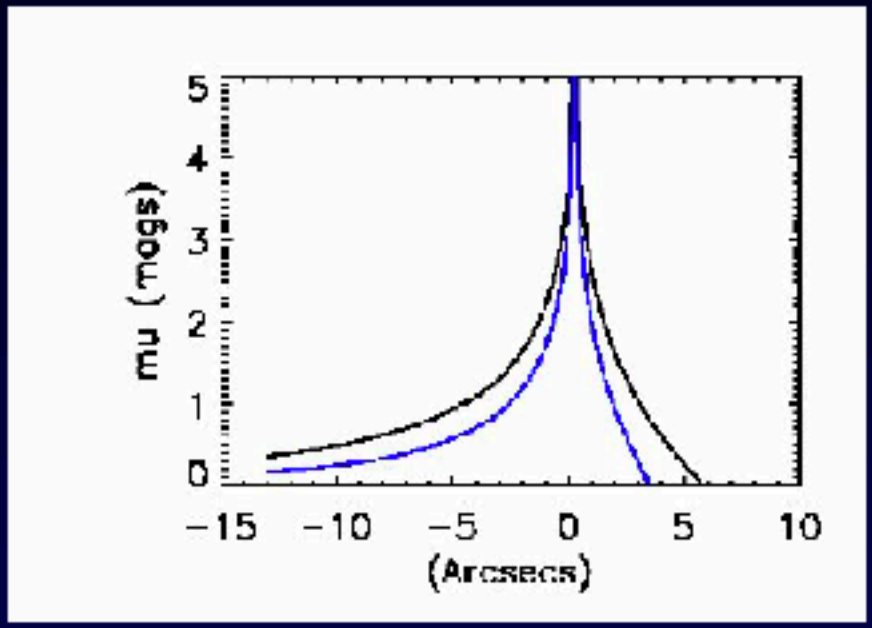

- Maximal magnification effect in the vicinity of the **critical lines**
- μ drops more quickly away from the critical line for more massive lenses / largest Einstein radii
- Cluster lenses provide the largest image plane area with a large magnification

Example of resolutions achieved

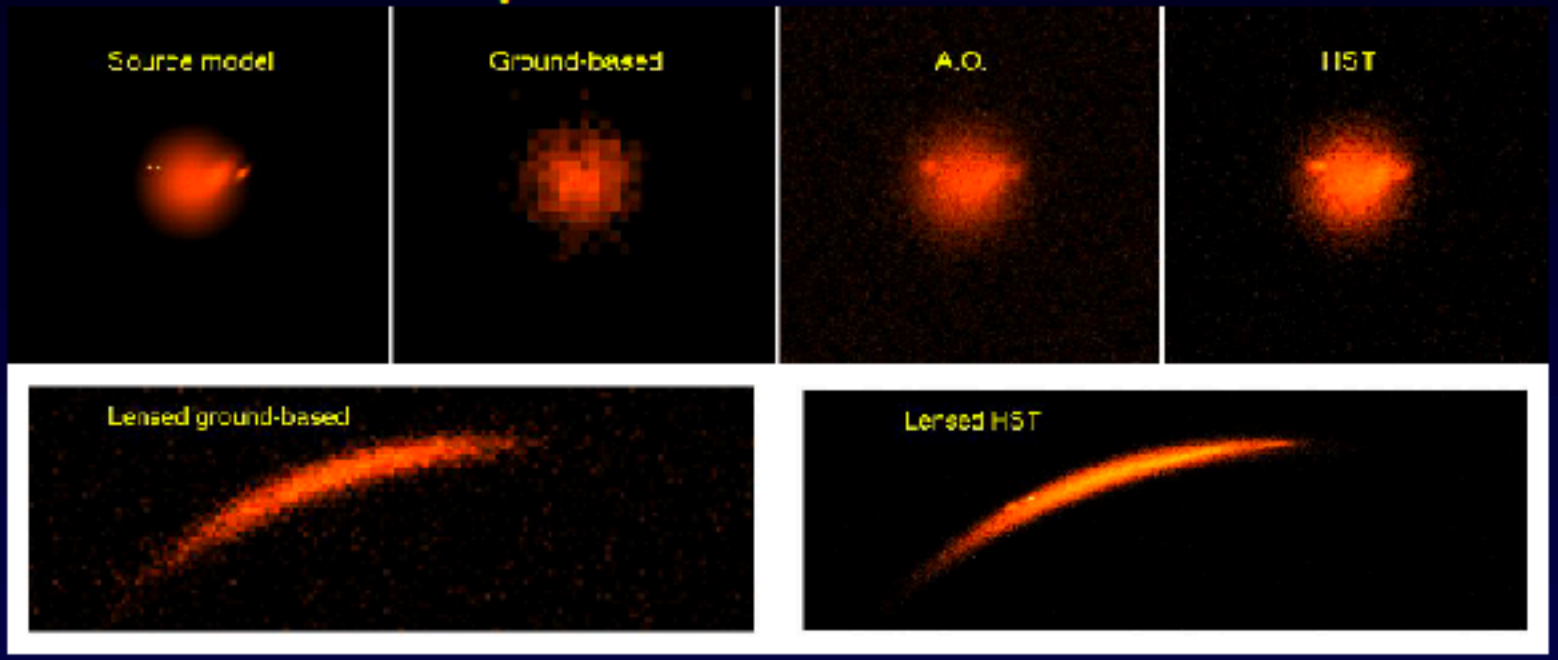

- Model of distant galaxy with multiple components and 2 star-forming regions separated by 500 pc.
- Only with the combination of lensing and high resolution imaging can we reach spatial resolutions $< 1kpc$ in distant galaxies.

Direct reconstruction

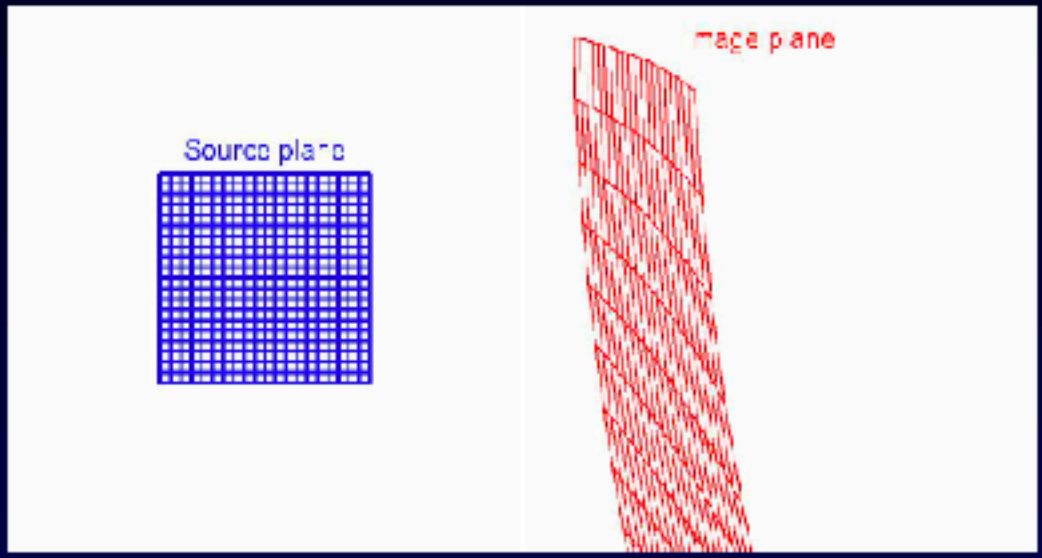

+ Straightforward calculation
+ No assumption on the source morphology

- Correlated source plane pixels at the highest resolution pixel grid
- Point Spread Function remains in the source plane

This technique gives useful results when the PSF is small (Adaptive Optics, Hubble images, good seeing) and when the image to reconstruct is isolated.

The Team

- Verónica Motta, Edo Ibar, Thomas Hughes, Diah Gunawan, Juan Magaña at Universidad de Valparaíso, Chile.
- Tomás Verdugo at IA-UNAM, Ensenada
- Mark Birkinshaw at Bristol University, UK
- Kathy Horellou and John H. Black at Chalmers University of Technology, Sweden
- Omar López-Cruz at INAOE

Science

- Initially we proposed to use APEX+LABOCA to map the pressure wave in the Bullet Cluster (1E 0657-56) (2008).
- Kathy Horellou and her team join us. They have proposed a similar project on APEX Swedish time.
- We were surprised to discovered 17 sub-millimeter galaxies (SMG) behind the Bullet Cluster, which at the time none of them had measured redshifts (2009).
- In this talk I present the results from our APEX+LABOCA observations and our follow-up observations on the brightest SMG, aka SMM J065837.6−555705 (SMM J0658), Cosmic Seagull using ATCA CABB (3mm and 7mm) and ALMA

The Bullet Cluster (1E 0657 -57) was discovered by Tucker et al. (1995) using *Einstein IPC*. Tucker et al. (1998) used ASCA data and derived T= 17 keV (5.2 X 10^8 K), it's one of the hottest known cluster. Established as a cluster-cluster merger by Tucker et al. (1998) using ROSAT. The most luminous synchrotron radio halo (Liang et al. 2000). Supersonic merger Mach=2-3 shock: v=4000-5000 km/s (Markevitch et al. 2002)

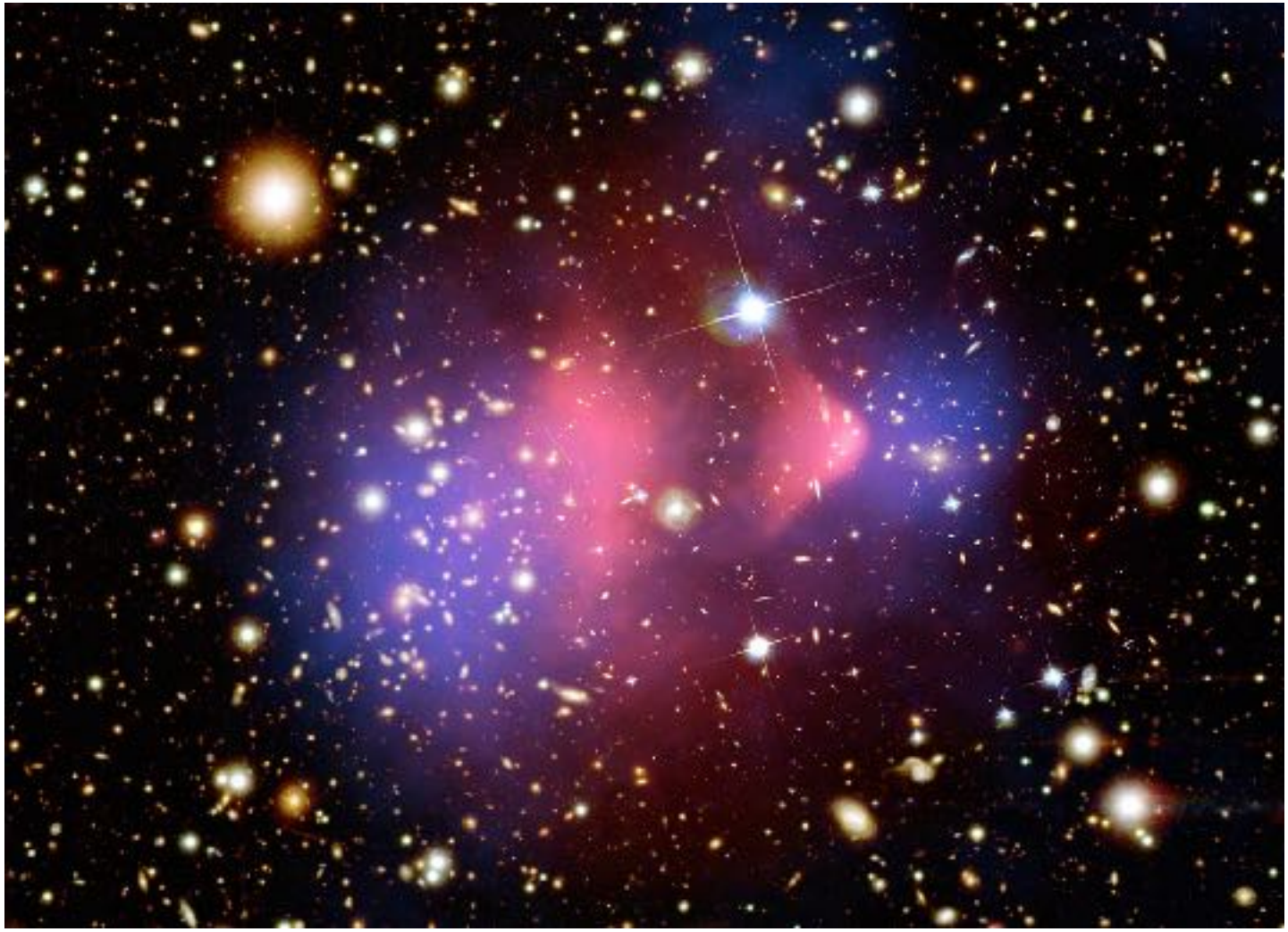

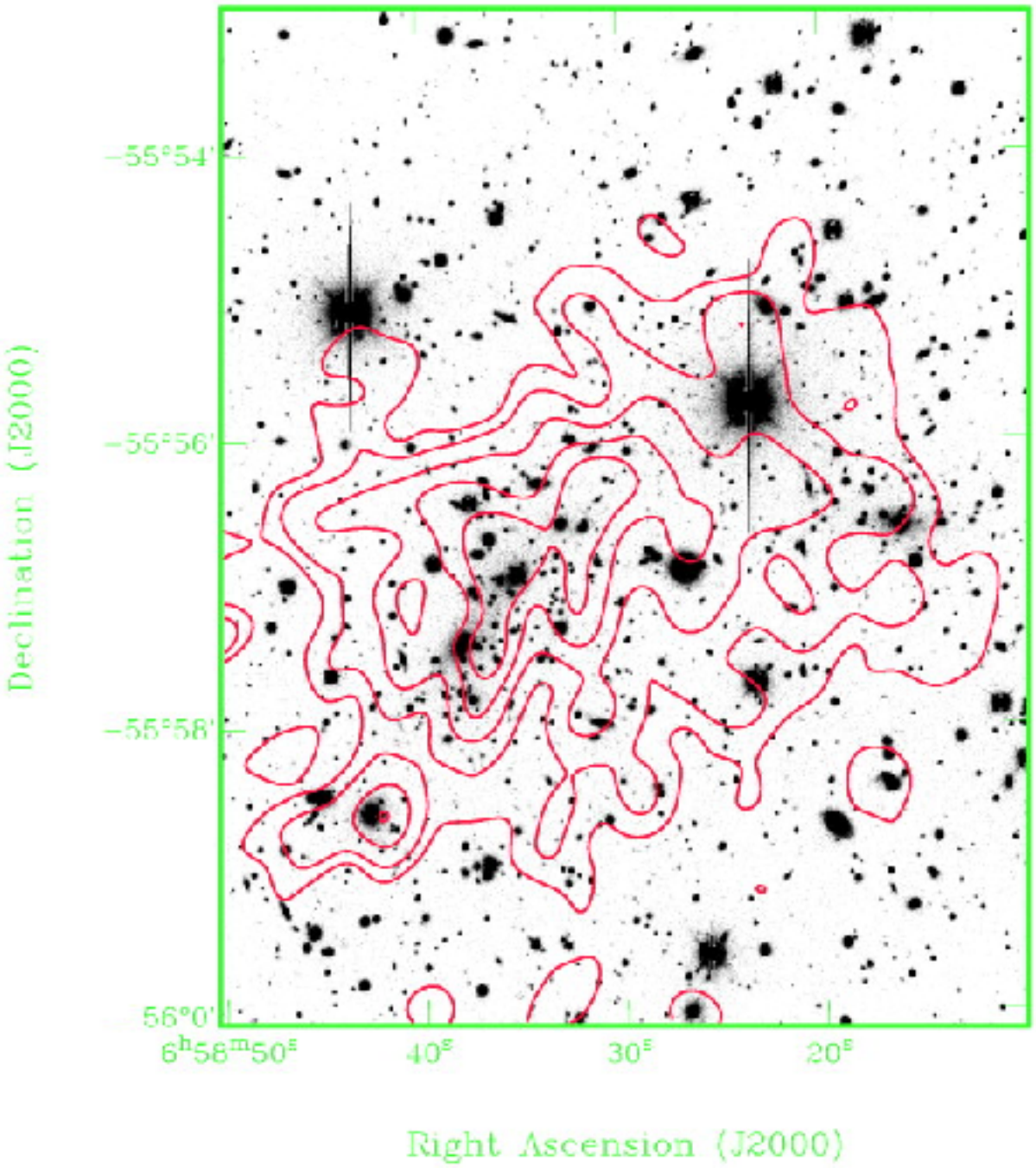

Liang et al. (2000)
1.3 GHz ATCA
observations

Physical Properties of the gas in the Bullet Cluster (Markevitch et al. ,2002)

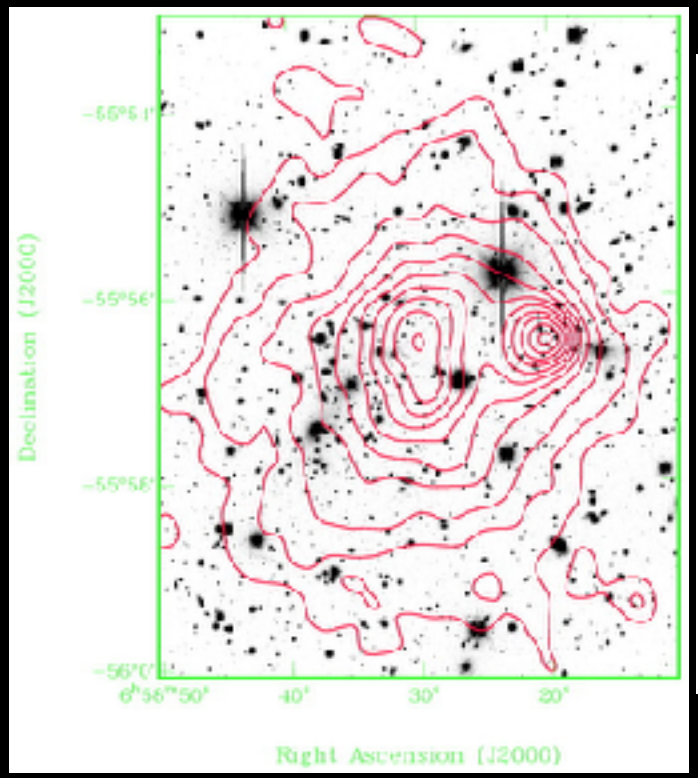

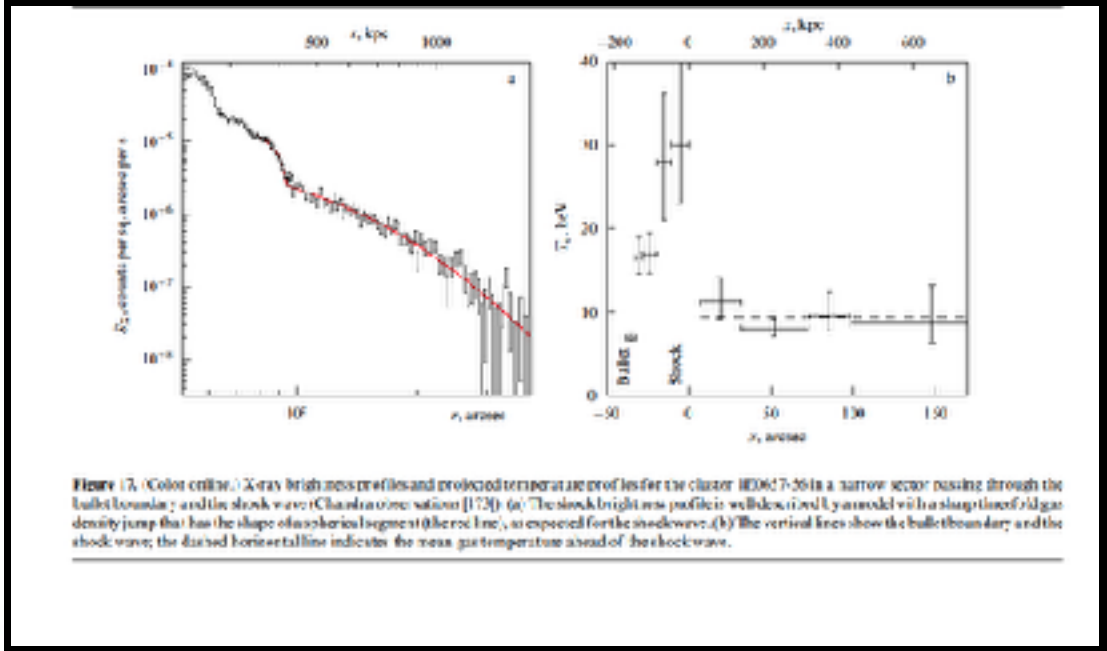

Figure 13. (Color online.) X-ray brightness profiles and projected temperature profiles for the cluster 1E0657-56 in a narrow sector passing through the bullet's boundary and the shock wave (Chandra observations [173]). (a) The shock brightness profile is well described by a model with a sharp tilted edge (a density jump that has the shape of a spherical segment (the red line), as expected for the shock wave. (b) The vertical lines show the bullet boundary and the shock wave; the dashed horizontal line indicates the mean gas temperature ahead of the shock wave.

The discovery of the brightest SMG behind the Bullet Cluster was done by Wilson, Hughes, Aretxaga et al. (2008) using AzTEC (First light Instrument of GTM Alfonso Serrano) on ASTE (ALMA's prototype antenna).

Table 1. Derived parameters for MMJ065837−5557.0. The absolute calibration error of the flux density is given in parentheses.

Flux density	$15.9 \pm 0.5\ (\pm 1.3)$ mJy
SZE-corrected flux density	$13.5 \pm 0.5\ (\pm 1.0)$ mJy
RA centroid position	06:58:37.31 ± 0.02 s
Dec. centroid position	−55:57:01.5 ± 0.32 arcsec
Source FWHM (RA)	36 ± 1.3 arcsec
Source FWHM (Dec.)	32 ± 1.2 arcsec
Position angle of elongation	34° ± 8°
reduced χ^2/ of fit	0.94

$$z_{phot} = 2.7 \pm 0.2$$

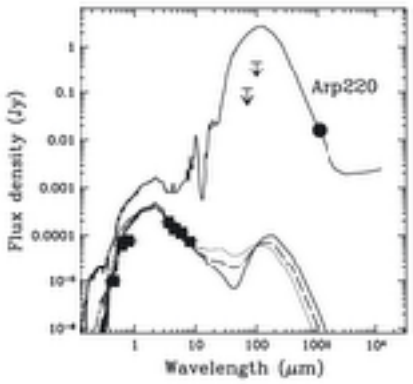

Figure 5. SED of the $z = 0.297$ cluster member galaxy E (Fig. 4) near the MMJ065837−5557.0 position centroid. The measured photometry data for the galaxy E are shown as filled squares, and they are compared with three elliptical galaxy SED templates by Polletta et al. (2007) with different ages (2, 5 and 13 Gyr old shown as dotted, dashed and solid lines, respectively). The two 3σ upper limits from the IRAS 60 and 100 μm bands are also shown. The Arp 220 SED by Polletta et al. is normalized to the 1.1 mm AzTEC measurement (filled circle) for comparison.

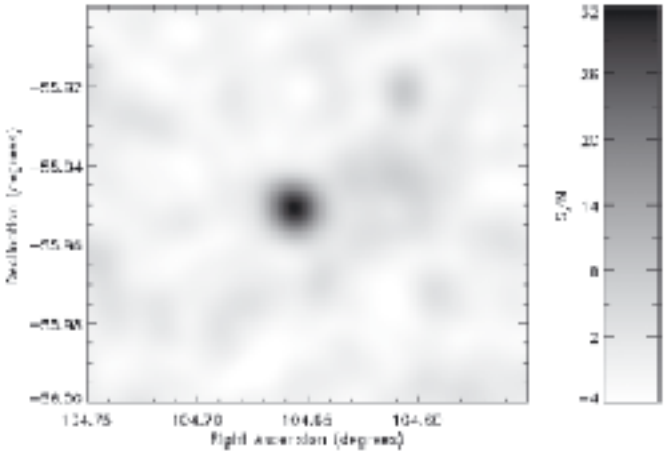

Figure 1. AzTEC image of MMJ065837−5557.0. The colour bar shows the shading in units of signal-to-noise of a point-source detection. The underlying noise in the map varies by 4.6 per cent across the portion of the image shown. The faint diffuse emission to the west of the point source is dominated by the extended SZE signal from the Bullet Cluster (Bevan et al. in preparation); however, due to the point-source filtering of the map, no morphological information about the SZE should be taken from this figure.

Atacama Pathfinder EXperiment APEX Telescope

Max-Planck-Institut für Radioastronomie

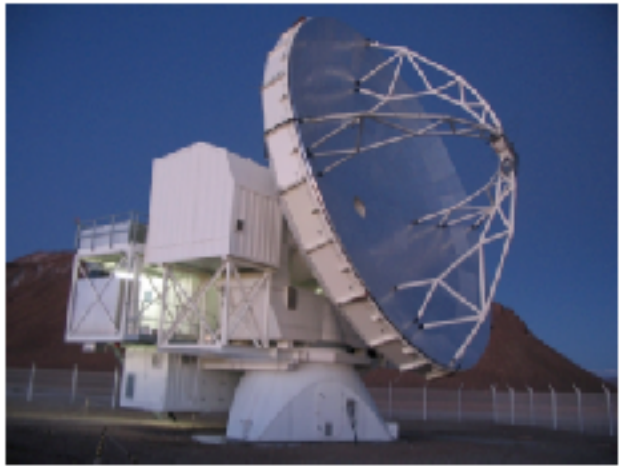

The APEX Telescope

Location	Llano de Chajnantor 50 Km east of San Pedro de Atacama, Northern Chile
Coordinates	Latitude : 23°00'20.8" South Longitude :67°45'33.0" West Altitude : 5105 m
Diameter	12 m
Mass	125000 kg
Main reflector	264 aluminium panels average panel surface r.m.s. 5 micron
Secondary reflector	Hyperbolical Aluminium Diameter 0.75m
Mounting	Alt-Az
Surface	17 micron

Technical description of LABOCA

General

LABOCA is a multi-channel bolometer array for continuum observations. It operates in the 870 µm (345 GHz) atmospheric window. The array consists of 295 channels, which are arranged in 9 concentric hexagons around a central channel. The angular resolution is 18.6″ (HPBW), and the total field of view is 11.4′. With a channel separation of about 36″ (twice the beam size) the array is undersampled, thus special mapping techniques are used to obtain fully-sampled maps in a time-efficient manner.

The Bolometers

A bolometer is practically a thermometer. The radiation arriving at APEX from astronomical objects is absorbed by a thin metal film cooled to about 280 mK. This metal changes its temperature while absorbing the radiation, and this is measured by a heat-sensitive semiconductor. This results in a voltage change, which can be measured and amplified and is in principle proportional to the intensity of the incoming radiation.

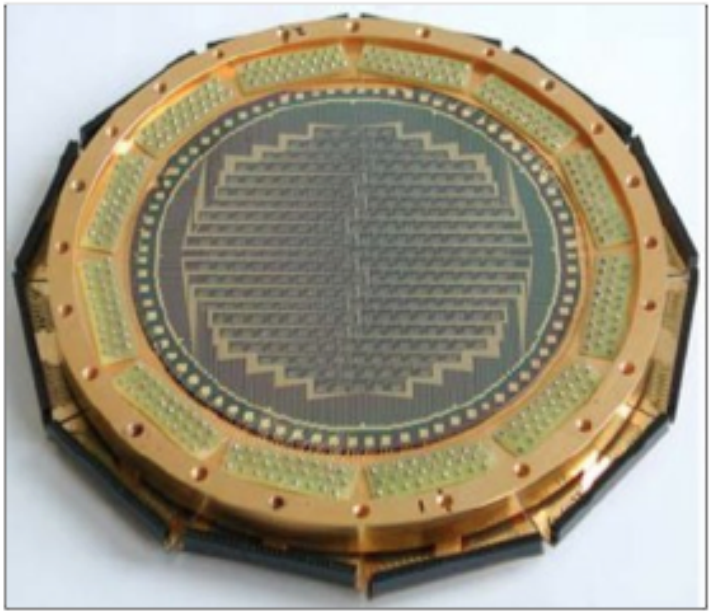

For LABOCA, the thermal, electrical and mechanical structure of the bolometer array is based on a single silicon wafer. Free-

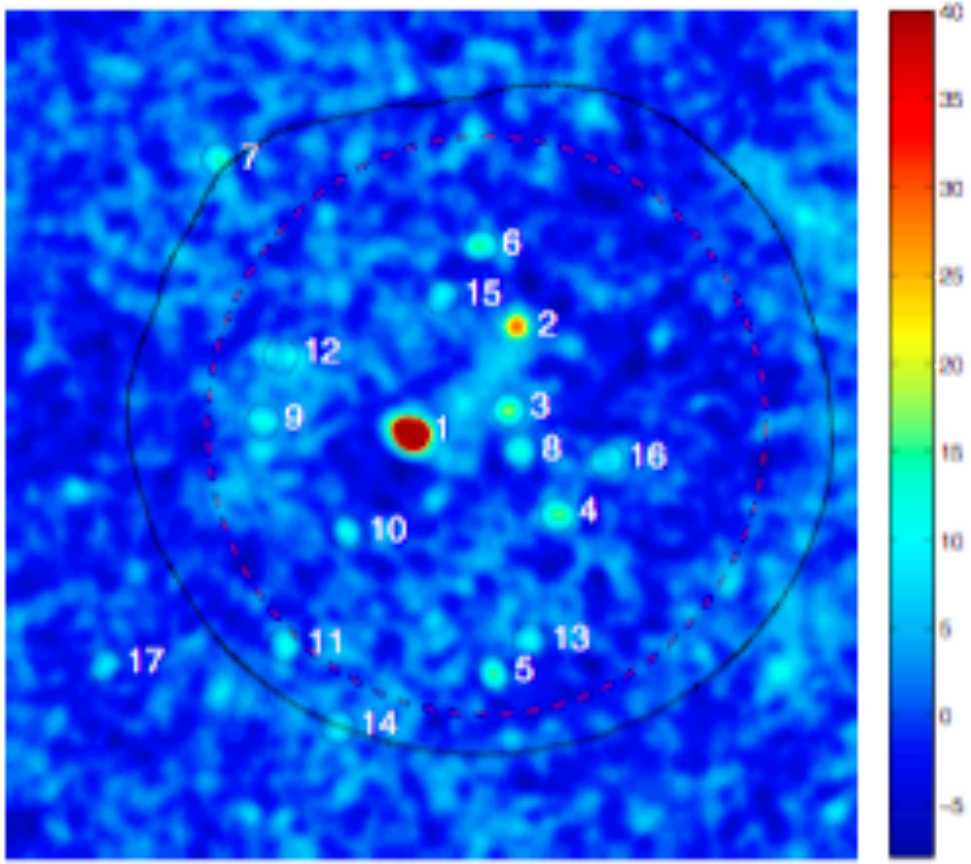

The GMF significance map, $F/\Delta F$, is computed as

$$\frac{F}{\Delta F} = \frac{(S \cdot W) \otimes P}{\sqrt{W \otimes P^2}} \quad (1)$$

where S is the signal map, W is the weight map (the reciprocal of the noise map, squared), and P is a Gaussian of the same size as the beam. The $\otimes$ sign denotes a convolution.

Johansson et al. 2010, A&A, 514, A77

Table 2. List of sources extracted from the LABOCA map.

Source	α(J2000) (hours)	δ(J2000) (° ′ ″)	Flux density[a] (mJy)	Deboosted[b] flux density (mJy)	Demagnified[c] flux density (mJy)	$F/\Delta F$[d]
1	06:58:37.62	−55:57:04.8	48.6 ± 1.3[e]	48.0 ± 1.3	0.64	82.8
2	06:58:24.47	−55:55:12.5	15.1 ± 1.0	14.7 ± 1.0	8.8	29.9
3	06:58:25.45	−55:56:40.1	6.9 ± 0.9	6.4 ± 1.0	2.2	17.8
4	06:58:19.36	−55:58:30.3	8.2 ± 0.9	7.7 ± 0.9	4.7	16.2
5	06:58:27.27	−56:01:16.3	9.0 ± 1.3	8.0 ± 1.3	6.3	15.9
6	06:58:28.94	−55:53:48.4	9.3 ± 1.2	8.6 ± 1.2	6.3	15.4
7	06:59:01.39	−55:52:18.1	11.9 ± 2.1	9.7 ± 2.1	8.4	14.2
8	06:58:24.05	−55:57:23.0	5.3 ± 0.9	4.7 ± 1.0	1.8	13.1
9	06:58:55.98	−55:56:51.7	5.4 ± 1.2	4.4 ± 1.3	3.3	12.8
10	06:58:45.60	−55:58:48.0	6.2 ± 1.1	5.5 ± 1.1	3.6	12.0
11	06:58:53.22	−56:00:45.0	7.8 + 1.5	6.4 + 1.6	5.2	11.9
12	06:58:52.22	−55:55:45.7	5.5 ± 1.2	4.5 ± 1.2	3.4	11.2
13	06:58:22.88	−56:00:40.7	4.8 ± 1.2	3.8 ± 1.3	2.9	11.0
14	06:58:46.68	−56:02:11.8	7.2 + 1.9	4.6 + 2.5	3.8	10.8
15	06:58:33.69	−55:54:40.8	4.6 + 1.1	3.6 + 1.2	2.5	10.1
16	06:58:12.44	−55:57:29.7	4.9 + 1.0	4.2 + 1.0	1.9	9.2
17	06:59:15.72	−56:01:07.5	23.6 + 3.9	–[f]	–	9.0

Notes. Statistical uncertainties on the listed positions are 1–2″, which is smaller than the pointing uncertainty. [(a)] Flux density as extracted from the map. [(b)] Flux density corrected for boosting due to confusion noise. [(c)] Flux density corrected for lensing. [(d)] Significance of the detection in the Gaussian-matched-filtered map. [(e)] Source #1 is extended relative to the 22″ beam: it has an apparent size of 29.2″ × 23.3″. [(f)] Source #17 lies in the outer part of the map where the noise level is high and the method used to deboost the flux densities fails.

Johansson et al. 2010, A&A, 514, A77

APEX+LABOCA

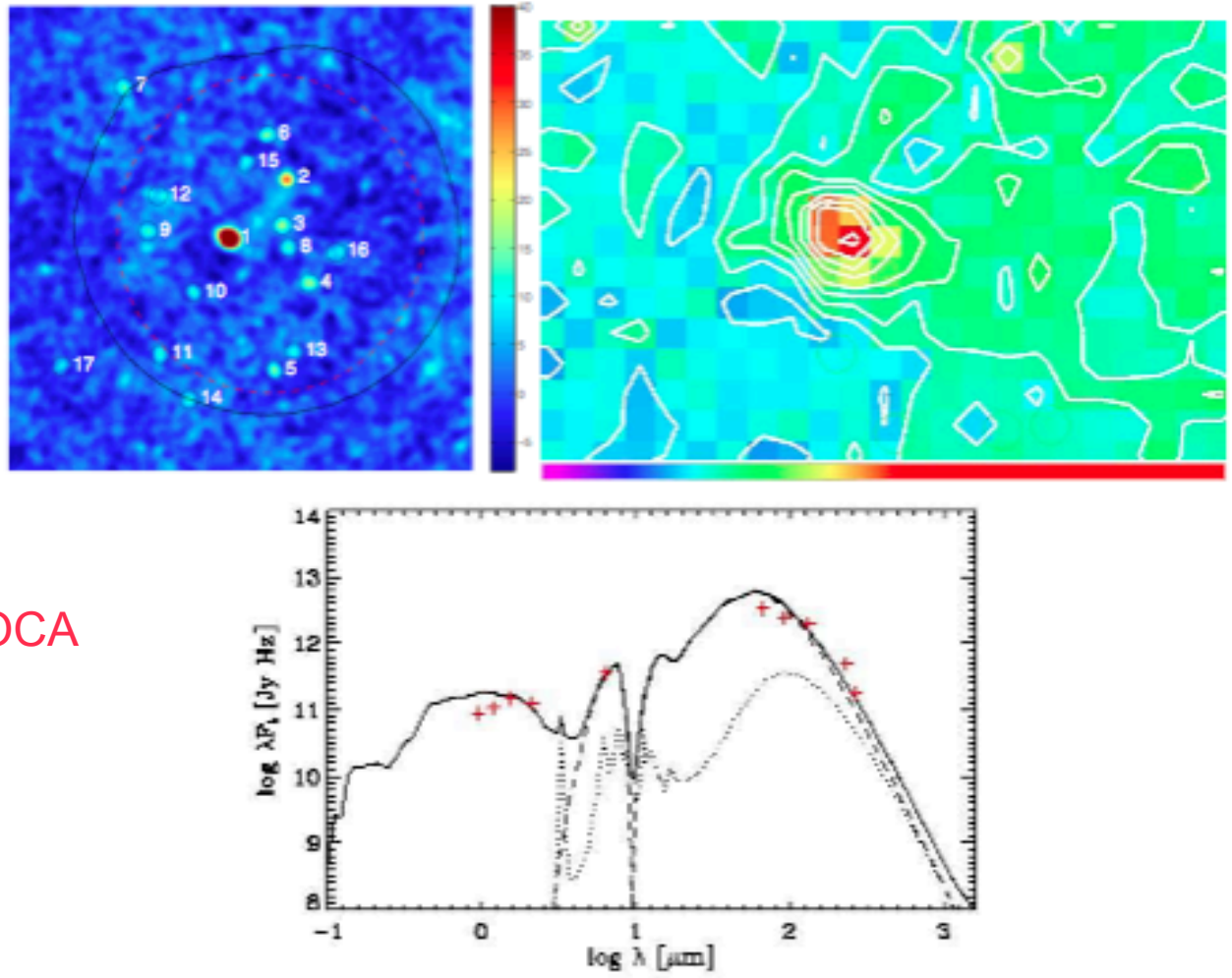

Figure 1: Figure 1a (upper left).- Gaussian filtered map generated from APEX+LABOCA observations at 870 μm. This map shows Source #1 with eleven further sources within the central 10-arcmin region of constant noise in the analysis of Johansson et al. (2010). Figure 1b (upper right).- Smaller region near Source #1, from an unsmoothed map generated from APEX+LABOCA observations at 870 μm, the faint extended Sunyaev-Zel'dovich effect signal is also visible (green). The resolution of 19.1 arcsec in this image is insufficient to resolve components A and B of Source #1. However the elongation of the contours is consistent with the positions of source A and B. Figure 1c (lower center).- Preliminary modeling of the rest-frame SED of Source #1 using GRASIL (Silva et al. 1998), with a renormalized flux density scale. Data-points are taken from Gonzalez et al. (2009), Rex et al. (2009), Johansson et al. (2010); and the revised measurement by Wilson et al (2009). The full data set cannot be modeled as a typical ULIRG.

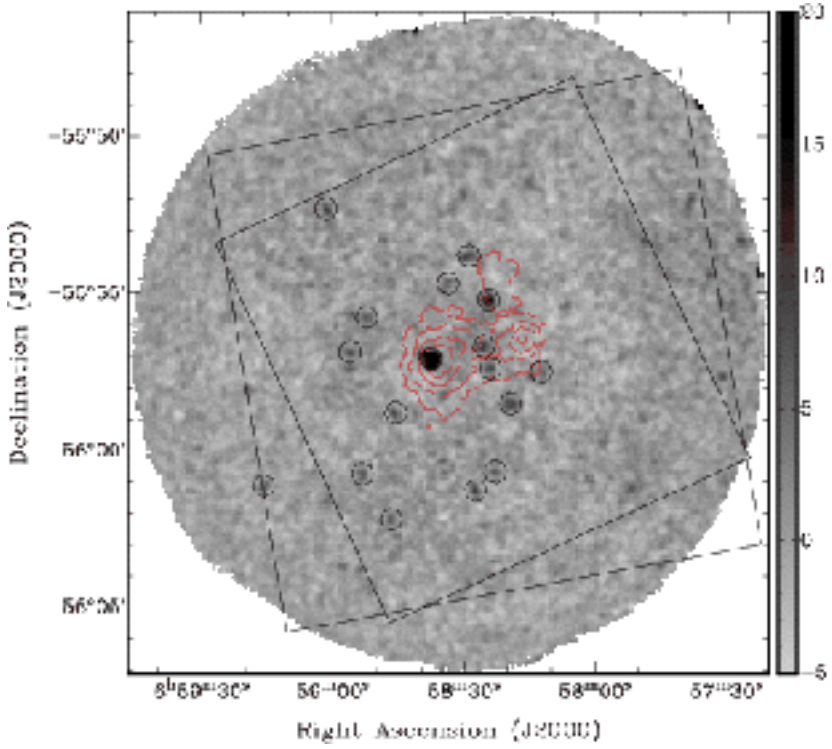

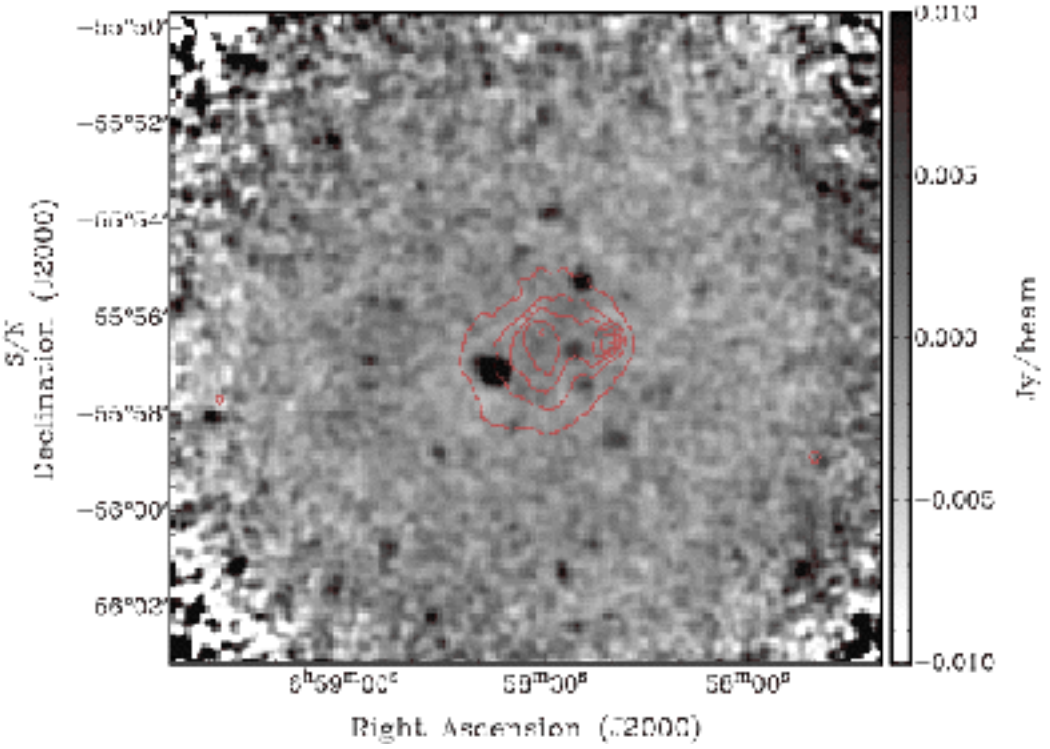

Left: signal-to-noise map with overlaid circles indicating extracted submm sources. The contours show the the projected mass density from the weak lensing analysis by Clowe et al. (2006). The contours range from 40 to 85% of the maximum value and are spaced by 15%. The weak lensing map was retrieved from the website http://flamingos.astro.ufl.edu/1e0657/public.html. The rectangles show the regions of complete coverage of Spitzer MIPS (small rectangle) and IRAC (large rectangle). *Right*: signal map (in units of Jy/beam) with contours of the X-ray surface brightness from XMM-Newton observations. The noise level in the signal map increases rapidly towards the outskirts because of the low coverage there.

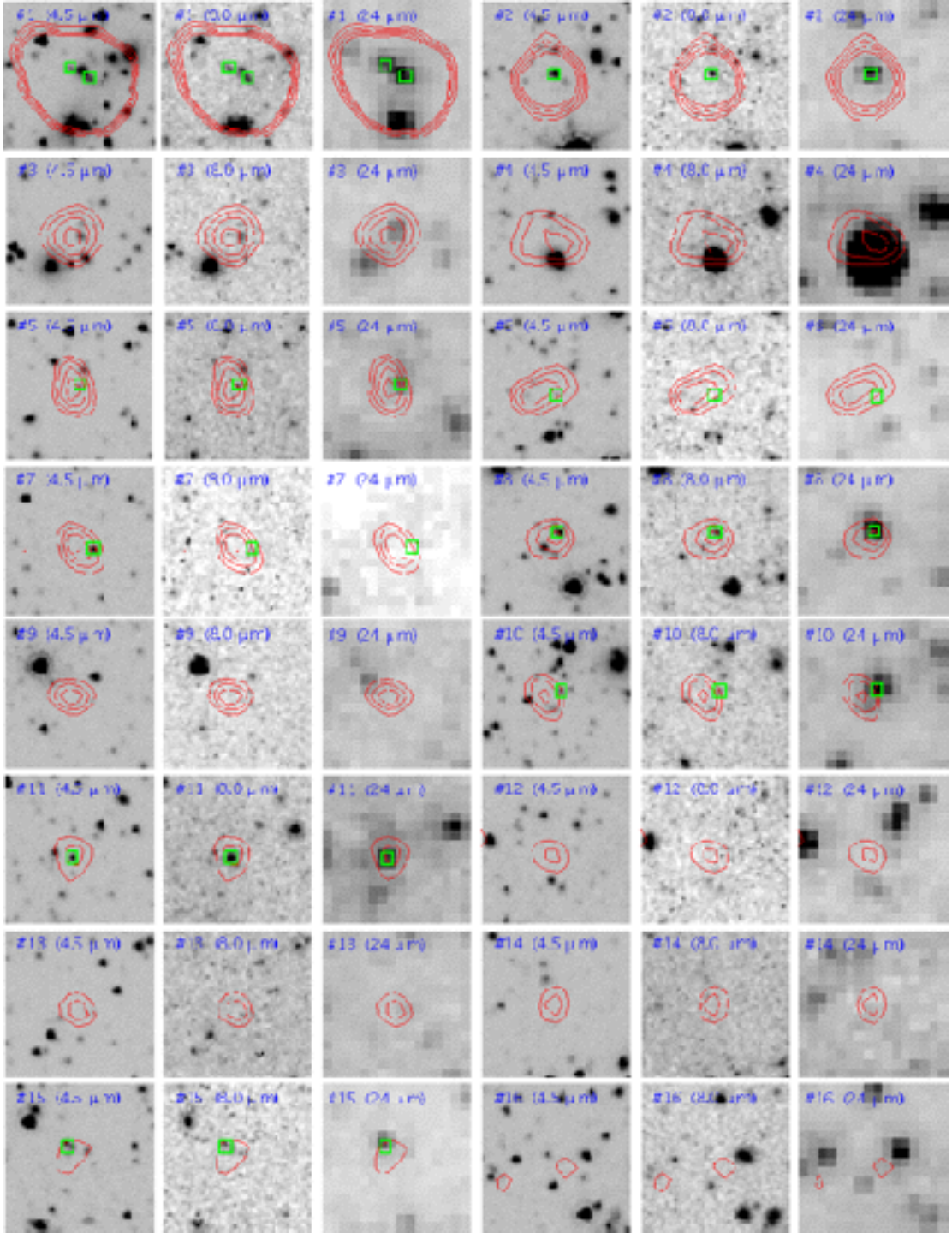

The bullet has the most lensed galaxies

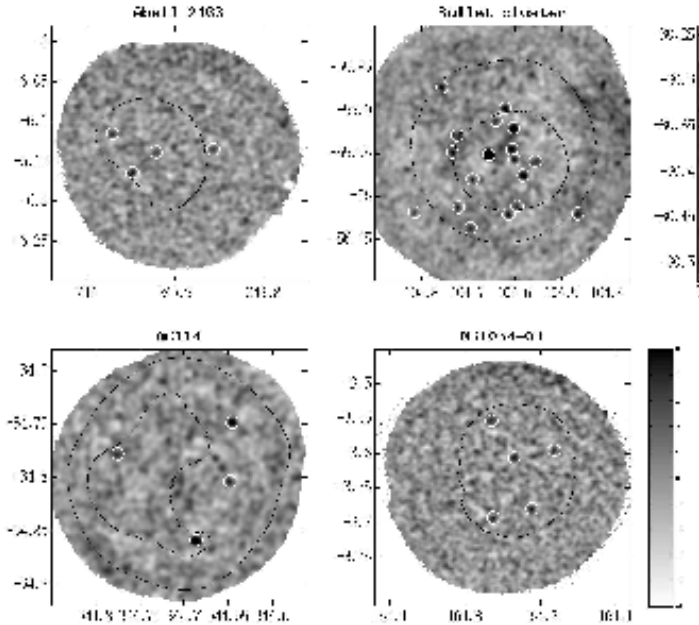

Fig. 1. Signal-to-noise maps of the five cluster fields. White circles represent the significant sources in the map and black contours show the noise maps of each cluster map at levels of 2, 4 and 8 mJy beam^{-1}. The signal-to-noise representation causes the appearance of the increasing noise towards the edge of each map to be suppressed.

Target	α^a [J2000] [h m s]	δ^a [J2000] [° ′ ″]	z	rms[b] [mJy beam^{-1}]	Ω^c [arcmin^2]
Abell 2163	16 15 45.1	−06 08 31	0.203	2.2	150
Bullet Cluster[1]	06 58 29.2	−55 56 45	0.296	1.2	220
Abell 2744[2]	00 14 15.0	−30 22 60	0.308	1.5	220
AC 114[3]	22 58 52.3	−34 46 55	0.312	1.2	130
MS 1054-03[4]	10 57 00.2	−03 37 27	0.823	1.6	200

Why the Bullet Cluster (1E0657-56)?

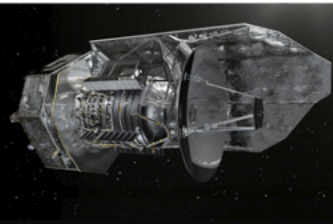

- Known bright, multiple-image, lensed submillimeter galaxy in the background (z=2.8; Bradac+06, Gonzalez+09, Rex+09)

- Recent collision of two clusters at z=0.3 (Markevitch+02,04)
  - Sub-cluster conveniently travelling perpendicular to our line of sight (<8° from sky plane)
  - Analysis of X-ray emission shows a supersonic bow shock proceeding the gas
  - Weak lensing maps indicate the X-ray gas lags behind the cluster galaxies due to ram pressure

- Abundant ancillary data:
  - multi-wavelength imaging
  - 930 spec-zs
    (mostly in cluster / foreground)
  - weak/strong lensing maps

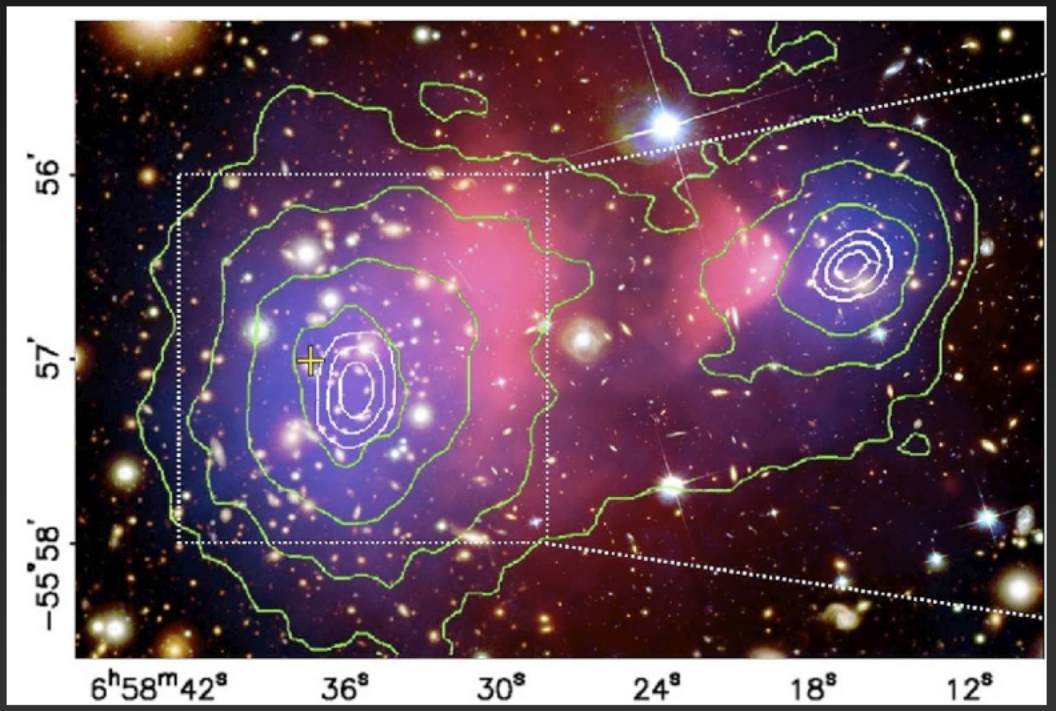

Clowe et al. (2004)
Rex et al. (2009)

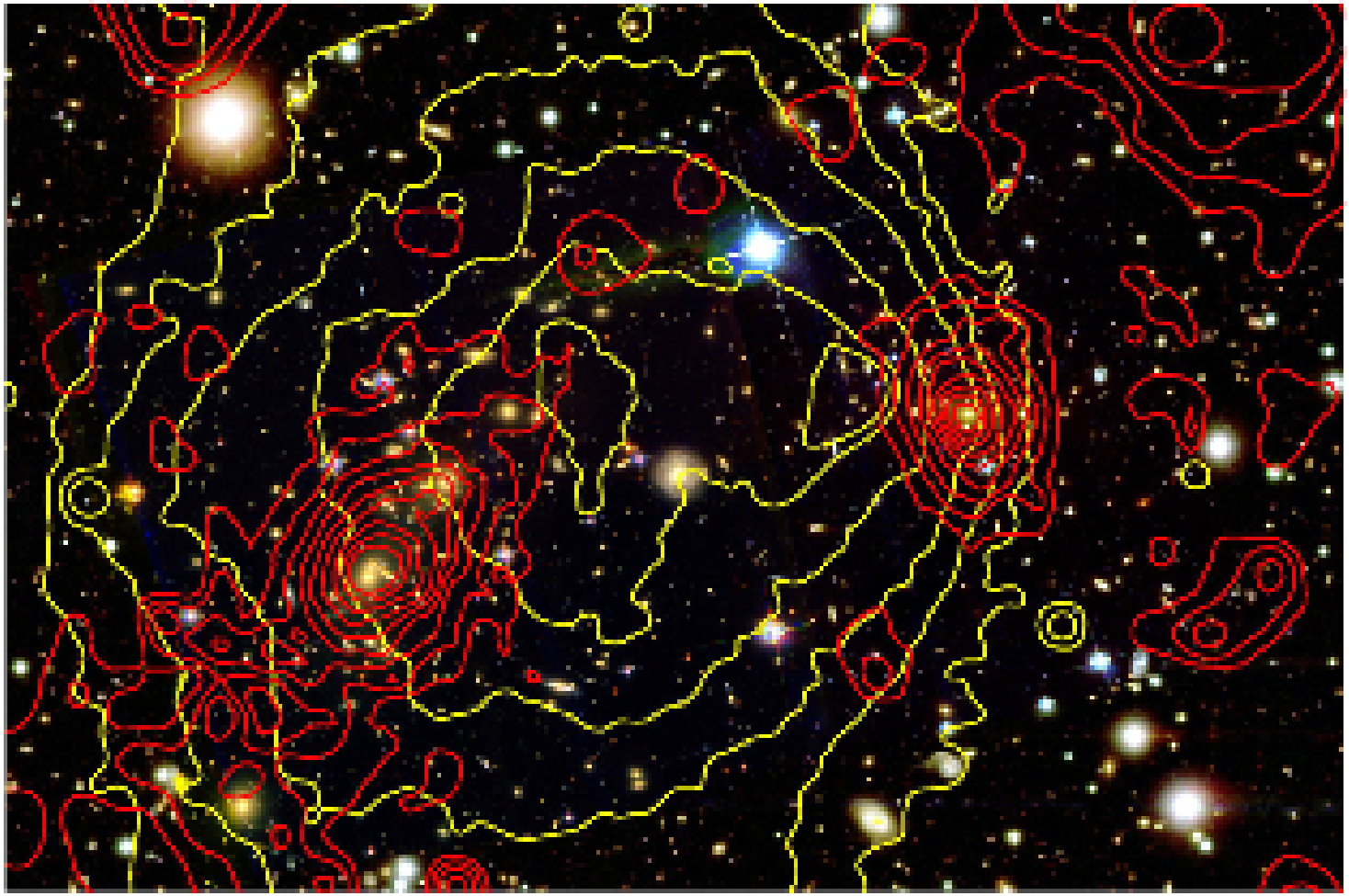

F435W−*V*−F814W (subcluster) color composite of the 1E0657 − 56. The ACS images are inse

Bullet Cluster

X-ray luminous cluster merger at $z = 0.3$

Special thanks...

Doug Clowe (Magellan/IMACS images)

Jean-Gabriel Cuby (VLT/HAWKI images)

Anthony Gonzalez, Sun Mi Chung (Magellan/IMACS redshifts)

Dario Fadda, Phil Appleton (CTIO Hydra redshifts)

Cathy Horellou, Daniel Johansson and LABOCA team

David Hughes, Itziar Aretxaga and AzTEC team

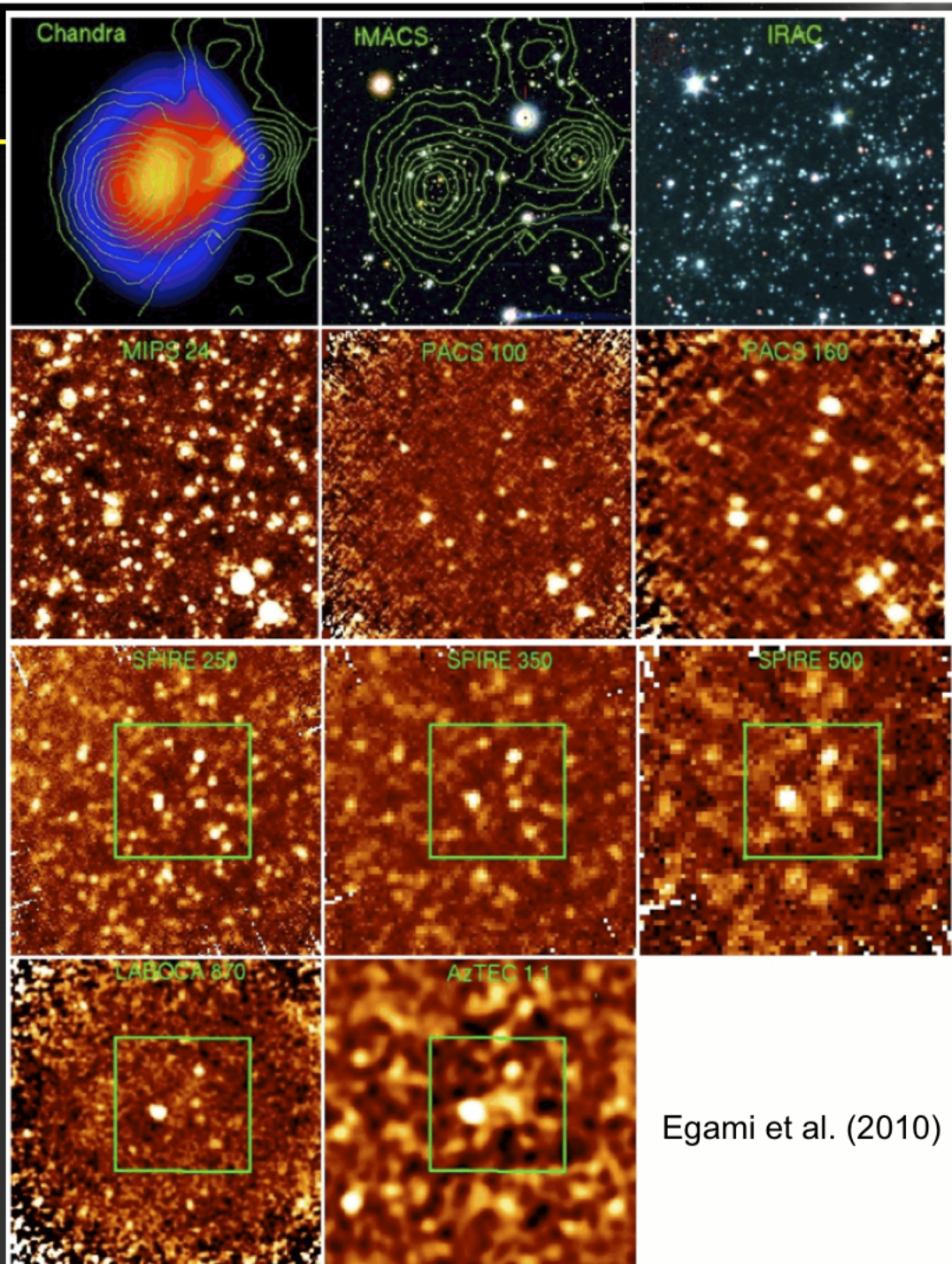

Egami et al. (2010)

BLAST vs SPIRE

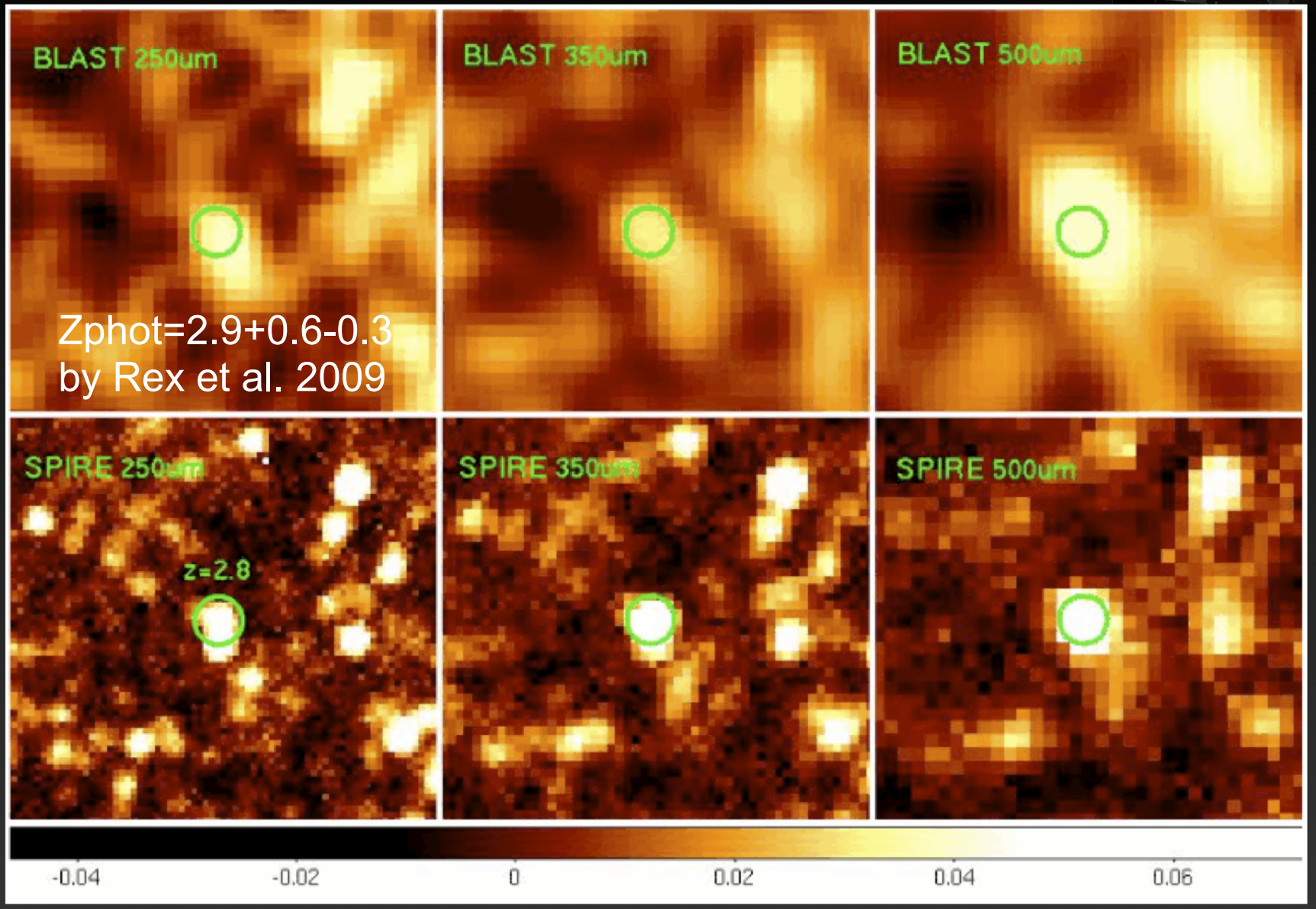

Far-IR/submm template SEDs

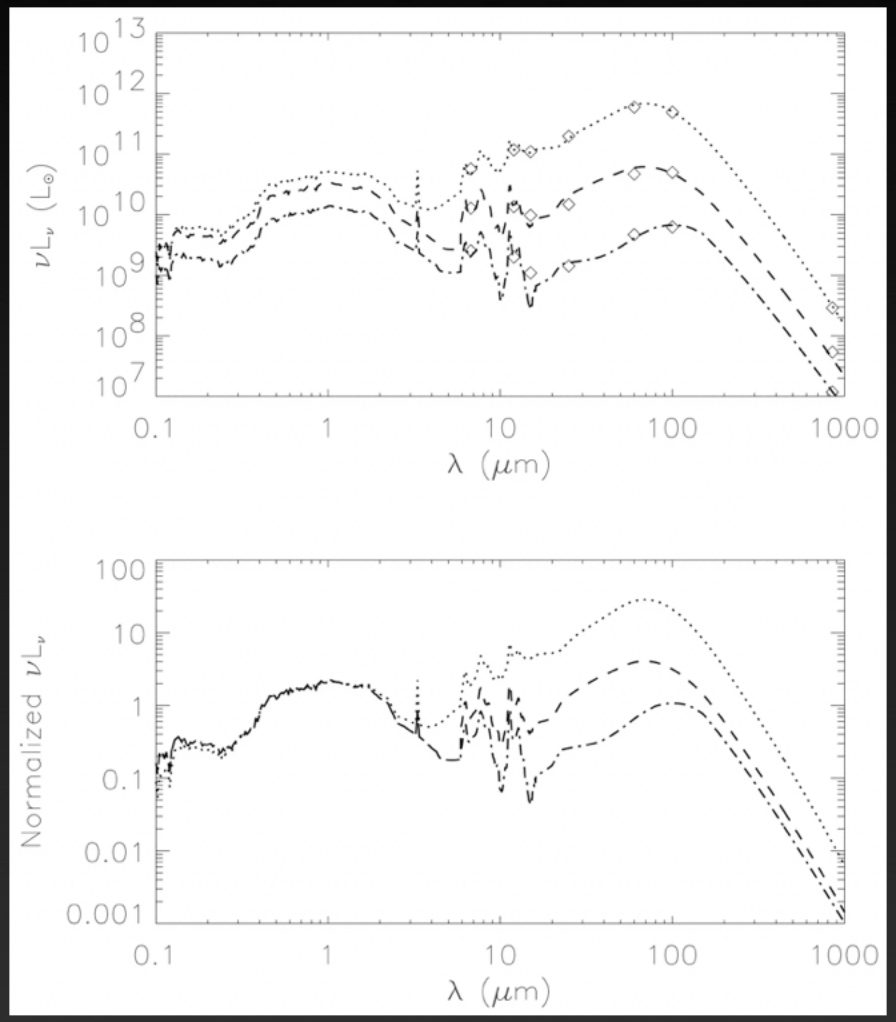

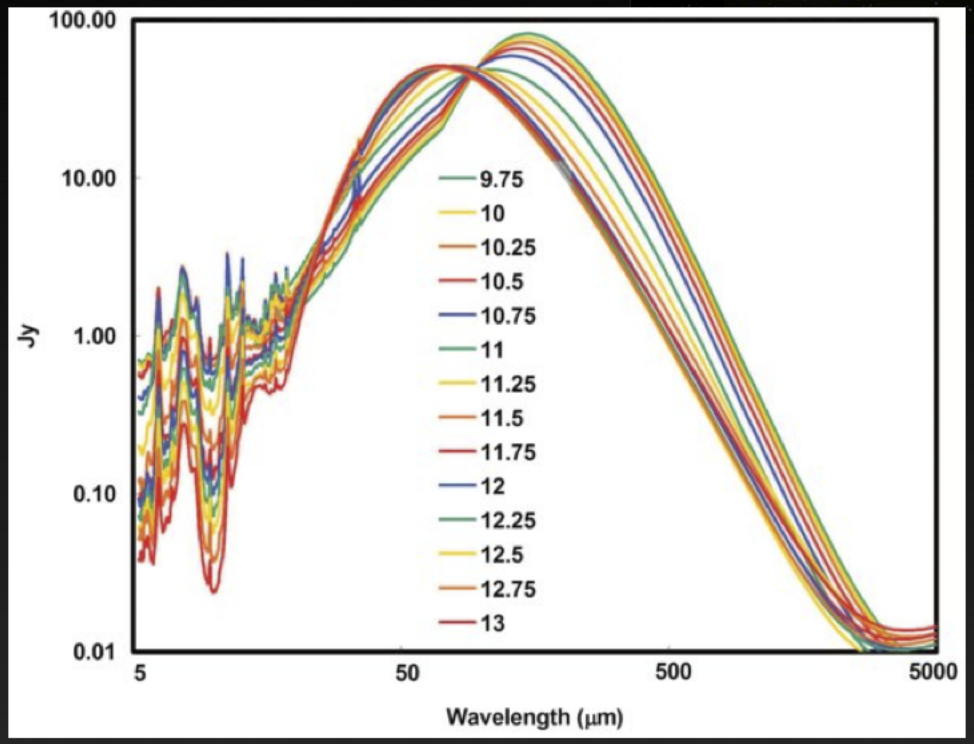

Rieke et al. (2009)

Chary & Elbaz (2001)

$L_{TIR} \uparrow \Rightarrow T_{dust} \downarrow \Rightarrow L_{FIR}/L_{MIR} \uparrow$

Do these local templates adequately describe high-z galaxies?

IR/submm SED of z=2.8 LIRG (5×10^{11} $L_\odot$)

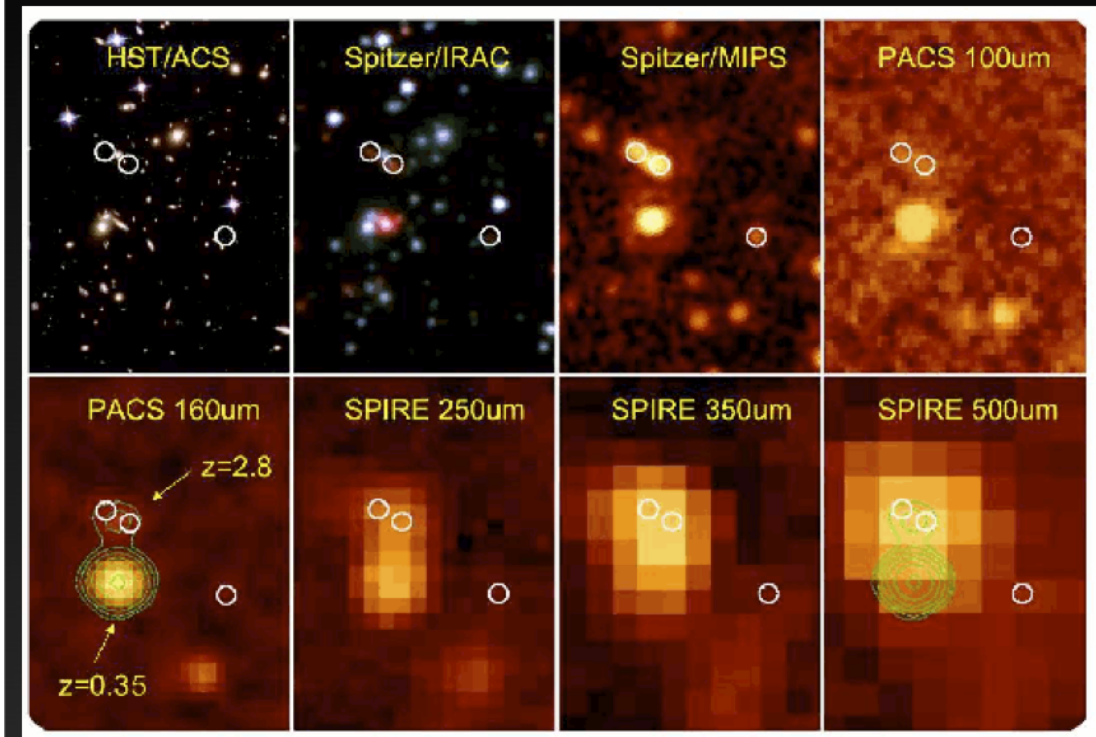

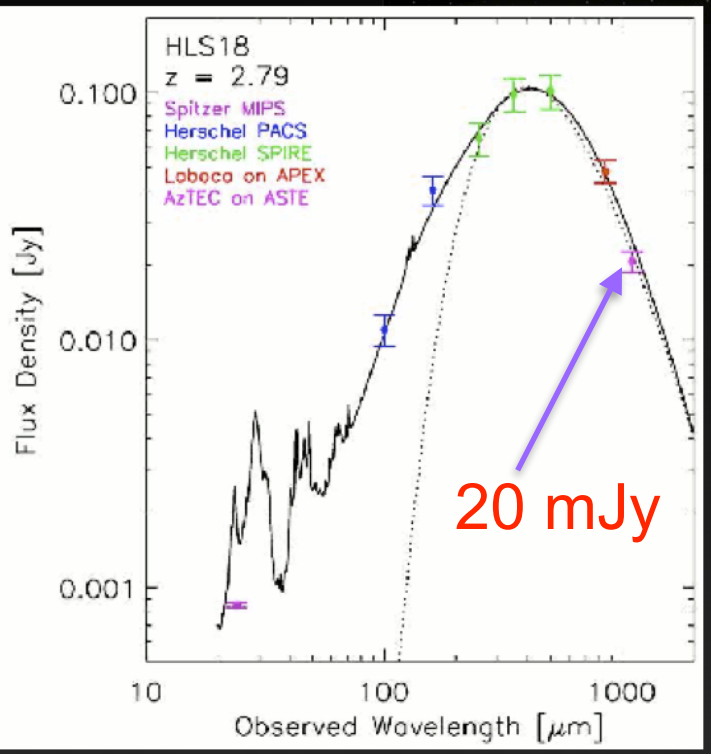

Rex et al. (2010)

Magnification factor 50x (→ 100x including unquantified local lensing)

- Observed flux densities: 7.0, 24.5, 65.3, 98.6, 101.4 mJy
- Corrected for lensing (x75): 0.09, 0.3, 0.9, 1.3, 1.4 mJy

Impossible to observe without lensing

That is all fine for imaging. But we need spectroscopic redshifts!!

Enters the Australian Telescope Compact Array and the Compact Array Broadband Backend (ATCA/CABB)

Schematic and now dated sub-mm spectrum of a molecular cloud showing fine structure & molecular emission lines (only the lowest rotational transition is shown).

Not all of the suggested species have been detected.

Phillips & Keene
Proc IEEE 80 1662 1992

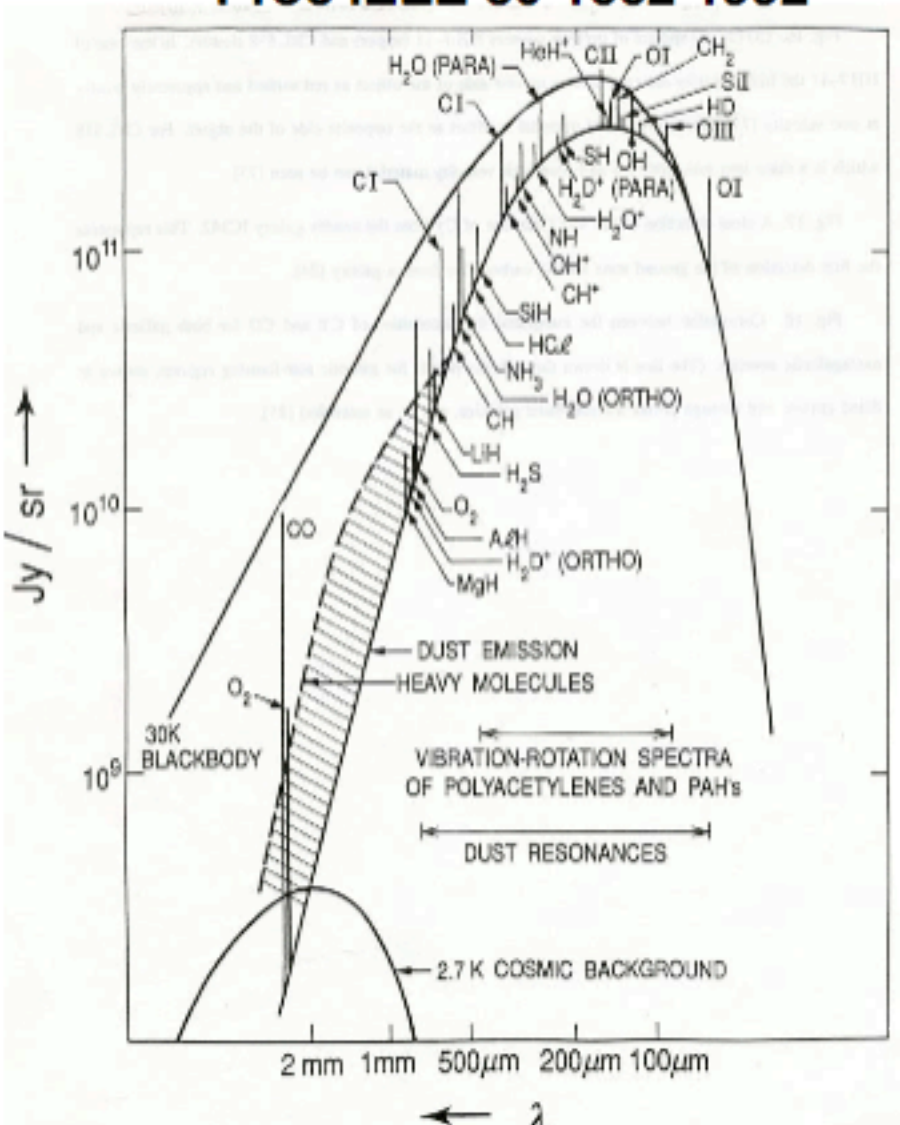

M82 reconstructed apodized spectrum

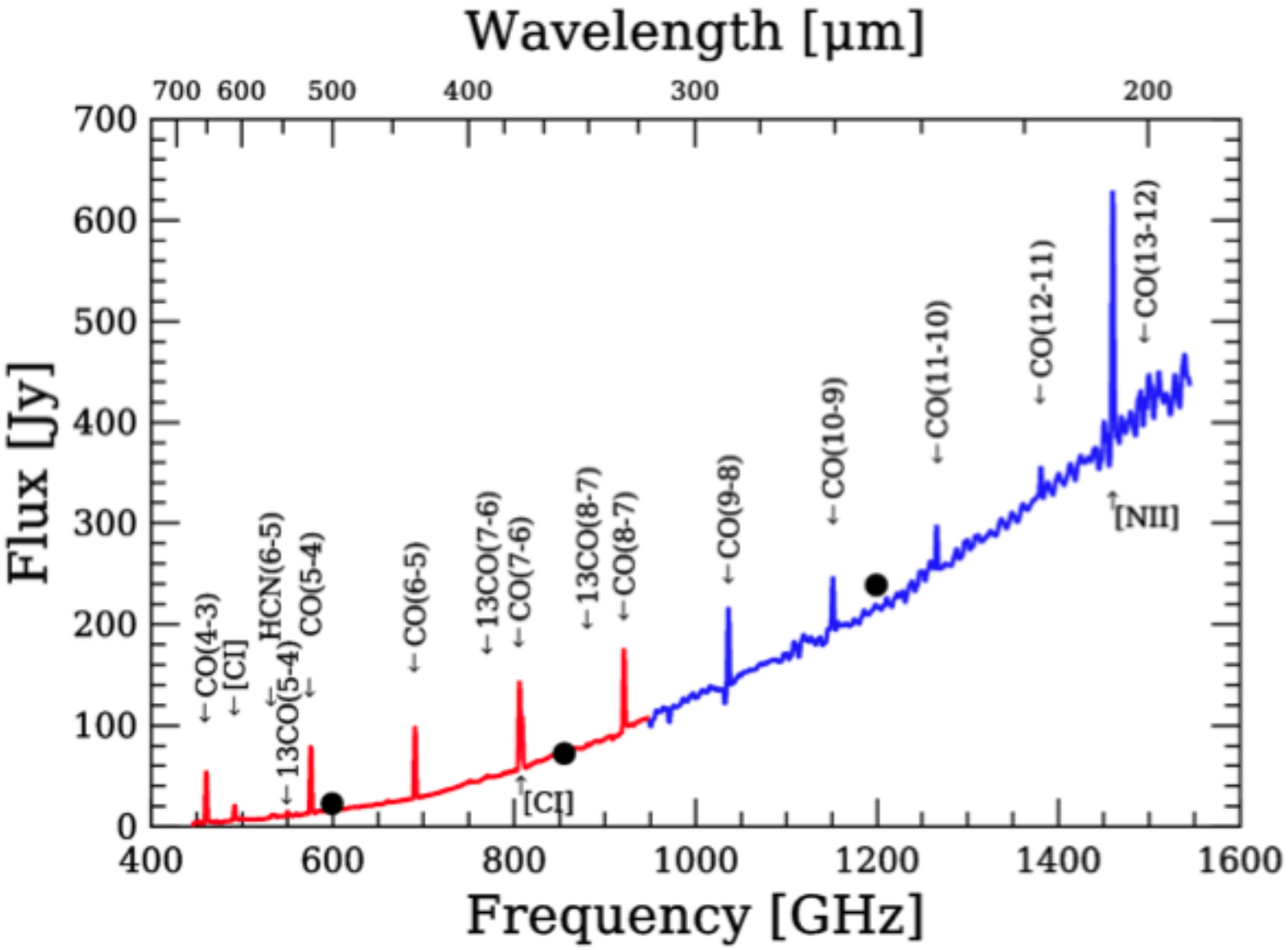

Gonzalez et al. 2010 PAH redshift, z=2.791 +/- 0.007

CO(3-2) ➔ 91.23 GHz; CO(1-0) ➔ 30.41 GHZ

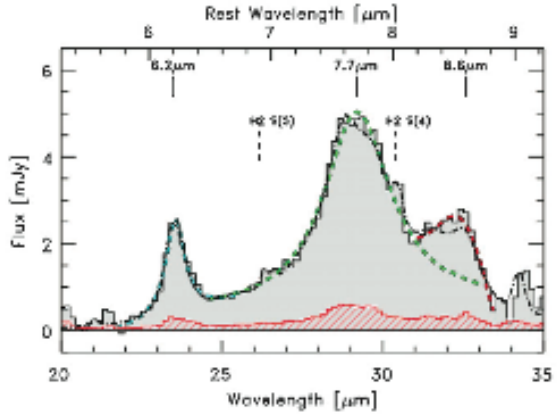

Figure 2. IRS spectrum of the galaxy, taken in the long-low mode. The data are presented as the shaded histogram, with the uncertainties shown by the hashed histogram. The dot-dashed line indicates the best fit from PAHFIT, while the dashed curves correspond to fits to the individual PAH lines using Drude profiles and the formulae from Smith et al. (2007). The vertical marks above the spectrum denote all spectral features robustly detected in our analysis.

(A color version of this figure is available in the online journal.)

Table 1
Observed Fluxes and Magnitudes[a]

Quantity	Value
$f(6.2\,\mu m)$	$1.4 \pm 0.2 \times 10^{-14}$ erg s^{-1} cm^{-2}
$f(7.7\,\mu m)$	$6.3 \pm 1.2 \times 10^{-14}$ erg s^{-1} cm^{-2}
$f(8.6\,\mu m)$	$5.2 \pm 3.3 \times 10^{-14}$ erg s^{-1} cm^{-2}
$f(H_2S(4))$	$5.8 \pm 1.9 \times 10^{-15}$ erg s^{-1} cm^{-2}
$f(H_2S(5))$	$2.5 \pm 1.2 \times 10^{-15}$ erg s^{-1} cm^{-2}
$f(7.7\,\mu m)/f(6.2\,\mu m)$	4.5 ± 1.1
m_{F160W}	23.80 ± 0.1 (AB)

Note. [a] All quoted values are for the combination of images A and B.

use a power law to fit the underlying continuum. We derive the redshift from the two strongest PAH features (6.2 μm and 7.7 μm), obtaining $z = 2.791 \pm 0.007$. This redshift confirms the photometric redshifts in the literature ($z \sim 2.7$–2.9; Wilson et al. 2008; Gonzalez et al. 2009; Rex et al. 2009).

The derived fluxes for the PAH features are listed in Table 1. The flux ratio for the two highest S/N lines, $f(7.7\,\mu m)/f(6.2\,\mu m) = 4.5 \pm 1.1$, can be compared with results from Pope et al. (2008) for SMGs. The star formation dominated SMGs in the Pope et al. sample ($z \sim 1$–2.5) have flux ratios in the range of 1.4–3.5 for these PAH lines, some

red curve shows the histogram of the signal map.

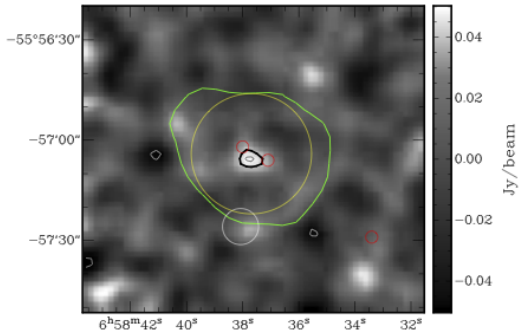

Fig. 2. SABOCA 350 μm map, overlaid with signal-to-noise contours at $\pm 3.0\sigma$ and $\pm 3.4\sigma$ (black and gray). SMM J0658 is clearly detected in this image at 3.6σ significance. We show also the positions of the three images of SMM J0658 (red circles) and that of an infrared-bright elliptical galaxy within the Bullet Cluster (white circle). The size of the white circle is 10.″6, the FWHM of the SABOCA image. The green line corresponds to the 3.5σ level of the LABOCA 870 μm detection and the yellow circle corresponds to the Herschel SPIRE 350 μm band beam FWHM (see Rex et al. 2010).

ATNF Facilities: ATCA 6 x 22m

CABB

Table 1. Some ATCA properties. — See the *ATCA Users Guide (Table 1.1)* for more details and up-to-date information.

ATCA observing bands	16-cm* (L/S)	6-cm (C)	3-cm (X)	15-mm (K)	7-mm (Q)	3-mm (W)
frequency range [GHz]	1.1 – 3.1	4.4 – 6.7	7.5 – 10.5	15 – 25	30 – 50	85 – 105
number of antennas	6	6	6	6	6	5
number of baselines	15	15	15	15	15	10
primary beam FWHM	44′ – 16′	10.′7 – 7.′4	6.′3 – 5.′1	∼2′	∼70″	∼30″

Notes: ATCA observing information can be found at *www.narrabri.atnf.csiro.au/observing*, including a link to the CABB Sensitivity Calculator which is highly recommended to obtain observing characteristics (e.g., T_{sys}) at specific frequencies and correlator settings (see also Fig. 3). The ATCA primary beam size (in arcmin) can be approximated by $50/\nu$ where ν is the observing frequency in GHz; the MIRIAD task PBPLOT provides details of the primary beam model (see Fig. 4). * In 2010 the 1.5 GHz (20-cm) and 2.3 GHz (13-cm) bands were combined into one broad band covering the frequency range from 1.1 to 3.1 GHz (now referred to as the 16-cm band). Note that the 3- and 6-cm bands can be used simultaneously.

the ringing that was commonly seen with the original ATCA and other correlators while observing narrow spectral lines.

- Modes providing high velocity resolution (for spectral line studies), high time resolution (for the study of fast transients), or pulsar binning come as an addition to the basic wide-bandwidth modes.
- CABB also provides auto-correlation data.

These improvements have a major impact on the scientific ability of the ATCA (see examples in § 6), including the following:

- the much larger bandwidth reduces the time required to reach any particular continuum sensitivity, and the increased sampling depth allows for higher dynamic range and lower T_{sys};
- narrow, independent channels allow for precise excision of narrowband interference;

configuration	channel width	
	primary band	secondary band
CFB 1M–0.5k	1.0 MHz	0.488 kHz
CFB 4M–2k	4.0 MHz	1.953 kHz
CFB 16M–8k	16.0 MHz	7.812 kHz
CFB 64M–32k	64.0 MHz	31.250 kHz

Table 2. Basic CABB configurations.

Table 1. Parameters of the ATCA observations and data.

Phase center (J2000):	
Right ascension	$06^h58^m37\overset{s}{.}62$
Declination	$-55°57'04\overset{''}{.}8$
3 mm	
Configuration	214H
Bandpass calibrator	1921–293
Phase calibrator	0537–441
Primary flux calibrator	Uranus
Primary beam FWHM	$38''$
Synthesized beam[1]	$2\overset{''}{.}1 \times 1\overset{''}{.}7$; $82°$
Channel velocity width	3.3 km s^{-1}
Final velocity resolution	80 km s^{-1}
Noise level[2]	**1.6** mJy
7 mm	
Configuration	750A and 750D
Bandpass calibrator	0537–441
Phase calibrator	0724–47
Primary flux calibrator	Uranus
Primary beam FWHM	$110''$
Synthesized beam[1]	$5\overset{''}{.}5 \times 1\overset{''}{.}6$; $-8°$
Channel velocity width	9.8 km s^{-1}
Final velocity resolution	80 km s^{-1}
Noise level[2]	**0.85** mJy

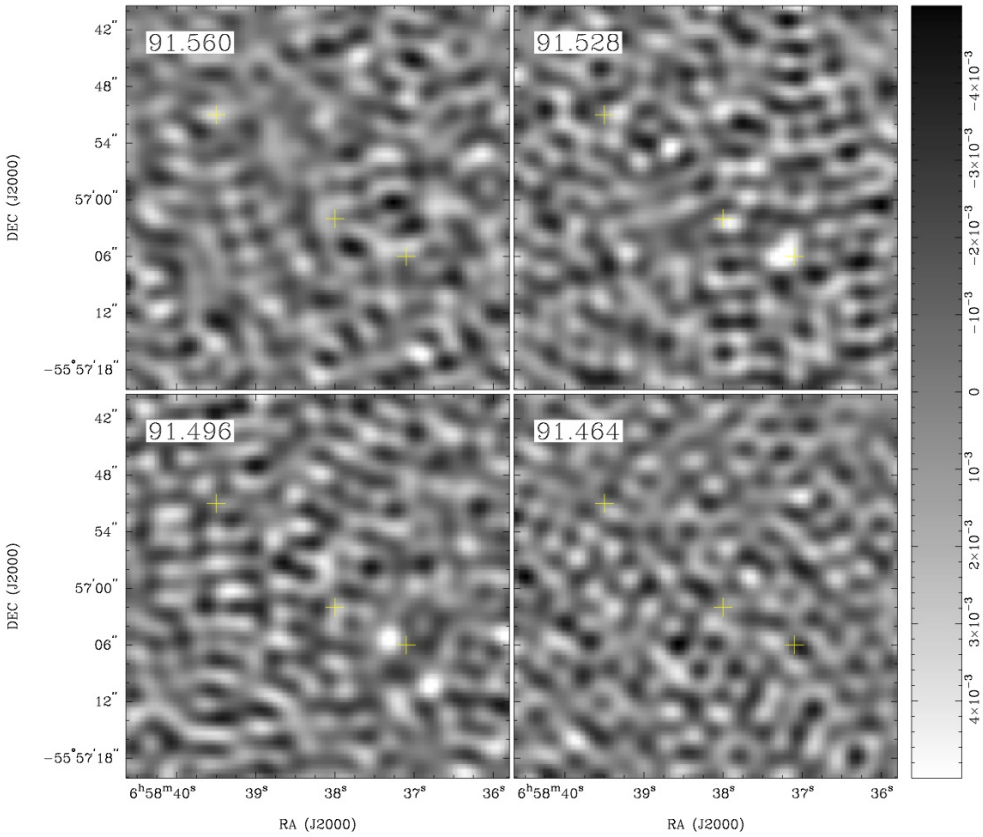

$$L_{\rm CO} = 3.25 \times 10^7 \, S_{\rm CO} \Delta v \, \nu_{obs}^{-2} \, D_L^2 (1+z)^{-3}$$

$$L_{\rm CO}\,[{\rm K\,km\,s^{-1}\,pc^2}]$$

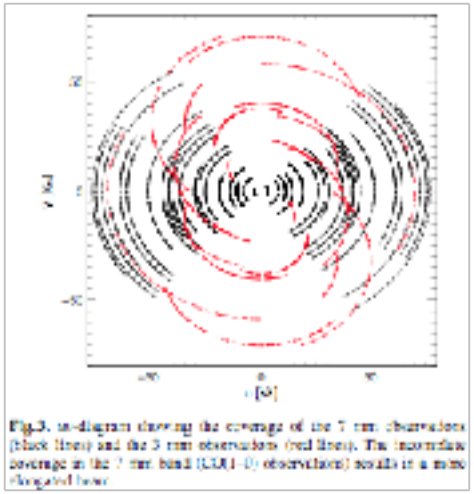

Fig. 3. uv-diagram showing the coverage of the 7 mm observations (black lines) and the 3 mm observations (red lines). The incomplete coverage in the 7 mm band (LMI-1) observations results in a more elongated beam.

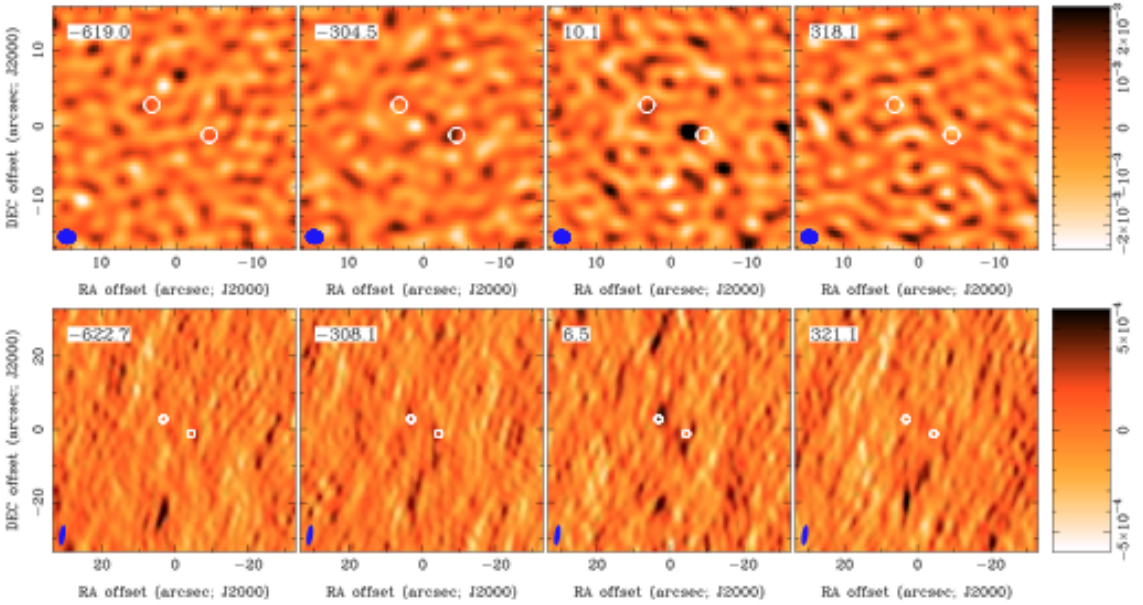

Fig. 4. *Top*: Channel maps at 3 mm, the band into which the CO(3–2) line is redshifted. The white circles indicate the positions of the Spitzer images A and B (GO10). Emission is clearly seen near image B (the western image) in the second and third panel. Faint emission near image A is seen in the third panel. The central velocity of each channel is noted in the upper left corners. The channel width of ~ 300 km s^{-1} corresponds to ~ 90 channels. The beam is shown in the bottom left corner. *Bottom*: Channel maps at 7 mm, the band into which the CO(1–0) line is redshifted. Note the different scale of those maps: they are twice as large as the 3 mm maps. The beam, shown in the bottom left corner, is elongated in the north-south direction. A continuum source is seen in every channel map about 20 arcseconds south of the two Spitzer images shown as white circles. Emission is detected close to images A and B and is best seen in the third panel. The channel width of ~ 300 km s^{-1} corresponds to ~ 30 channels. The color bars show the range of surface brightnesses, in mJy beam^{-1}.

L_{line}=3.25 X 10^7 S Δv ν_{obs}^{-2} $D_L^2(1+z)^{-3}$
(Solomon & Vanden Bout 2005)

Table 2. Integrated flux densities and upper limits on interesting molecular transitions in the ATCA bands.

Line	$\nu_{\rm rest}$	Image A	Image B	Image A+B	Image A+B	Flux B/A
		Integrated flux			$L'_{\rm line}\,(\mu_{\rm AB}/100)^{-1}$	
	[GHz]	[Jy km s^{-1}]			[10^8 K km s^{-1} pc^2]	
^{12}CO(1–0)	115.271	0.34 ± 0.07	0.29 ± 0.07	0.63 ± 0.10	22.6 ± 3.6	$0.9^{+0.5}_{-0.3}$
^{12}CO(3–2)	345.796	0.94 ± 0.35	2.25 ± 0.35	3.18 ± 0.50	12.7 ± 2.0	$2.4^{+1.3}_{-0.7}$
HCN(4–3)	354.460	…	…	< 8.0	< 30	…
HCO$^+$(4–3)	356.734	…	…	< 8.0	< 30	…
CS(7–6)	342.883	…	…	< 1.0	< 4	…
Brightness temperature ratios (r_{31})						
		$0.31^{+0.22}_{-0.14}$	$0.86^{+0.45}_{-0.28}$	$0.56^{+0.21}_{-0.15}$		

Notes. Uncertainties correspond to the 1σ level while upper limits are < 3σ. Integrated flux values are derived from fitting point sources at the positions of images A and B in the CO(1–0) and CO(3–2) maps collapsed for velocities between −350 and +170 km s^{-1}, as described in the text. This velocity range was determined from the spectral extent of the CO(3–2) spectrum.

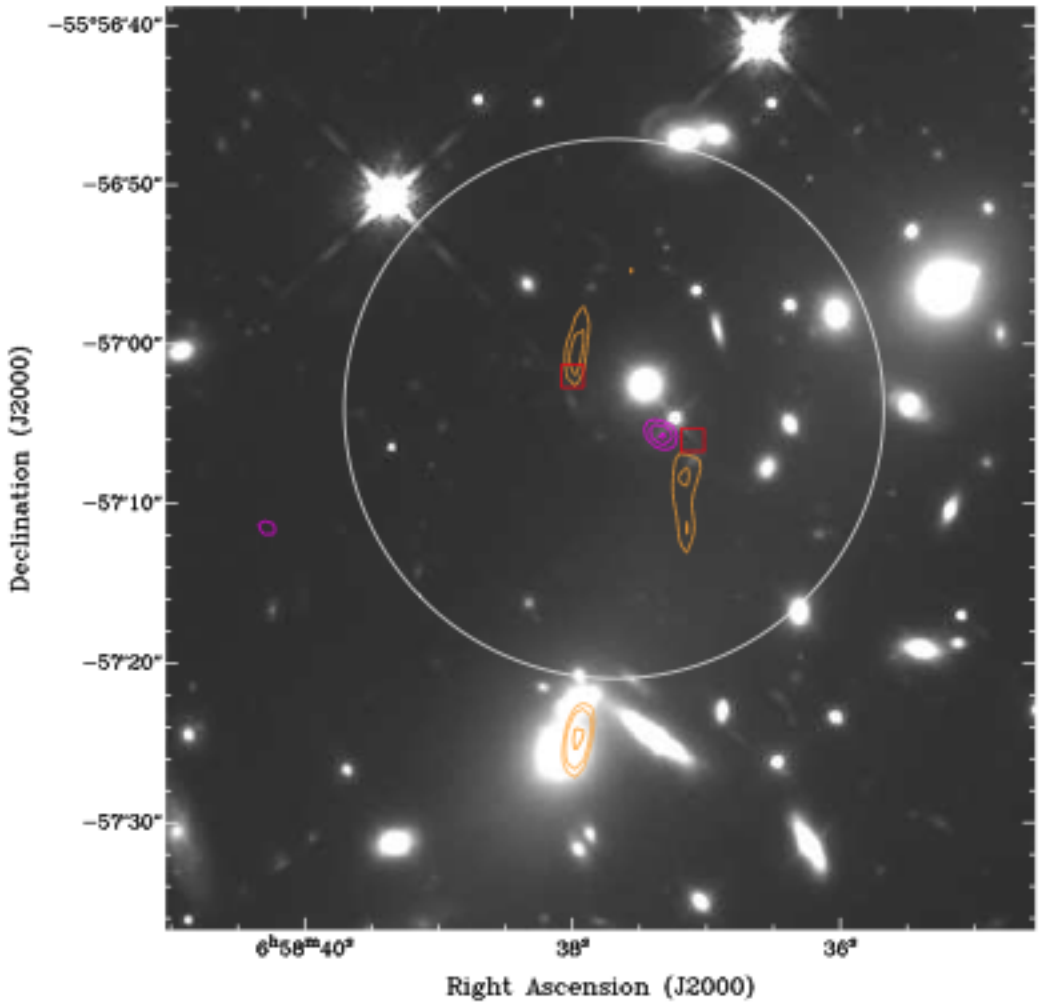

Fig. 5. Hubble Space Telescope WFC3 1.6 μm image of the region around SMM J0658. The orange contours show the CO(1–0) integrated intensity of both images of SMM J0658 and the 7 mm continuum emission from the cluster galaxy to the south, magenta contours show the CO(3–2) integrated intensity. The contours denote the 3, 4, 5σ-levels. The two red squares indicate the location of the two infrared Spitzer images, A to the east and B to the west (Gonzalez et al. 2009). The white circle shows the extent of the ATCA FWHM primary beam for the CO(3–2) observations (the primary beam at 7 mm is larger than the field displayed here). The offsets seen between the various components are discussed in Sect. 5.1.

fold arc

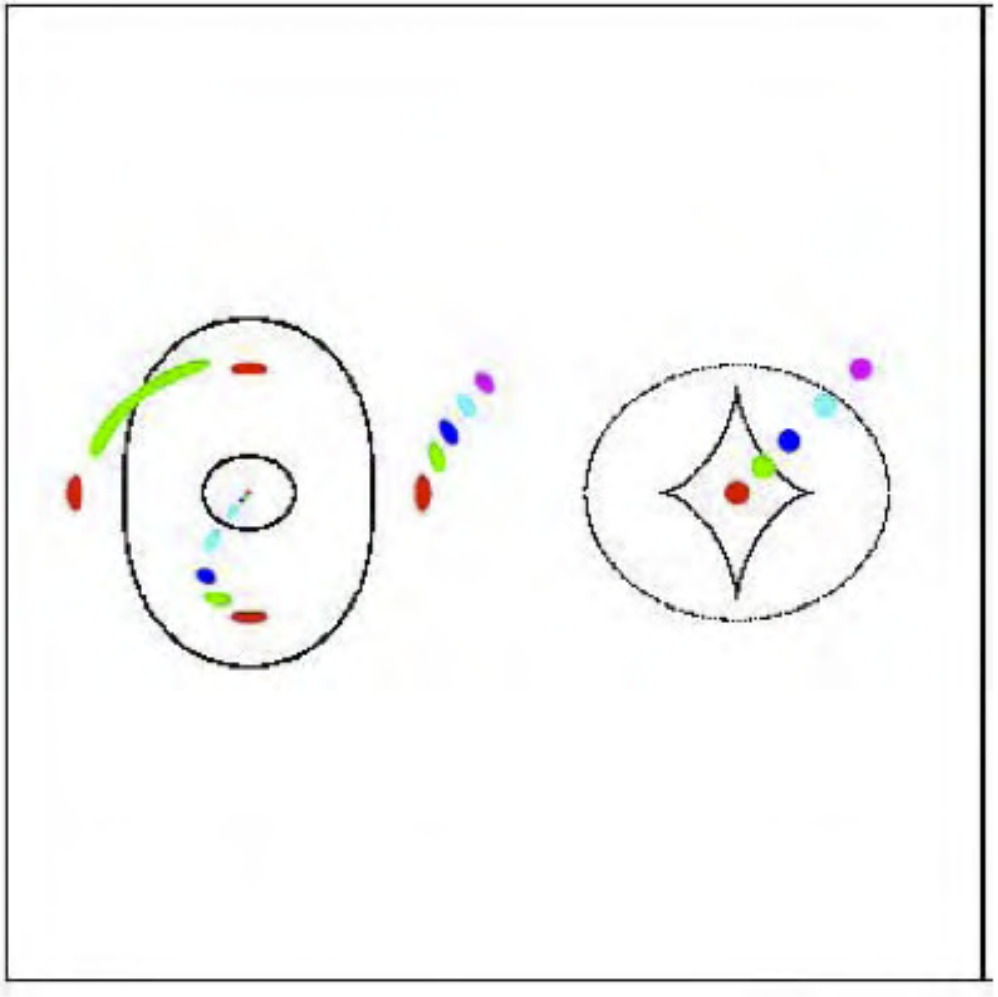

Figure 12: from [7]

$$z = 2.7793 \pm 0.0003 \qquad \frac{\mathrm{CO}(3-2)}{\mathrm{CO}(1-0)} = 0.56$$

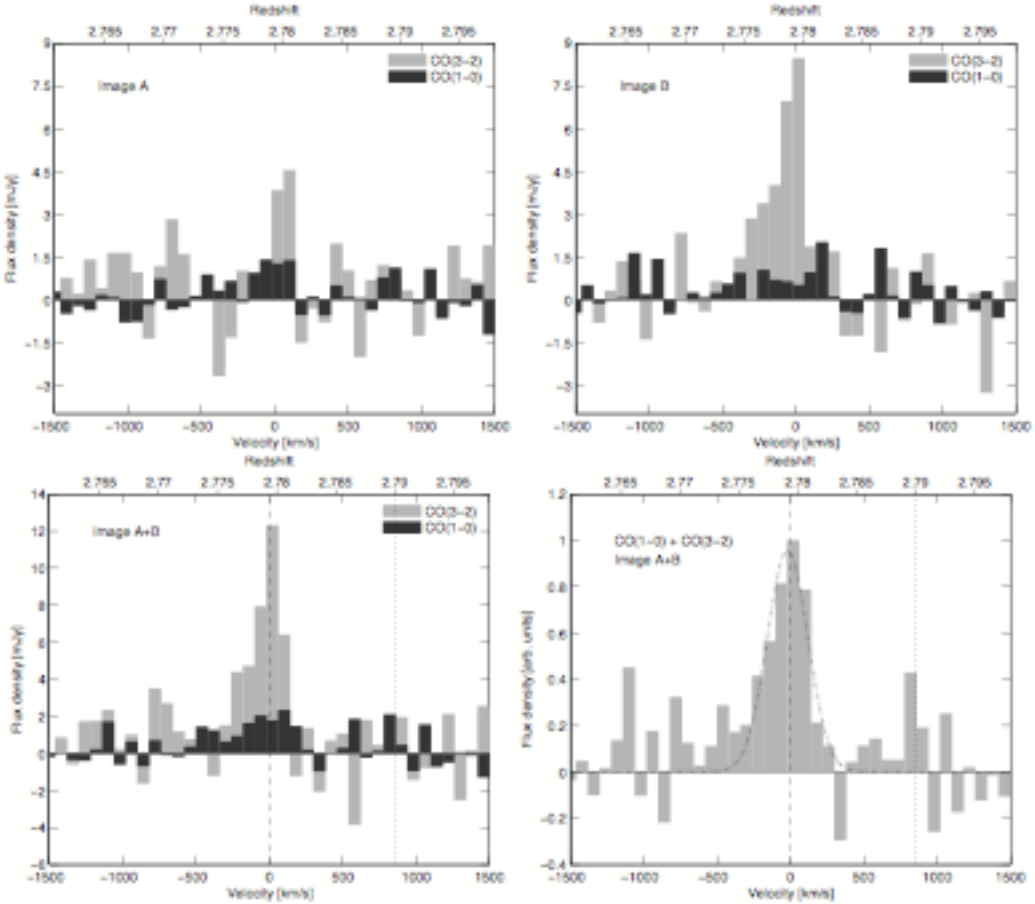

Fig. 6. CO(1–0) and CO(3–2) spectra as function of velocity and redshift, showing that both emission lines originate from gas at the same systemic velocity. The upper panels show individual spectra toward the positions of image A and B. The lower left panel shows the combined spectrum, in which we also indicated the derived redshift $z = 2.7795$ (dashed line) which is different from the redshift derived by GO10 ($z \sim 2.79$, dotted line). The velocity resolution of both the CO(1–0) and CO(3–2) spectrum is 80 km s^{-1}. The right lower panel shows the resulting spectrum when combining the CO(1–0) and CO(3–2) spectra toward images A and B. In this panel we also display the fitted Gaussian, which is further discussed in the text.

Gas Mass and Dynamical Mass

CO-H_2 conversion.

Taking $\alpha = 0.8 M_\odot (\mathrm{K\,km\,s^{-1}\,pc^2})^{-1}$

$$M_{gas} = (1.8 \pm 0.3) \times 10^9 M_\odot$$

$$M_{dyn} = 1.16 \times 10^9 \left(\frac{\Delta V_{FWHM}}{100 km\,s^{-1}}\right) \left(\frac{L}{kpc}\right) (\sin i)^{-2}$$

Formula by Papadopoulos et al. 2000; taking <sin *i*> = 0.5; L = 1 kpc

$$M_{dyn} = (2.4 \pm 0.7) \times 10^{10}\ M_\odot$$

Comparison with other highly magnify galaxies

Table 4. Summary and comparison of physical properties of SMM J0658 and other highly magnified SMGs.

Source	SMM J0658 (1)	SMM J16359+6512 (2)	SMM J2135−0102 (3)
Redshift	2.7793	2.5174	2.3259
Magnification	80–115	45 ± 9.5	32.5 ± 4.5
Submm flux density (mJy)	∼0.5	∼0.8[a]	∼3
$L_{CO(1-0)}$ (10^8 K km s^{-1} pc^2)	22.6 ± 3.6	–	173 ± 9
$L_{CO(3-2)}$ (10^8 K km s^{-1} pc^2)	12.7 ± 2.0	37 ± 2	117.6 ± 0.9
M_{gas} (10^9 $M_\odot$)	1.8 ± 0.3	4.5 ± 1.0	14 ± 1
M_{dyn} (10^9 $M_\odot$)	$(13 \pm 4)(L/1\mathrm{kpc})^b$	15 ± 3	40 80
L_{FIR} ($10^{12} L_\odot$)[c]	0.3 ± 0.03	1.6 ± 0.4	2.3 ± 0.1
SFR ($M_\odot$ yr^{-1})	100 150	∼500	400 ± 20
SFE ($L_\odot$ $M_\odot^{-1}$)[d]	170	∼320	165 ± 7
M_{dust} (10^7 $M_\odot$)	$1.1^{+1.8}_{-2.3}$	1.9 ± 0.3	∼15
T_{dust} (K)	$33 + 5$	$51 + 3$	$(30; 57 + 3)^e$

Notes. All values have been corrected for the individual gravitational magnification factors. [a] Flux density measured at 850 μm; the other two flux densities were measured at 870 μm. For a submm spectral index of ∼3 the flux difference between the two wavelengths is less than 3%. [b] L is the size of the CO-emitting region. [c] Rest-frame infrared luminosity between wavelengths $\lambda = 8$–1000 μm. [d] Star formation efficiency, defined as L_{FIR}/M_{gas}. [e] Dust temperatures for the extended and clumpy dust component reported by Danielson et al. (2010) for a two-phase model. (1) This work; (2) Kneib et al. (2004, 2005); (3) Danielson et al. (2010).

SMG are usually ULIRGS

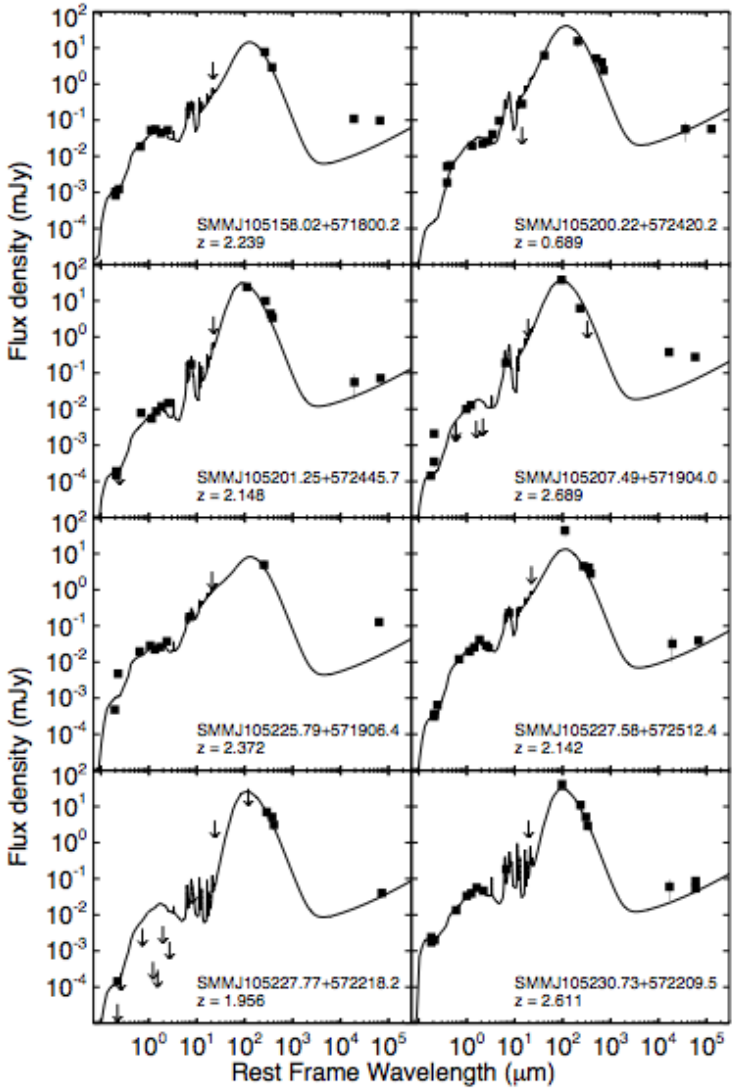

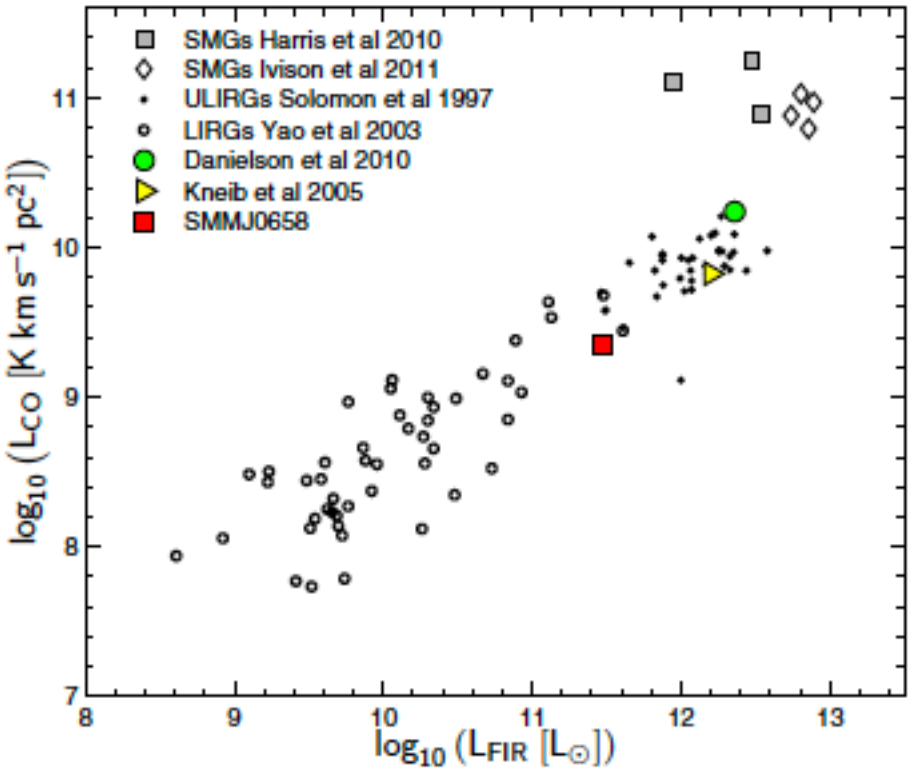

Fig. 7. Far-infrared luminosity versus CO(1–0) luminosity for the three galaxies summarized in Table 4: SMM J0658 (this study), SMM J16359+6612 (Kneib et al. 2005) and SMM J2135−0102 (Danielson et al. 2010). Local LIRGs and ULIRGs (Yao et al. 2003; Solomon et al. 1997) and high-redshift submm galaxies (Harris et al. 2010; Ivison et al. 2011) are also shown. Because SMM J16359+6612 has not been detected in CO(1–0), the CO(3–2) line luminosity was converted using $r_{31} = 0.6$ (which appears appropriate for SMGs, see Sect. 3.2.3). SMM J0658 is the least FIR-luminous high-redshift galaxy.

Enters ALMA Cycle 3 Observations, band-3 and band-6

The Cosmic Seagull

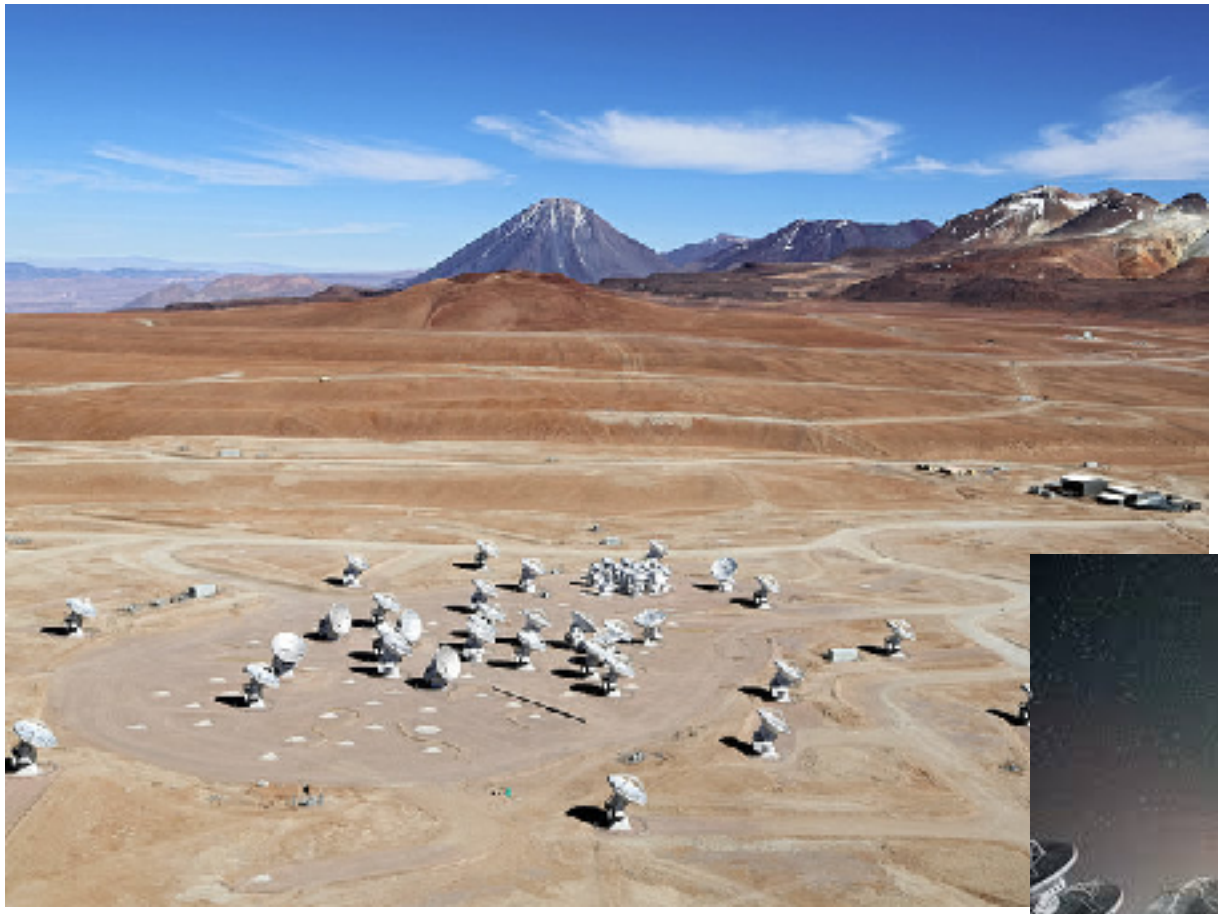

The best model of the Bullet Cluster

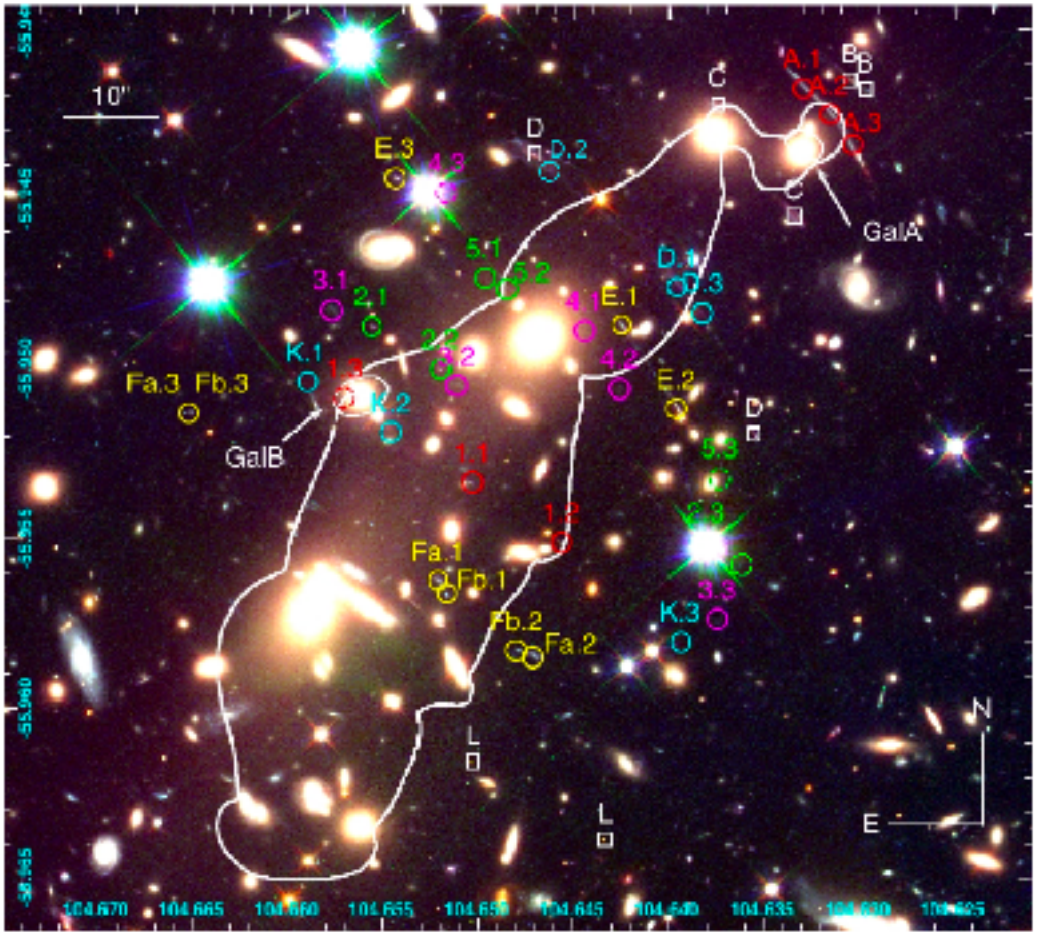

Fig. 1. Color HST image of the main cluster component of 1E 0657–56 (Blue: *F606W*, green: *F814W*, red: *F160W*). Multiple images considered in this work are marked with color circles (dashed line circles mark the qualified but not confirmed positions of counter images), the spectroscopically confirmed multiply imaged systems are system A (Mehlert et al. 2001) and K (Gonzalez et al. 2010). White squares are referring to Bradač et al. (2009) systems, which we have revised and we did not include in our modeling. The new identification of system A is shown in red and the new identification of system D is shown in cyan (see also Fig. 7). System D is a multiply imaged candidate and due to extended morphology is not a part of model constraints. The white line represents a critical line corresponding to $z = 3.24$.

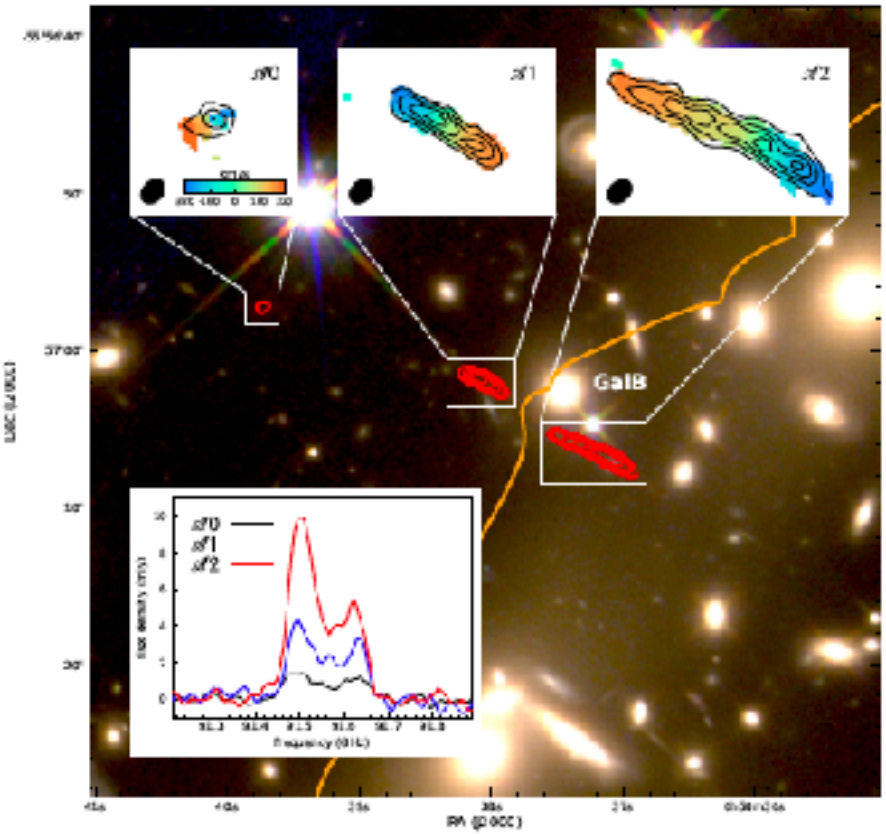

Fig. 1.— HST composite (WFPC2/F814W, WFPC3/F110W and F160W) image and contours (intervals from 20% to 80% of 1.16 mJy beam $^{-1}$ peak intensity) from ALMA band-6 continuum centered at 231 GHz showing the structure of the 'Cosmic Seagull' near a bright galaxy (GalB). The orange line represents the critical line in the lens plane. Inserts at the top exhibit the CO(3–2) rotation velocity map (in colours) and line intensity (in contours in intervals from 20% to 80% of 0.48 Jy beam^{-1} km s^{-1} peak intensity) for $s0$, $s1$, and $s2$. The ALMA synthesized beam (0.5"×0.7", PA= 43°) is shown as black ellipses. Notice the inverted rotation curves for $s2$ and $s1$, caused by the lensing effect. The central velocity, as well as the velocity range, of $s0$ is the same as for $s2$ and $s1$. The insert at the bottom shows the observed spectra from all of the 'Cosmic Seagull' images ($s0$, $s1$ and $s2$). The spectra have been smoothed to a final resolution of 23.4 MHz (78 km s^{-1}) to improve visualization. The effect of differential magnification (not corrected in the figure) can be significant in the low frequency (high velocity) side of the CO(3–2) emission line, as it approaches the critical line. The similarity of the profiles confirms that $s0$, $s1$ and $s2$ are three images of the same object.

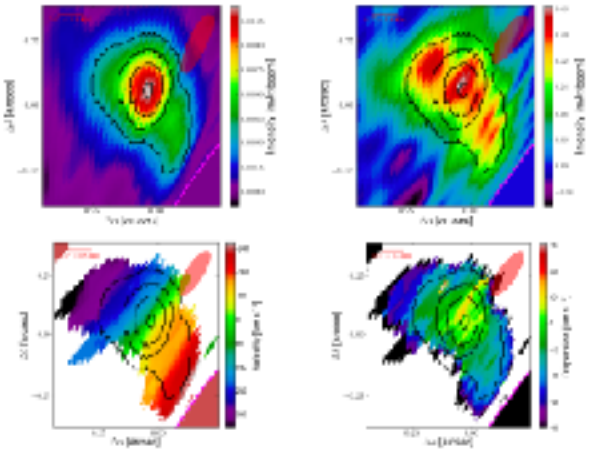

Fig. 2.— Lens model reconstruction of the 'Cosmic Seagull' source. The maps show the $s2$ reconstructed source morphology for (a) continuum centered at 231 GHz, (b) CO(3–2) surface brightness, (c) CO(3–2) rest frame velocity, and (d) CO(3–2) velocity dispersion. The magenta line represents the caustic curve (regions of highest magnification) in the source plane. The black contours show the continuum (intervals from 20% to 80% of 1.16 mJy beam^{-1} peak intensity). The light red ellipse shows the ALMA synthesized beam in the source plane, providing a mean resolution of ~ 620 pc (~ 0.078") along the plane.

$$Mdyn = (6.3 \pm 0.7) \times 10^{10}\ M_{\odot}$$

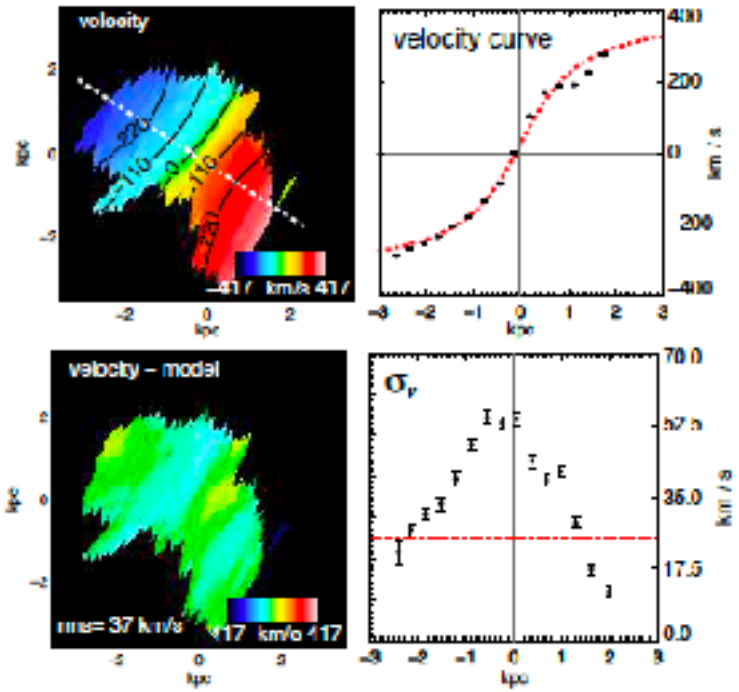

Fig. 3.— Kinematic analysis for the 'Cosmic Seagull' reconstructed δf2 source using a thick disk model. (a) Reconstructed CO(3–2) velocity field with contours from the best fit disk model. The dashed line represents the position angle of the major axis of the galaxy derived from the best two-dimensional kinematic model. (b) Major axis rotation curve for CO(3–2) with 1 σ errors (black) and the best fit disk model (red). (c) Residual map from the best fit disk model. (d) CO(3–2) line width (σ_v) corrected by the local velocity gradient across the line of sight. The dashed red line represents the mean velocity dispersion.

The Stellar Mass

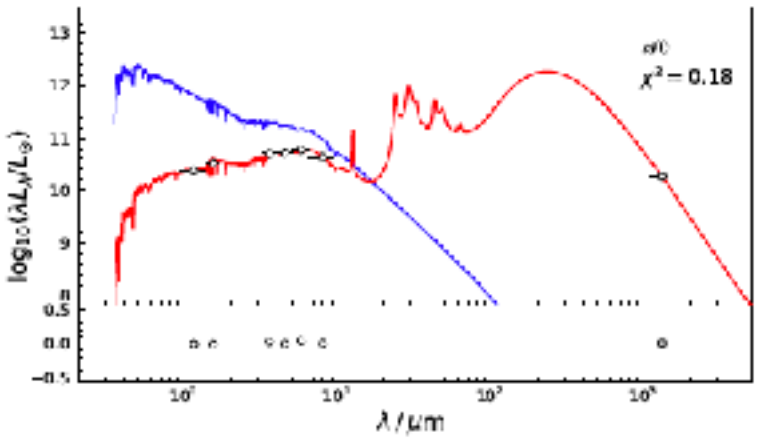

Fig. 4. Observed spectral energy distribution for sf0 using HST/WFC3 F110W, F160W bands, IRAC 3.6, 4.5, 5.8 and 8.0 μm bands, and ALMA continuum centered at 251 GHz (1.3mm) and $\mu_{sf0} = 4$ at $z = 7.7709$. We plot the best MAGPHYS SED fit comprising the unattenuated stellar continuum (blue line) and the observed (reprocessed light) emission including the cold dust emission (red line). Errors are included in quadrature with a 10 % error in the magnification. Continuum in band 3 is not included as it is not detected at sf0.

A1+A2

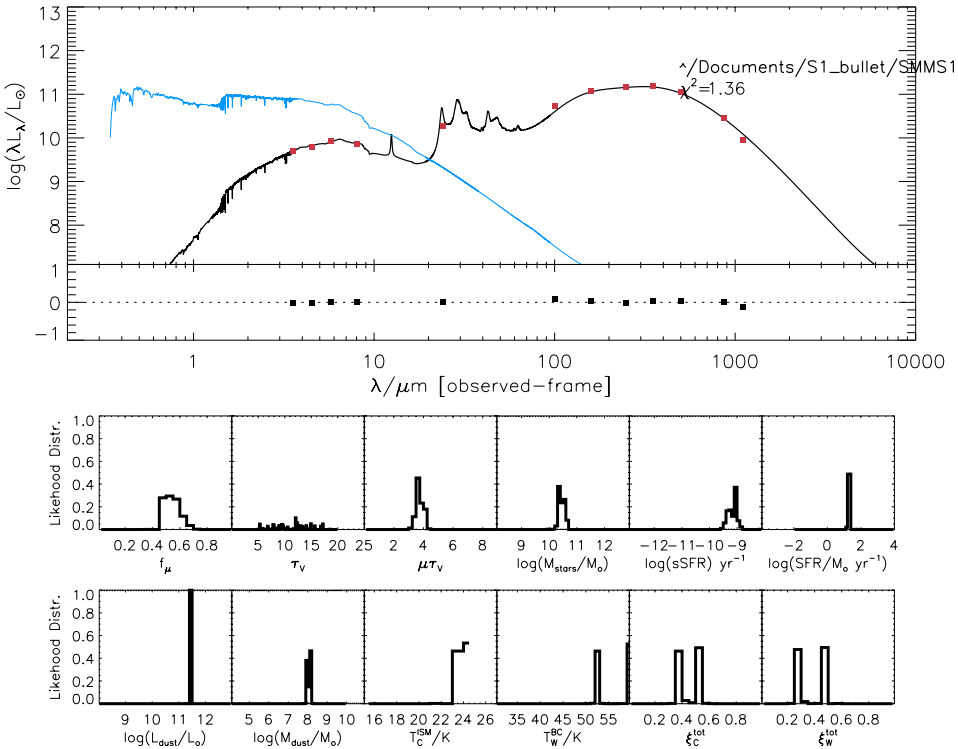

Newest Parameters

the noise levels but compose the bulk of the population at high-z.

Making use of the CO(3–2) emission line to estimate the molecular gas content (Bolatto, Wolfire & Leroy 2013) in the 'Cosmic Seagull' and following a similar approach as before, in *A*0 we find a CO(3–2) velocity integrated flux density of 228 ± 44 mJy km s^{-1} (corrected by a magnification $\mu = 4$, at 91.5 GHz). Using a classical (Solomon & Vanden Bout 2005) conversion to get the CO(3–2) luminosity, $L'_{\rm CO(3-2)}$, from observed velocity integrated flux densities, a typical ratio (Carilli & Walter 2013) of $L'_{\rm CO(3-2)}/L'_{\rm CO(1-0)} = 0.56$, and an upper limit for $\alpha_{\rm CO}$ of 3.0 M$_\odot$ (K km s^{-1} pc^2)$^{-1}$ derived from the dynamical mass ($M_{H_2} \leq M_{dyn} - M_{star}$), we estimate a maximum molecular gas content of $M_{\rm H_2} = (4.7 \pm 1.4) \times 10^{10}\ M_\odot$. Considering the estimated dust mass from the MAGPHYS fit, $M_{dust} = (1.86 \pm 0.07) \times 10^8$ M$_\odot$, this results in a maximum molecular gas-to-dust mass ratio of $M_{H_2}/M_{dust} = 300 \pm 80$. The corresponding maximum molecular gas fraction $f_{gas} = M_{H_2}/(M_{H_2} + M_{star}) \simeq 80 \pm 20\%$ indicates that baryonic mass is most probably dominated by the molecular gas as commonly found in normal high-z galaxies (Tacconi, Genzel, Neri et al. 2010; Daddi, Bourraud, Walter et al. 2010) unless $\alpha_{\rm CO}$ is reduced to 0.8 M$_\odot$ (K km s^{-1} pc^2)$^{-1}$, a value typical of disturbed ULIRG-like galaxies. Compared to the previous estimates obtained with the ATCA telescope (Johansson, Horellou, Lopez-Cruz et al. 2012) which combined *A*1 and *A*2 fluxes, after scaling to the same $\alpha_{\rm CO}$ and assuming an averaged $\mu = 30$ at those positions, we find that our results for f_{gas} are a factor of two higher, emphasizing the power of our new ALMA observations given the uncertainties introduced by differential magnification in previous *A*1 and *A*2 images.

Assuming a constant SFR, we estimate a molecular gas depletion time of $\geq 0.25 \pm 0.08$ Gyr, in agreement with those commonly seen in rotating disk galaxies.

Conclusions

- First to measure the Cosmic Seagull redshift.
- First to measure the rotation curve of the Cosmic Seagull.
- Improvement to the Bullet Cluster's lens model.
- To be continued…

Conclusions

- Clusters of galaxies acting as natural telescopes allow us to study faint SMG.
- We have detected CO for the first time using ATCA/ CABB We have refined on the redshift on the brightest SMG behind the bullet cluster.
- The derived masses are consistent with galaxies smaller than the Milky Way. Therefore S1 (SMM J0658) should be more representative of the overall population of galaxies at z ~3.
- Observations with ALMA will allow us to impose tighter constrains on the physical properties of this rather interesitng low-mass galaxy.

Acknowledgements & Gracias

- Thanks to my “ATCA friends” Bjorn Emonts, Bärbel Koribalski, Naomi McClure-Griffiths and Phil Edwards for making the reported observations possible. But above all, patience with a total beginner mm-astronomer who had never used a radio interferometer in his life.
- Thanks to everyone at ATNF and ATCA people for such a friendly environment and first class facilities.
- Maritza Lara-López and Sarah Burke-Spolaor for promoting this talk.

Clusters of galaxies

- Composition: (not just galaxies!)
  - 10^{14} Solar Masses
  - ~1 % of mass is in galaxies
  - ~10 % of mass is hot gas (10^{8} K)
  - the rest is dark matter
  - Also contains large scale magnetic fields (hard to explain their origin by initial conditions)
  - Distort the CMB through the Sunyaev-Zeldovich Effect.
- Interesting questions
  - how much mass?
  - 'slope' of central profile
  - subclumps?

Weak versus strong lensing

- Strong lensing:
  - multiple images
  - banana shaped arcs
  - $\Sigma > \Sigma_c$
  - inner parts of massive clusters/ galaxies
- Weak lensing
  - ellipse orientation is changed
  - low-mass clusters, outer parts of massive c.

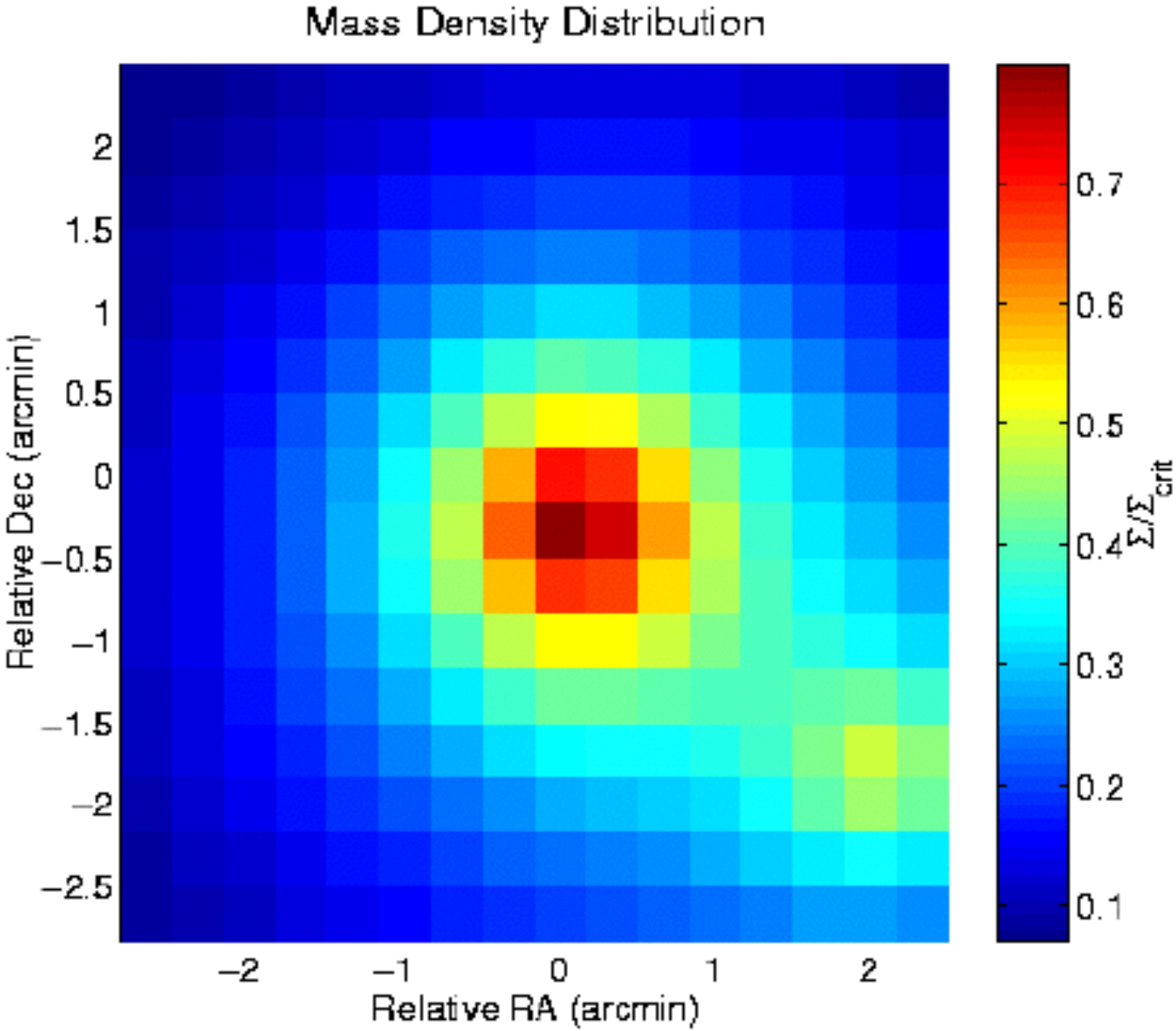
Mass Density Distribution
Relative Dec (arcmin)
2
1.5
1
0.5
0
−0.5
−1
−1.5
−2
−2.5
−2
−1
0
1
2
Relative RA (arcmin)
0.7
0.6
0.5
0.4
0.3
0.2
0.1
Σ/Σ_{crit}

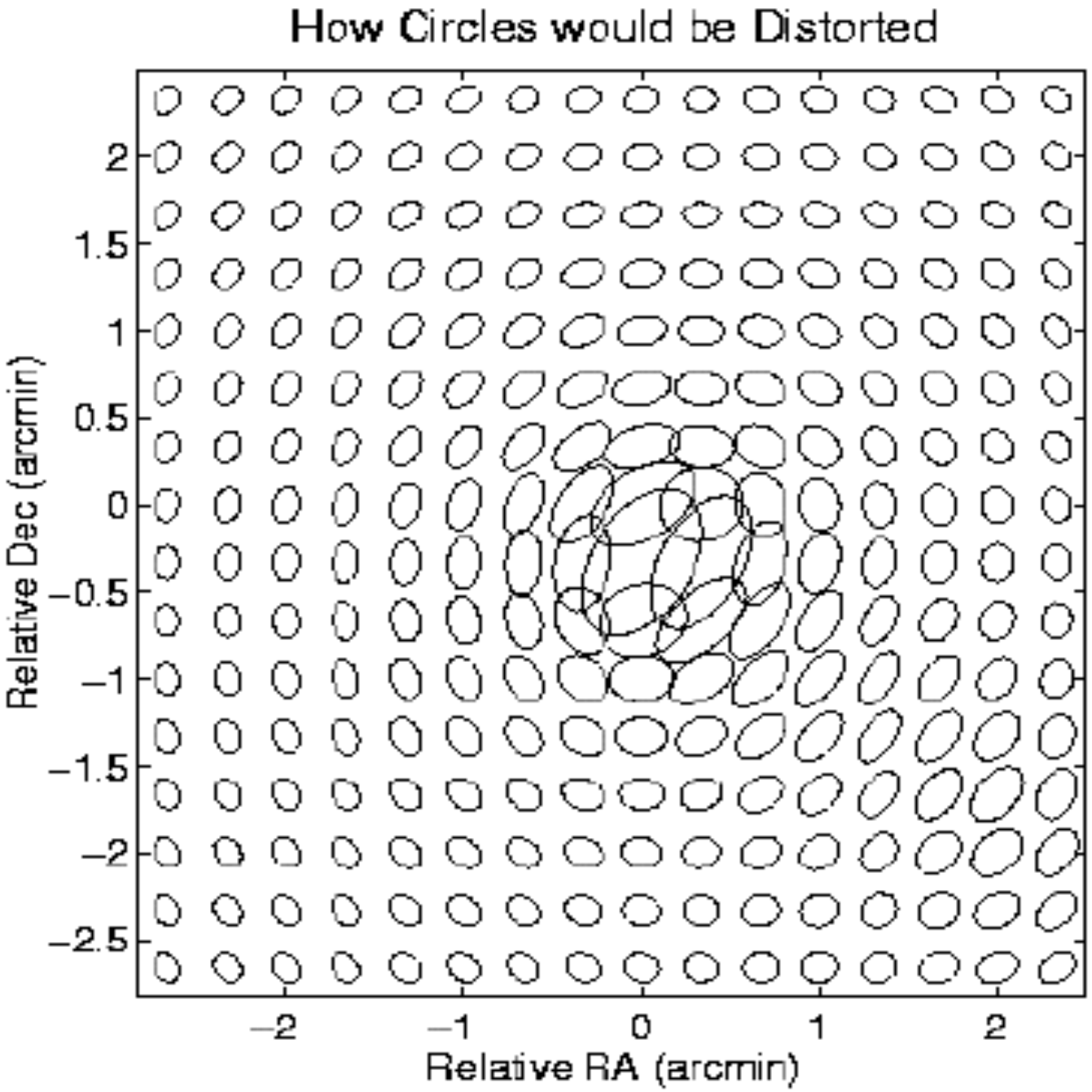
How Circles would be Distorted
Relative Dec (arcmin)
Relative RA (arcmin)
2
1.5
1
0.5
0
−0.5
−1
−1.5
−2
−2.5
−2
−1
0
1
2

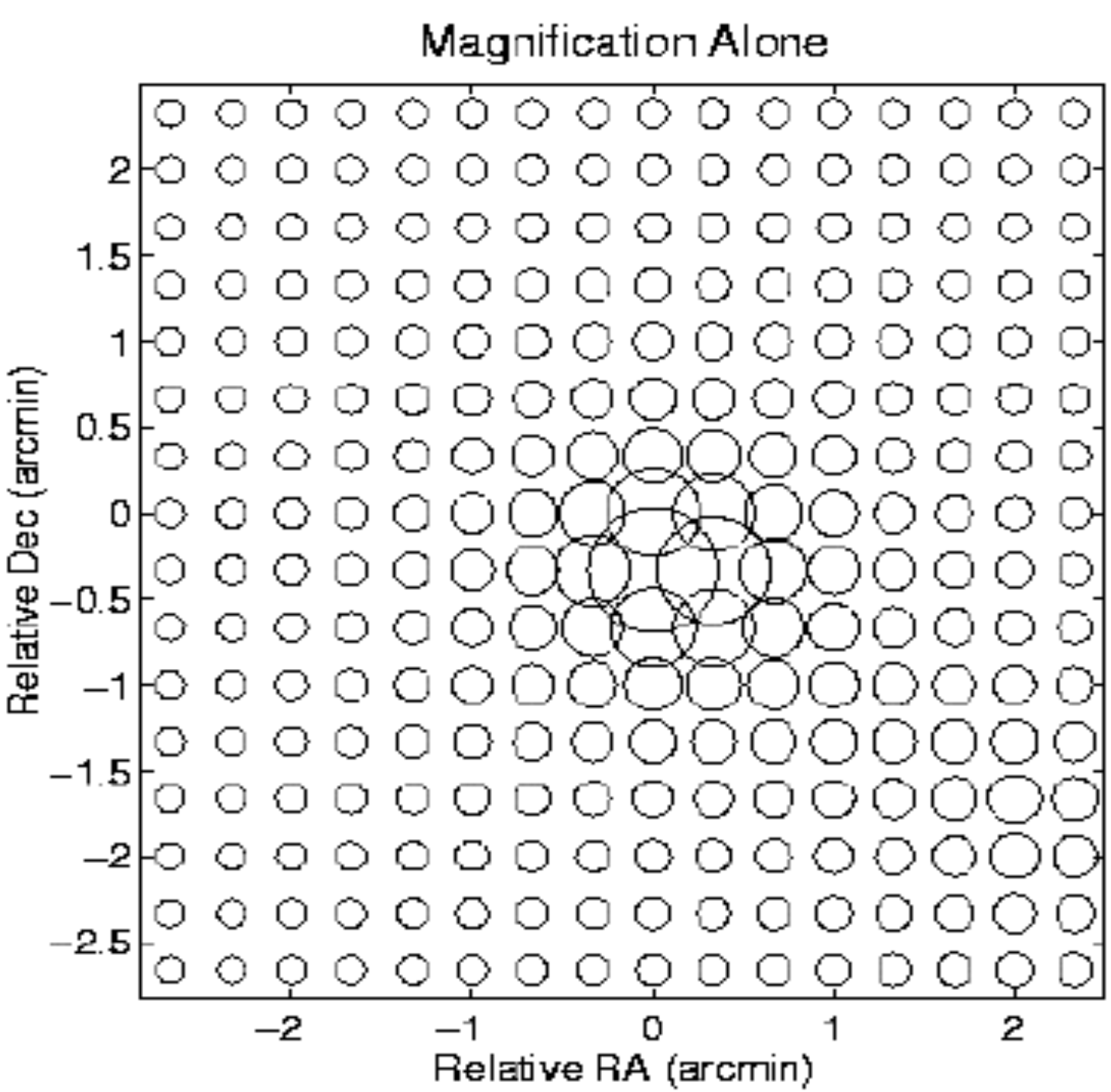
Magnification Alone
Relative Dec (arcmin)
Relative RA (arcmin)
2
1.5
1
0.5
0
−0.5
−1
−1.5
−2
−2.5
−2
−1
0
1
2

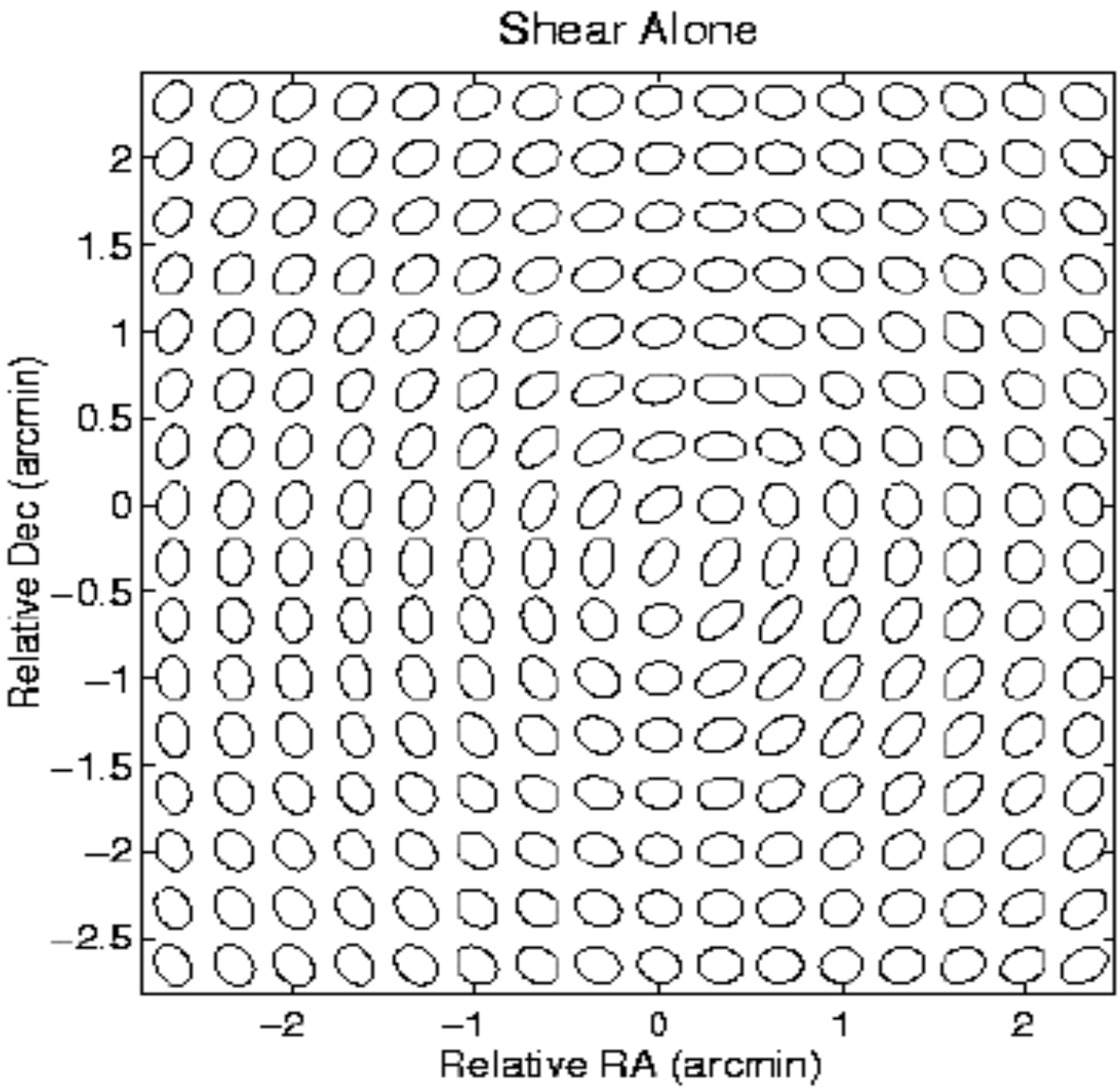
Shear Alone
Relative Dec (arcmin)
2
1.5
1
0.5
0
−0.5
−1
−1.5
−2
−2.5
−2
−1
0
1
2
Relative RA (arcmin)

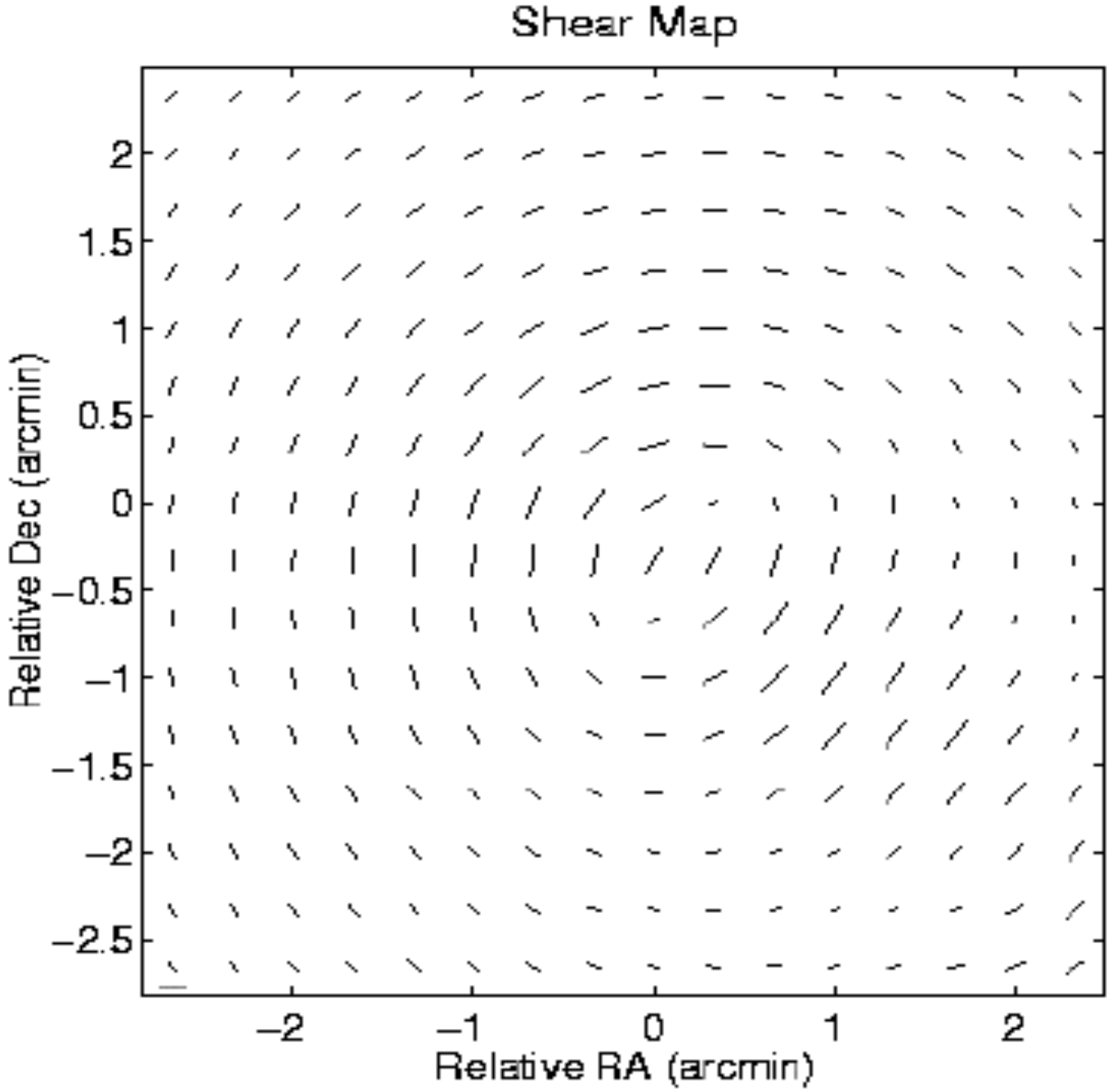
Shear Map
Relative Dec (arcmin)
Relative RA (arcmin)
2
1.5
1
0.5
0
−0.5
−1
−1.5
−2
−2.5
−2
−1
0
1
2

Shear maps: average galaxy shapes

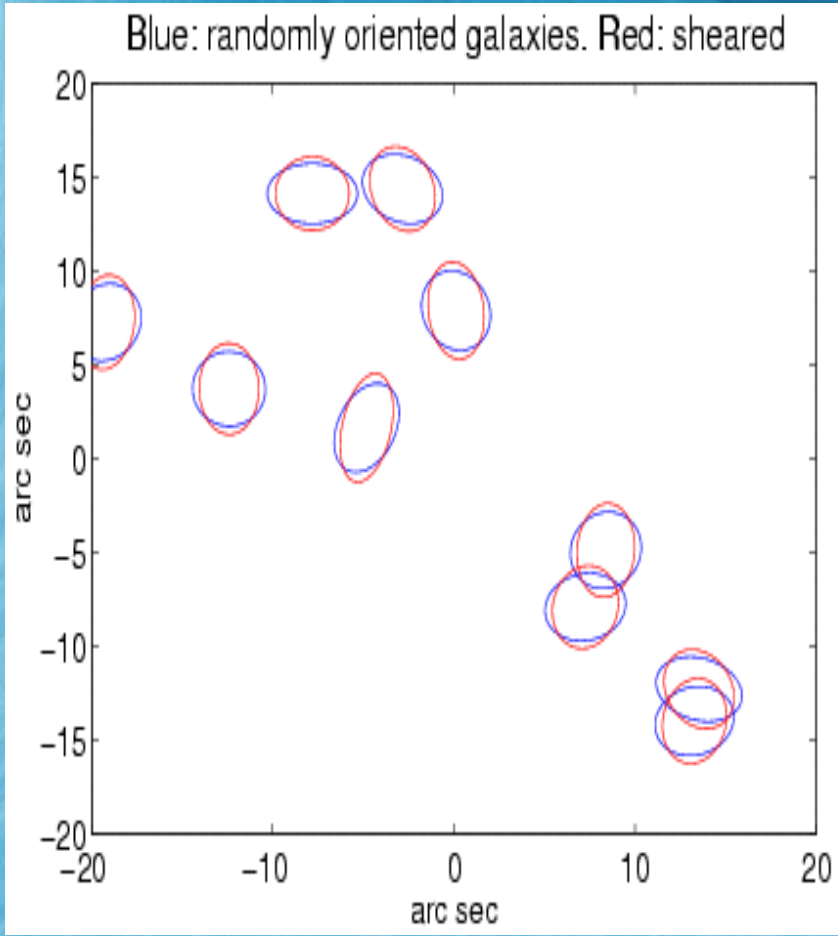

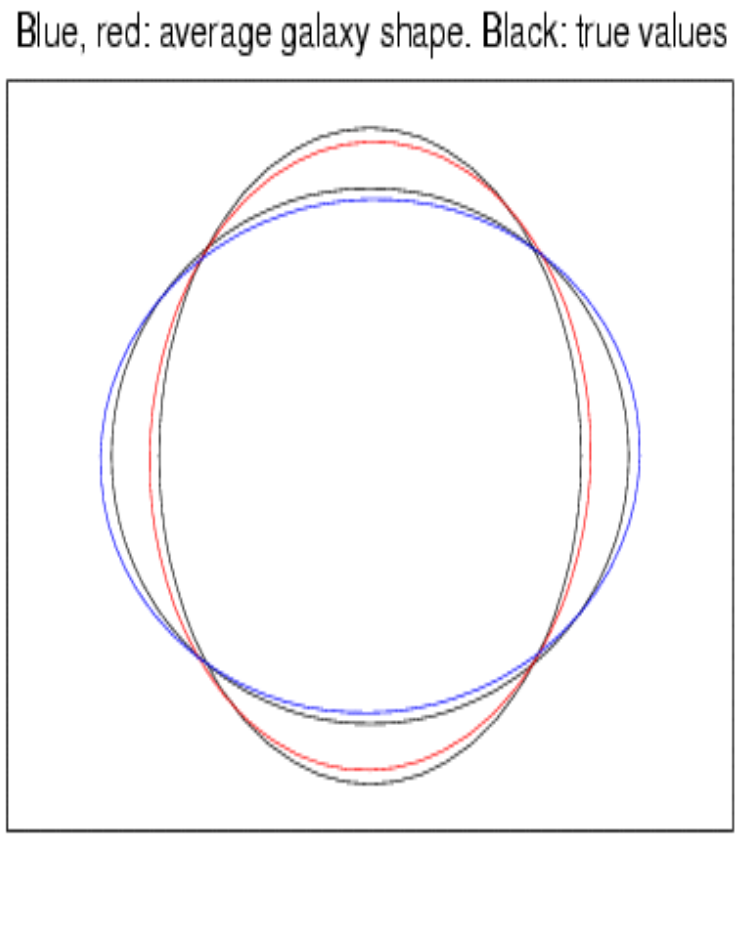

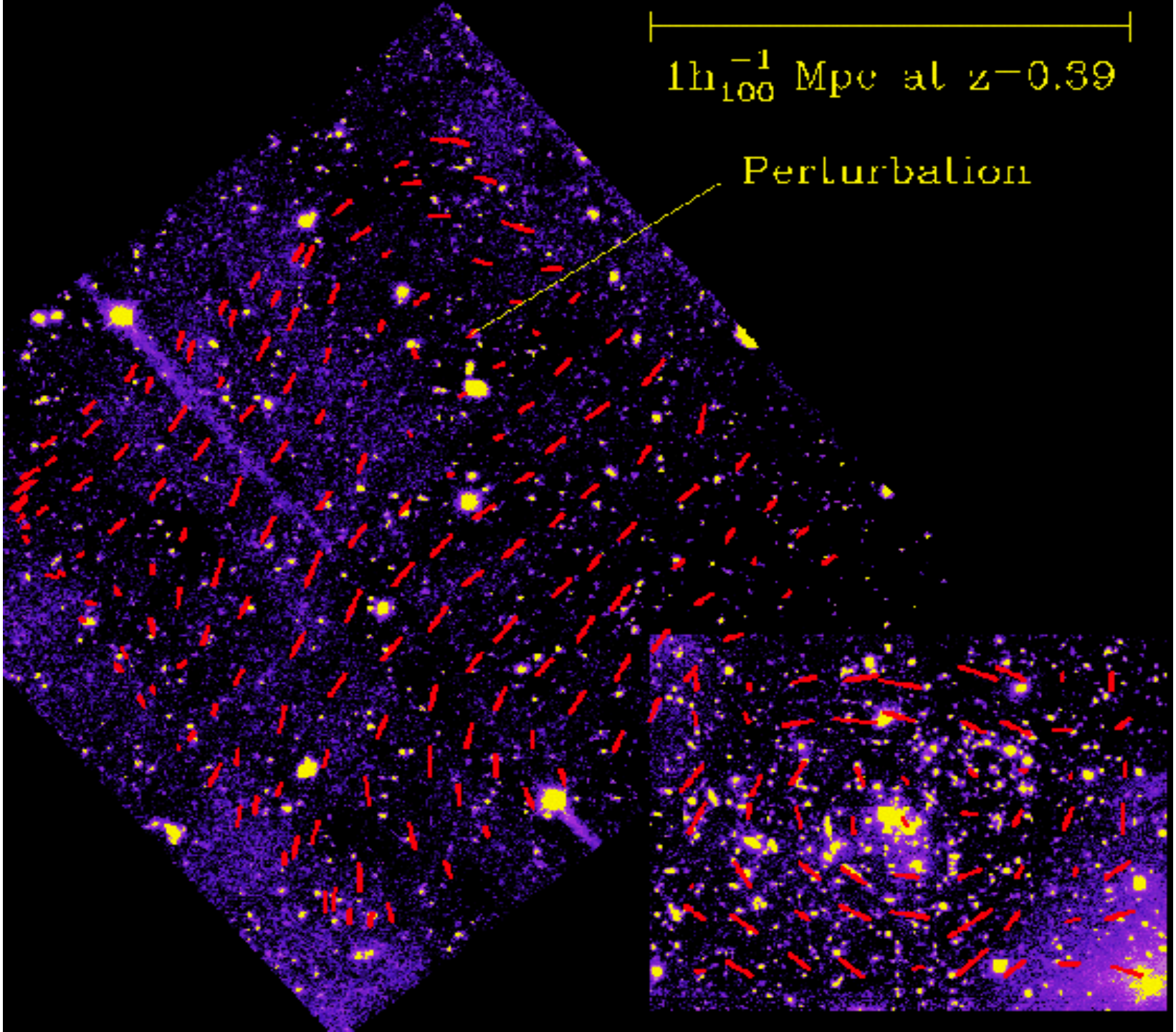
$1h_{100}^{-1}$ Mpc at z=0.39
Perturbation

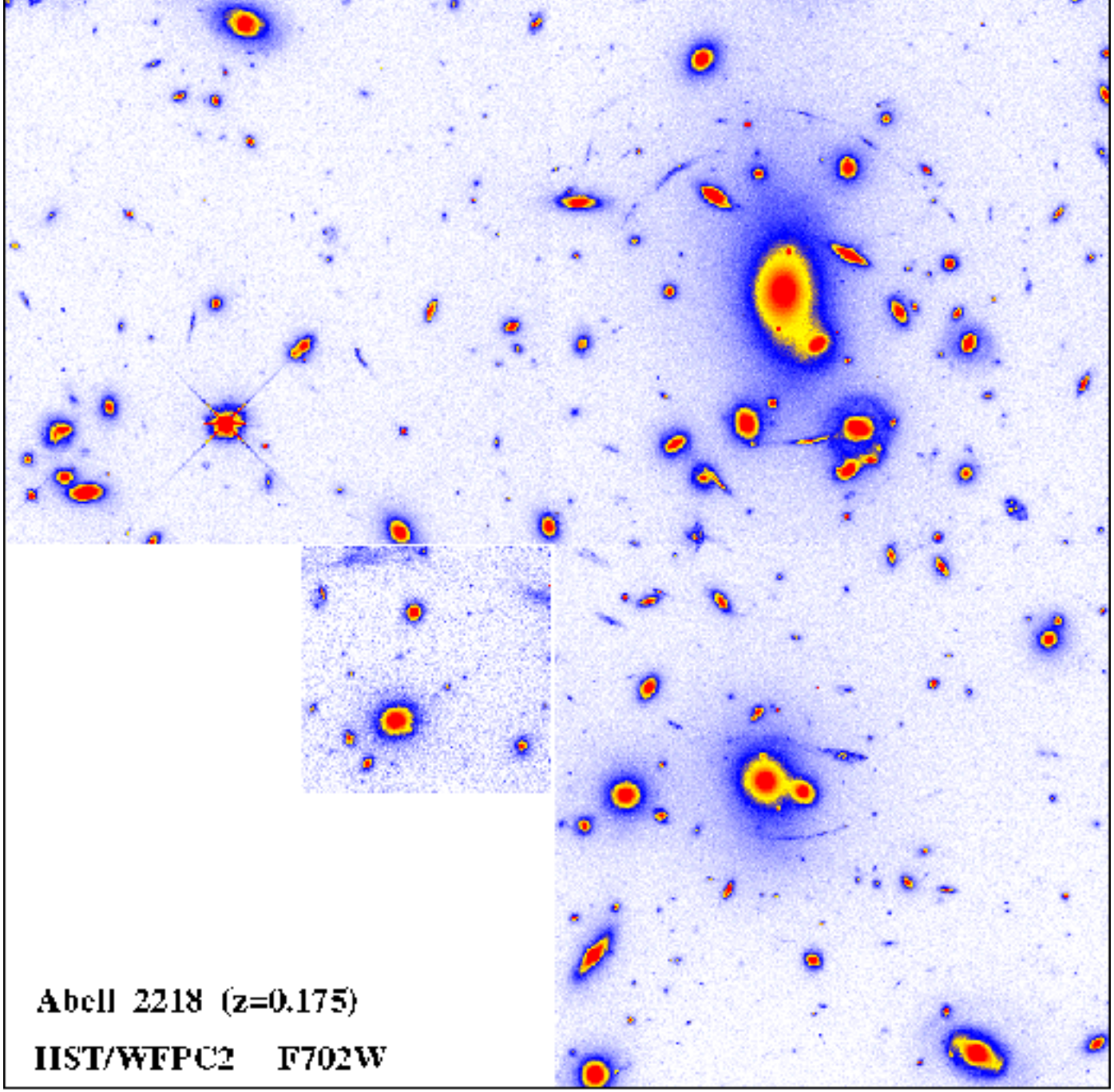

Kneib, Ellis, Smail, Couch, Sharples 1995

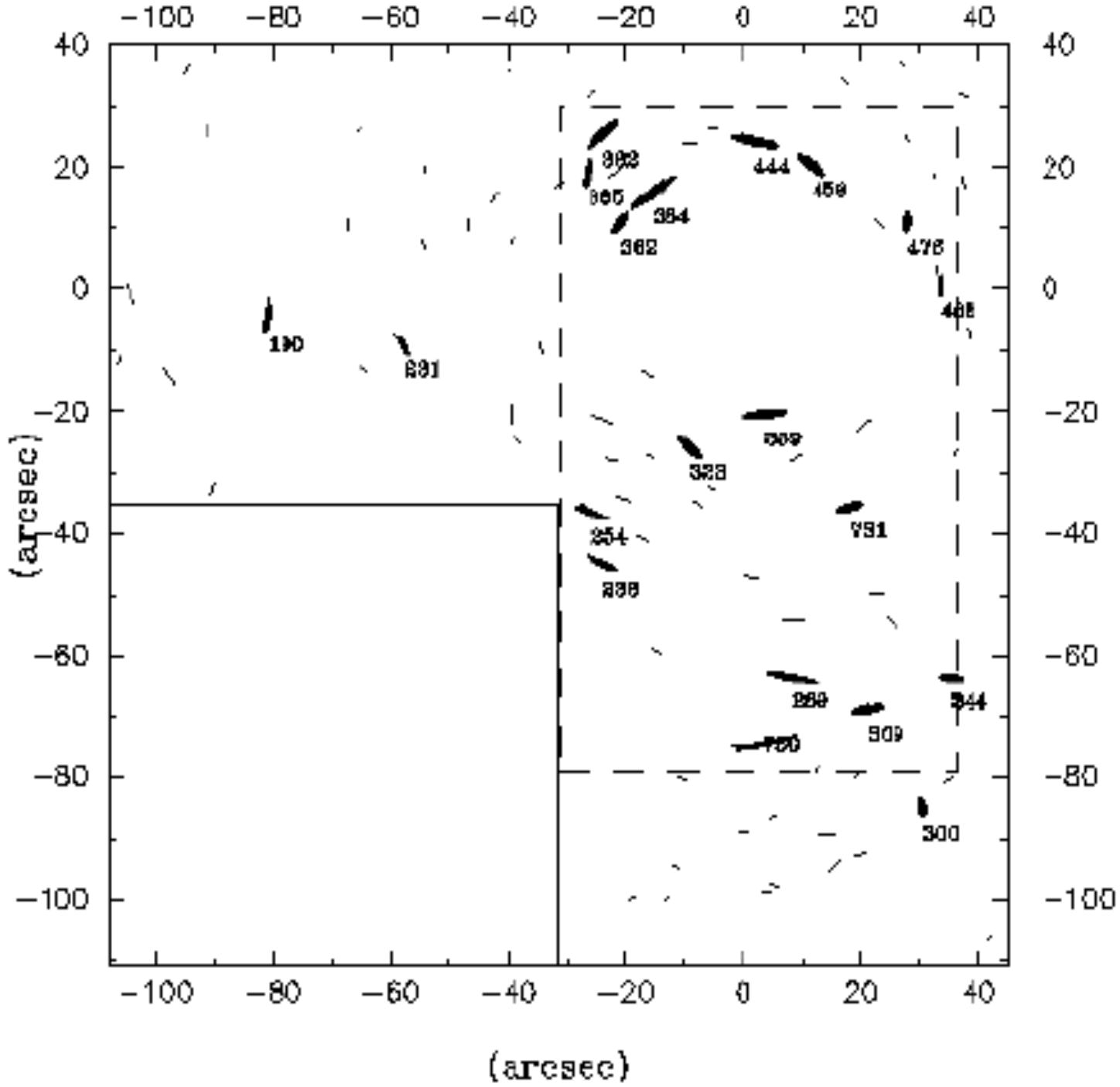
−100
−80
−60
−40
−20
0
20
40
(arcsec)
(arcsec)
444
456
384
362
476
190
331
509
328
254
236
731
269
244
309
760
300

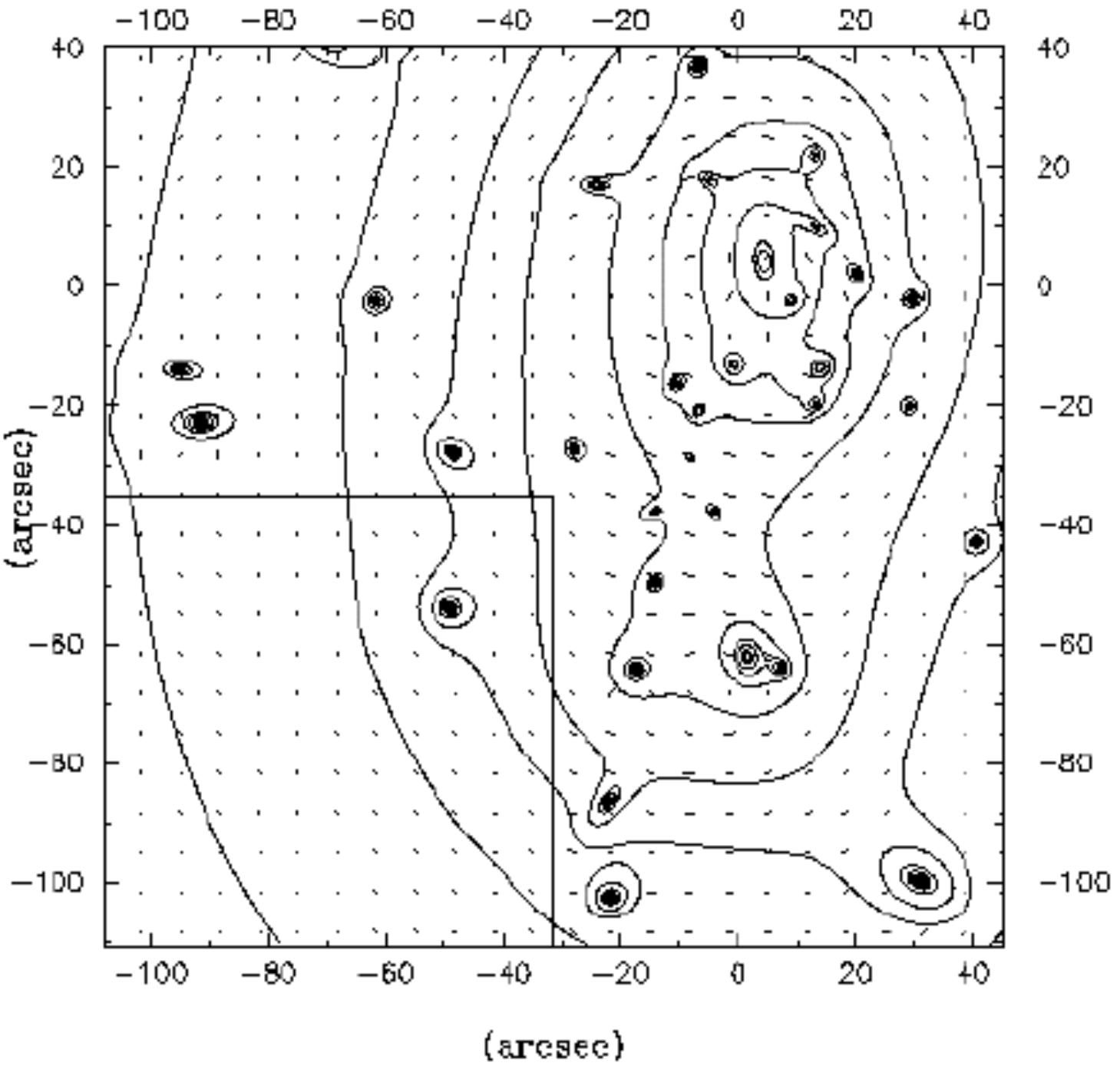
−100
−80
−60
−40
−20
0
20
40
(arcsec)
(arcsec)

Gravitational telescope

- Systematic scan of high magnification regions for Lyman-a emission at z>5
- A2218
  - 2 images, 1 source fits lens model well
  - only 10^6 M_o - first stars?
  - recently found z~10 galaxy this way!

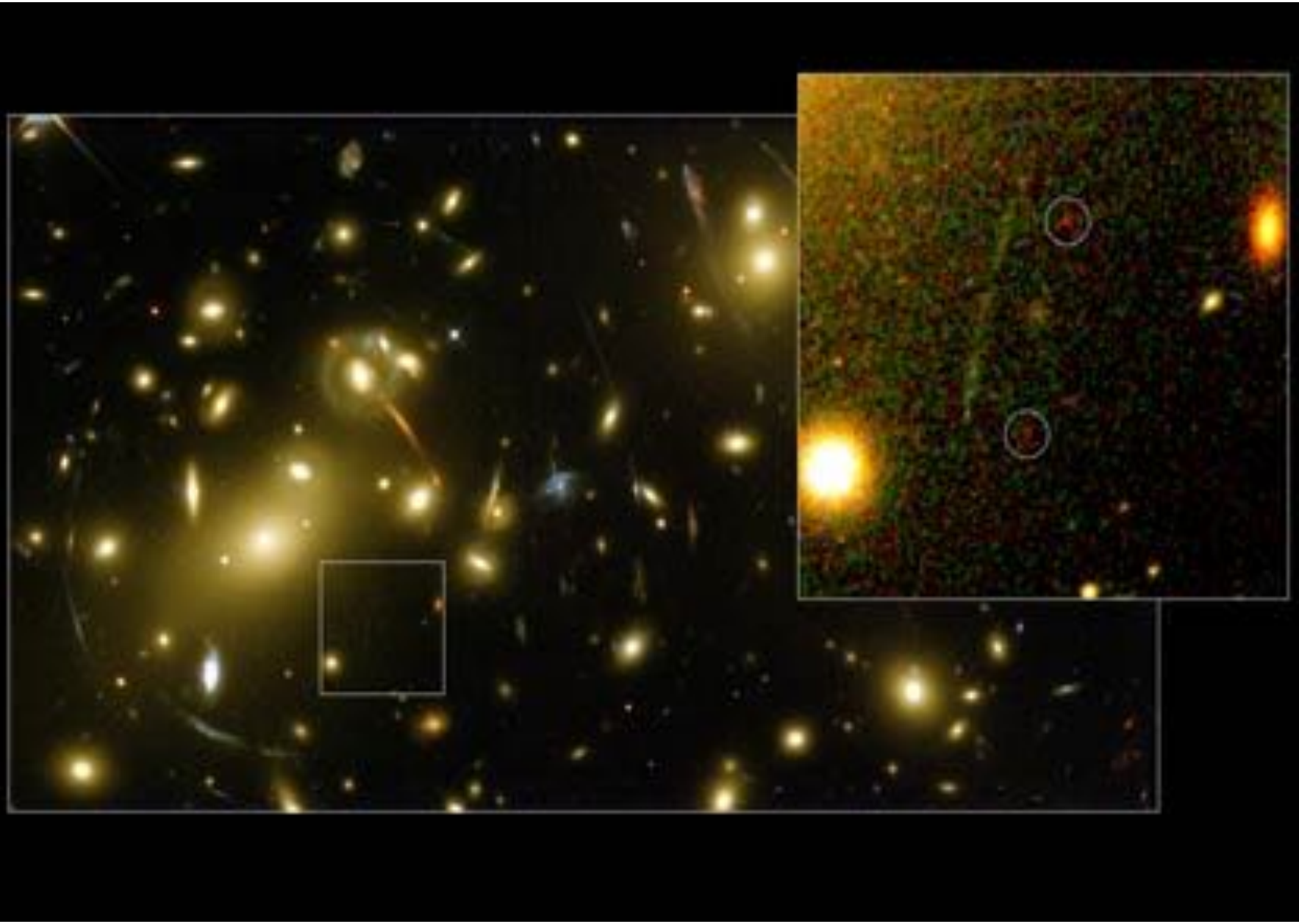

Cluster weak lensing: results

- Observations
  - MS1054
  - Dahle et al 2002
- Analysis of shear maps
  - fit parameters of eg. isothermal sphere
  - recovery of circular profile
  - 2d reconstruction

MS1054

- z=0.83 one of the highest z clusters
- Studied by both
  - Clowe et al. Keck
  - Hoekstra et al. HST
- see Marshall et al for comparison of both

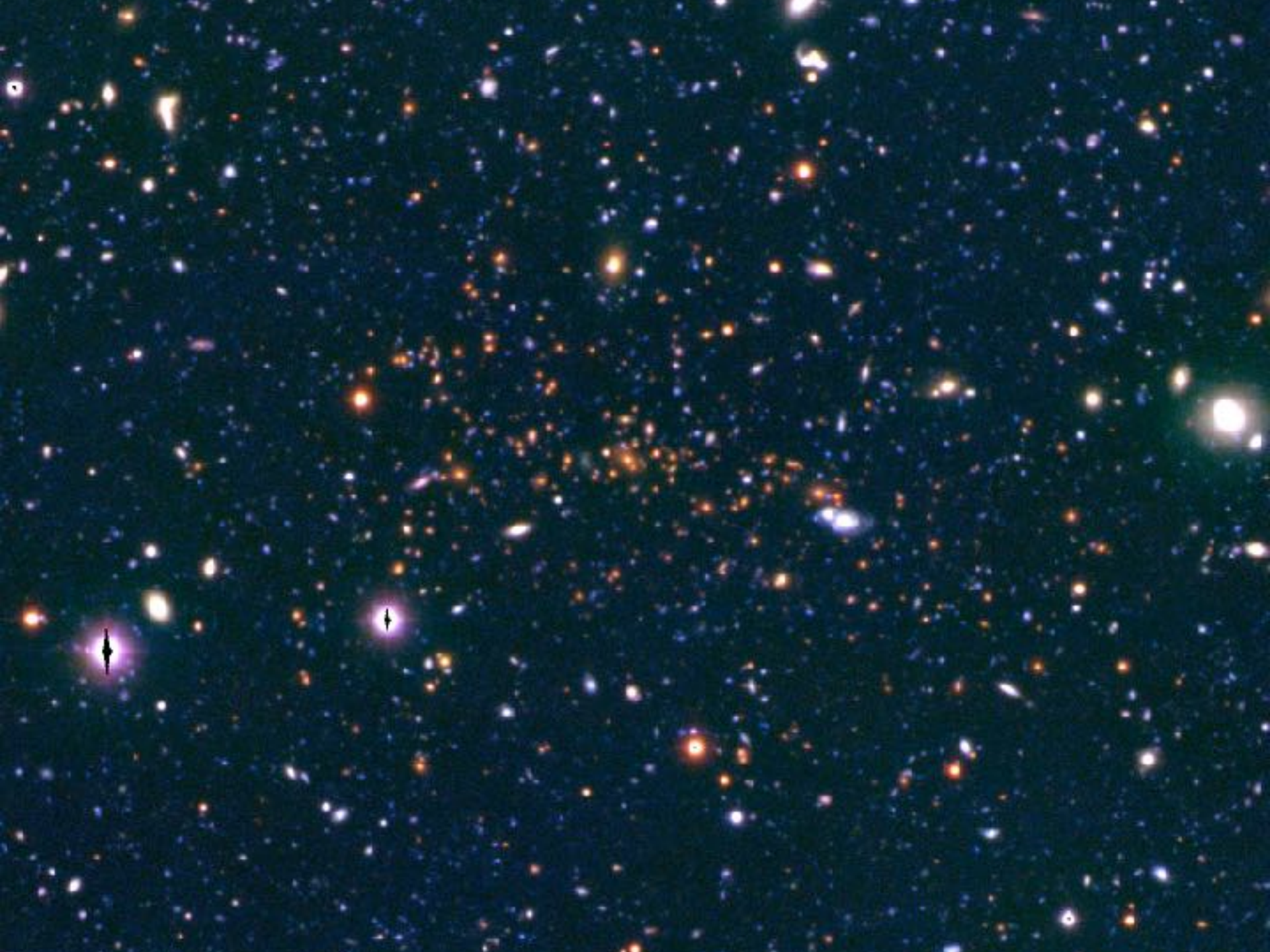

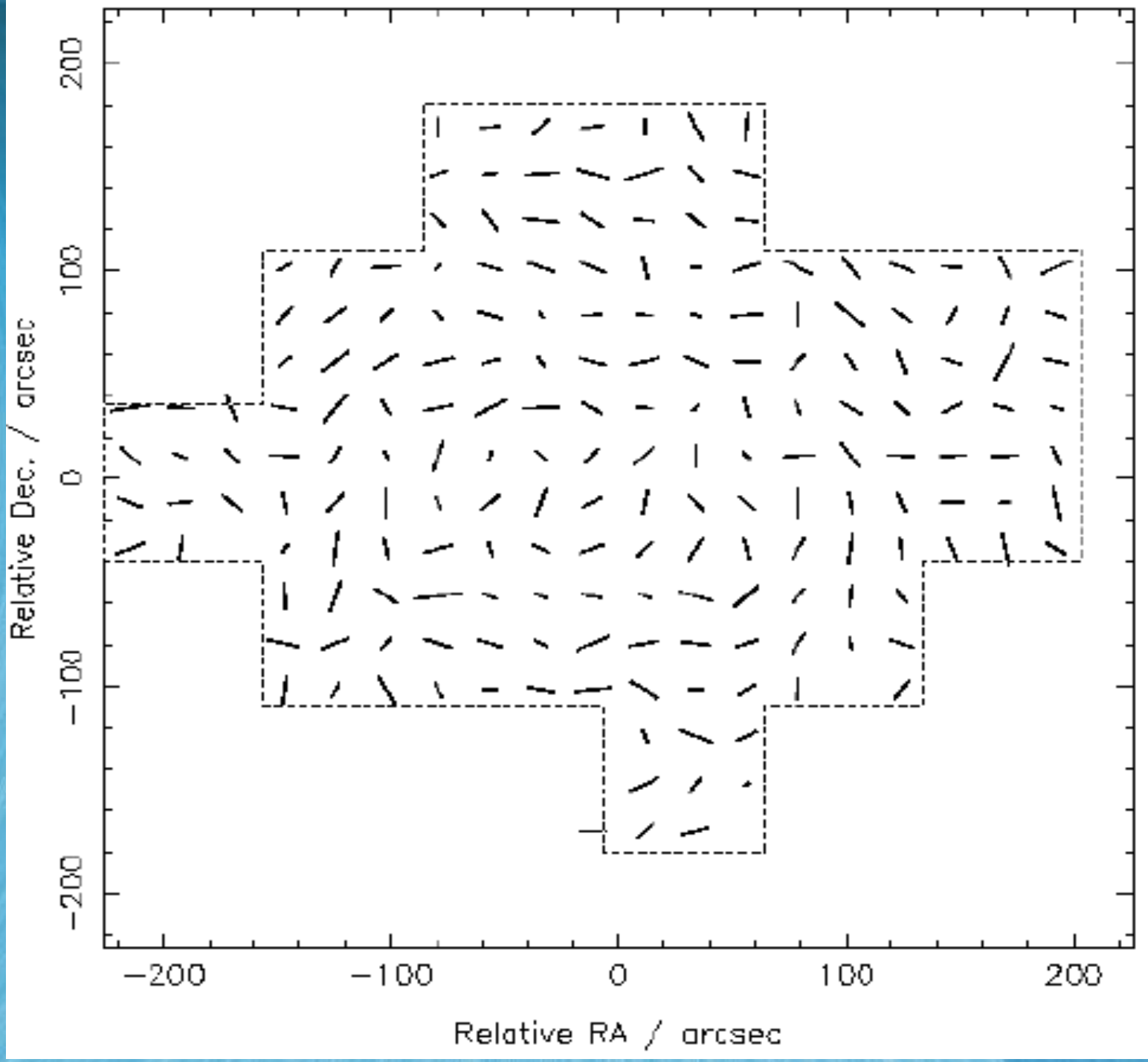
200
100
0
−100
−200
Relative Dec. / arcsec
−200
−100
0
100
200
Relative RA / arcsec

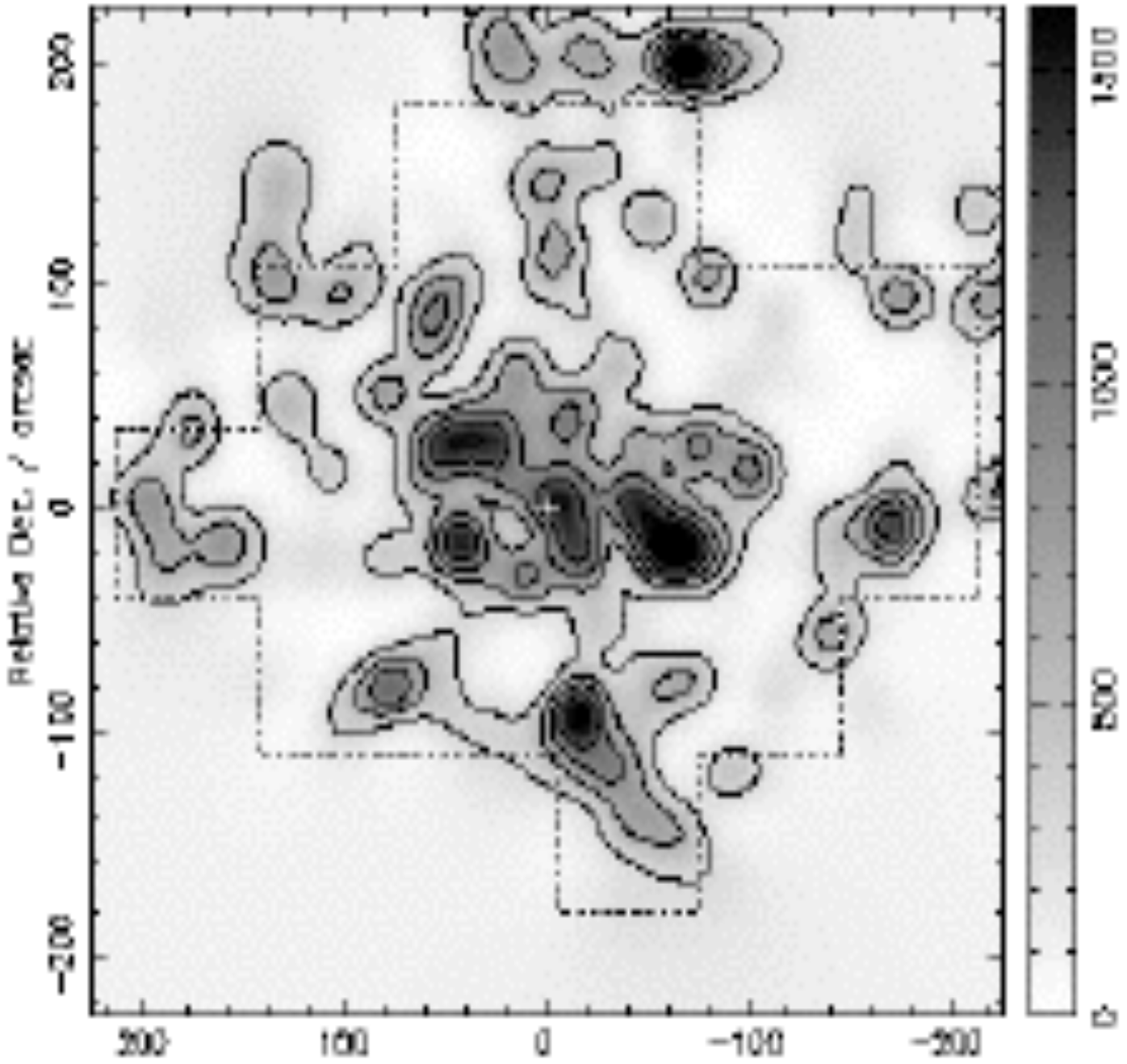
200
100
0
−100
−200
Relative RA / arcsec
Relative Dec. / arcsec
1000
500
0

HST

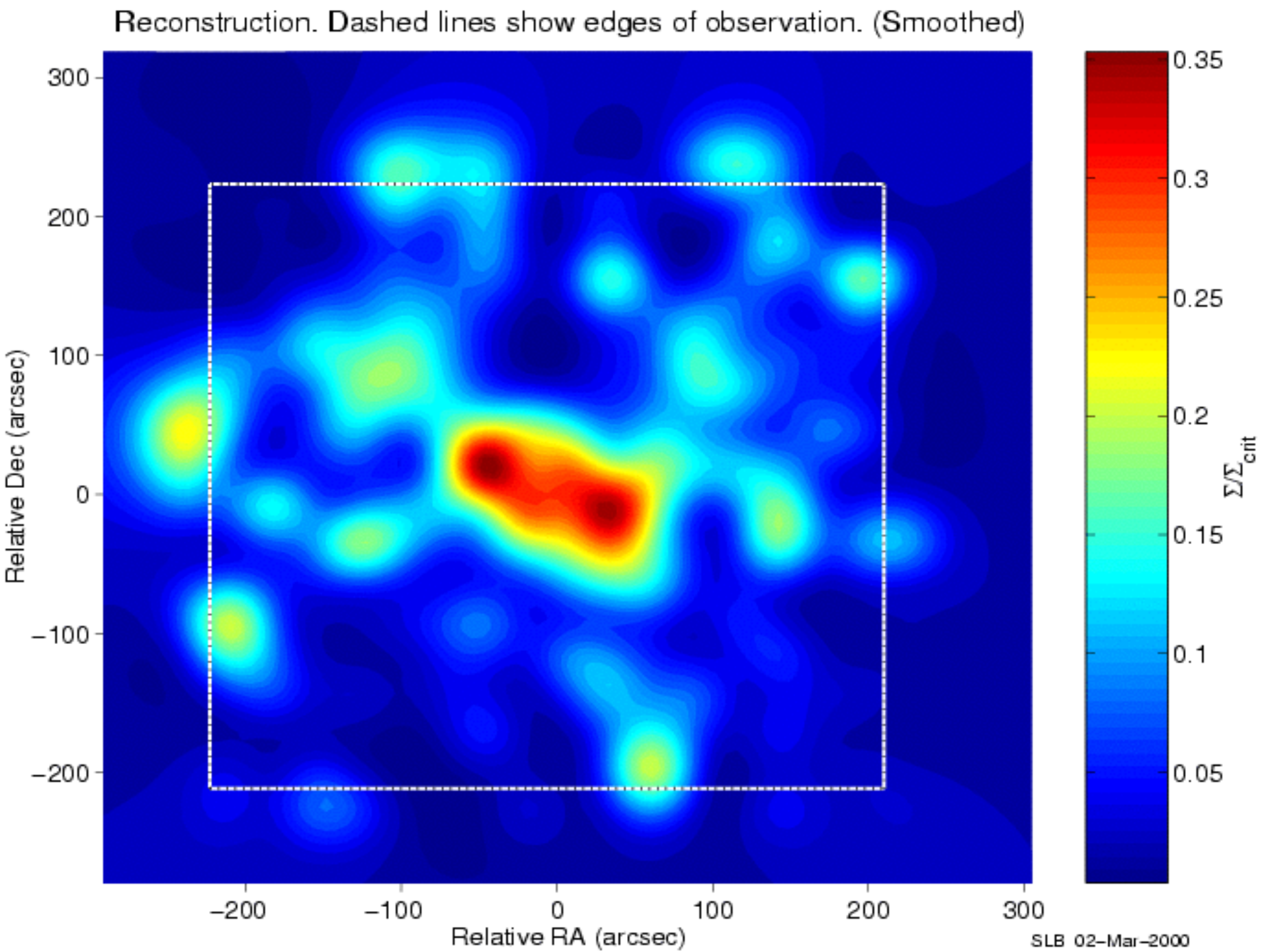
Reconstruction. Dashed lines show edges of observation. (Smoothed)
300
200
100
0
−100
−200
Relative Dec (arcsec)
−200
−100
0
100
200
300
Relative RA (arcsec)
0.35
0.3
0.25
0.2
0.15
0.1
0.05
Σ/Σcrit
SLB 02−Mar−2000

Largest single survey so far

- X-ray flux selected
- 38 clusters at $0.15 < z < 0.35$
- Field of view: 20' x 20' (UH8k camera)
- 2 colour imaging: I, V
  - improves selection of background galaxies
- Dahle, Kaiser, Irgens, Lilje, Maddox 2002

Deep optical images

William Herschel Telescope
La Palma, Canaries

16’x8’ arcmin
R<25.5
30 (15) gals/sq. arcmin

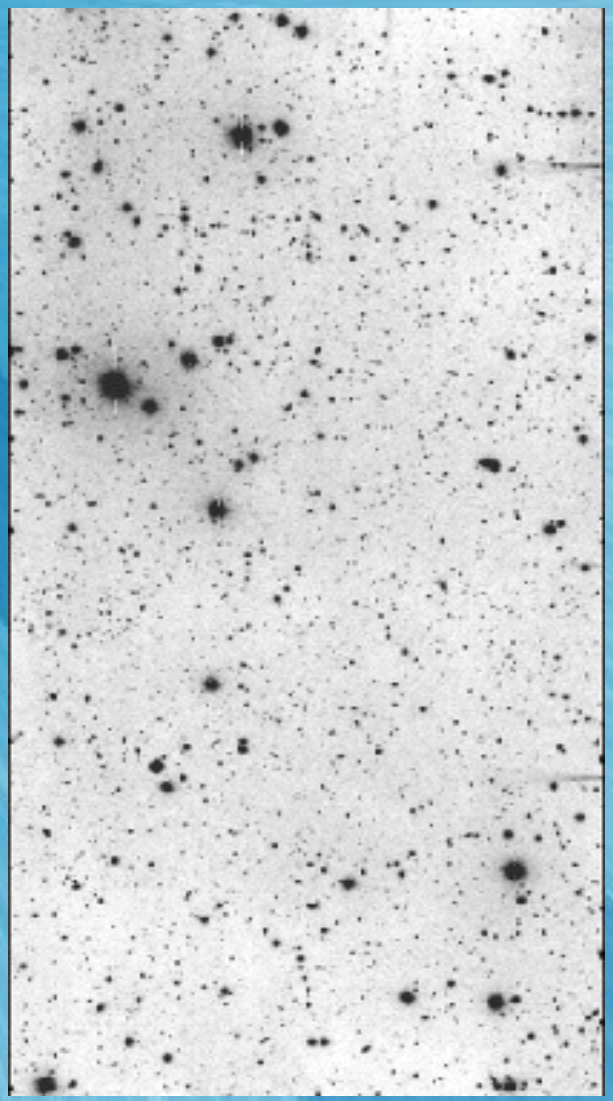

PSF anisotropy ε swirl patterns

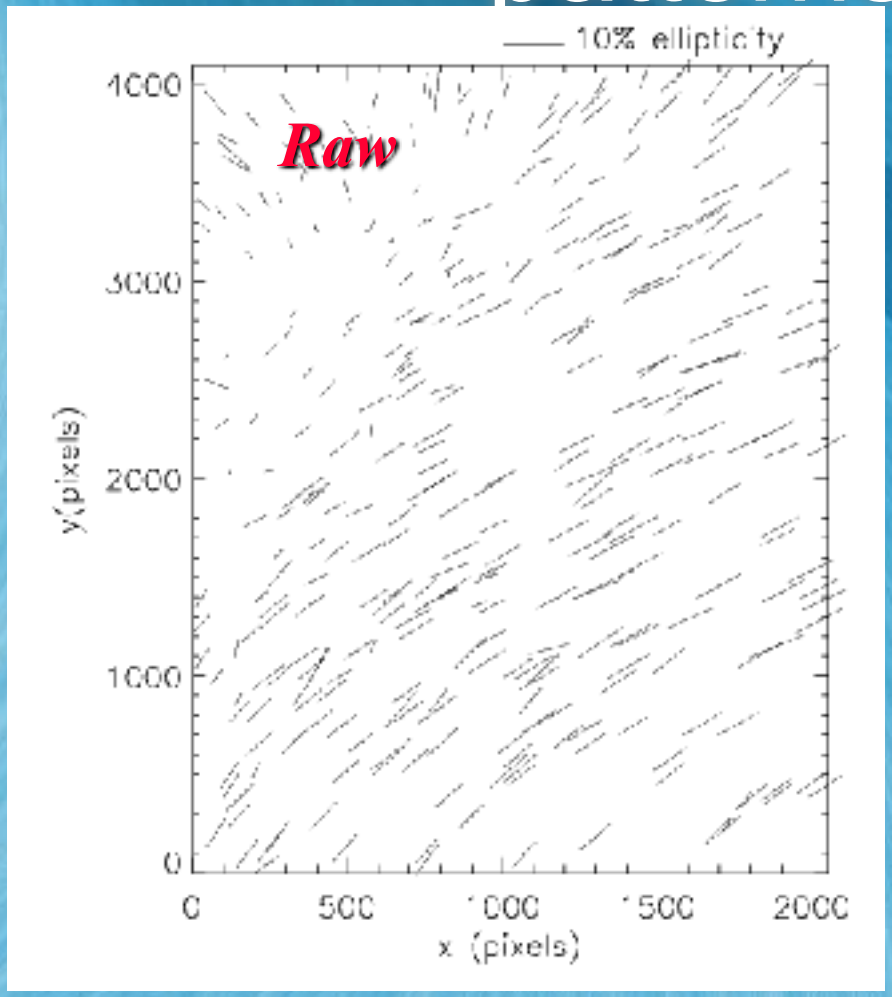

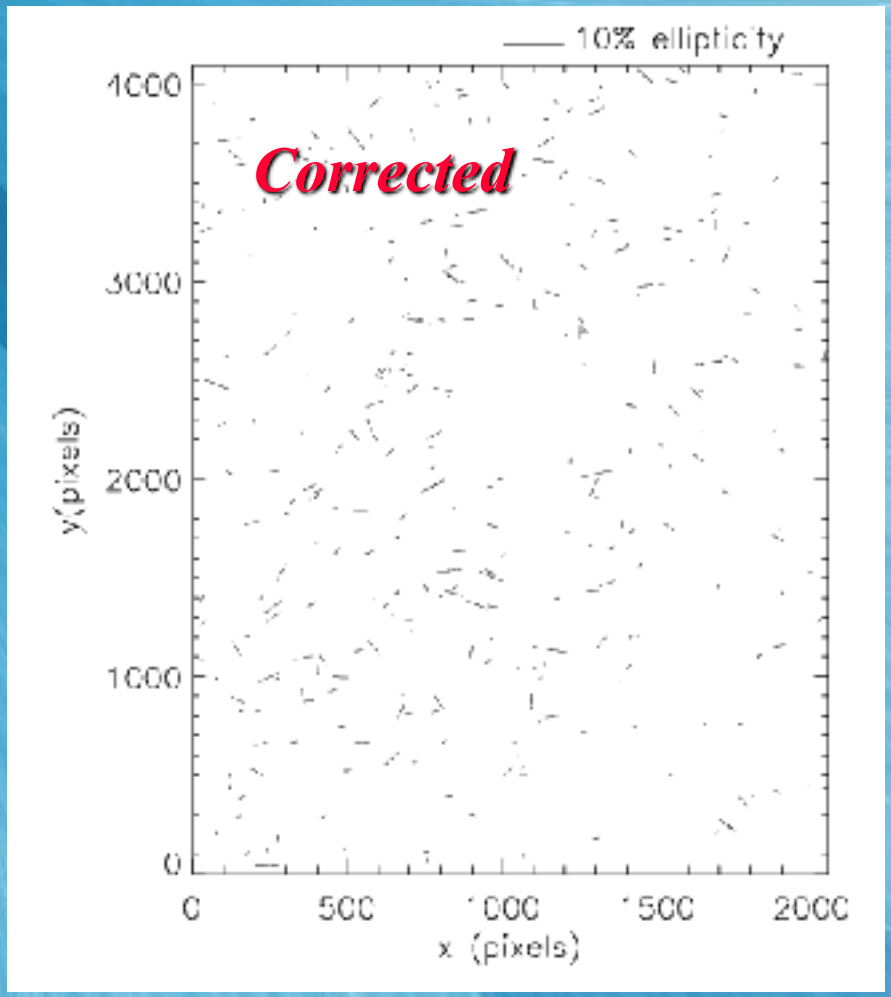

Ground based limits: 3-10% rms reduced to ≈ 0.1%

The most serious systematic: inherent in tracking

First Results with ATCA

5-Antana Interferometer

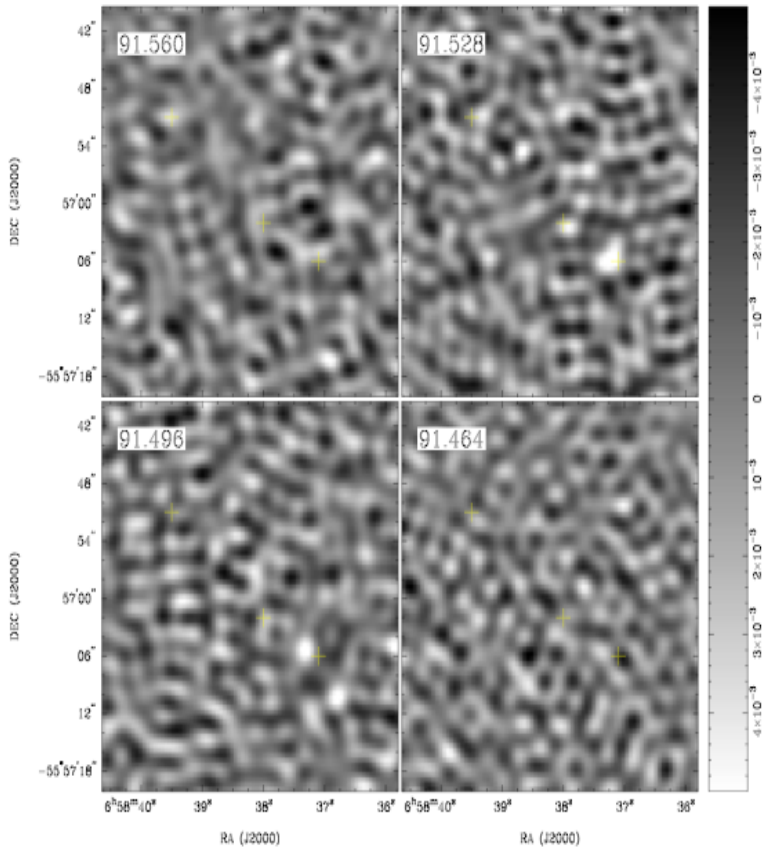

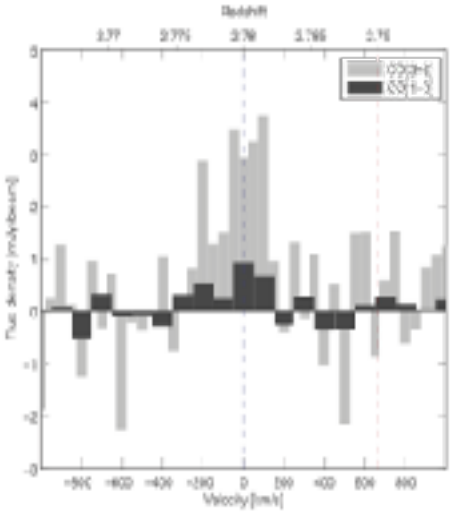

FIGURE 1: CO(1–0) and CO(3–2) spectra as function of velocity and redshift, showing that both emission lines originate from gas at the same systemic velocity. The blue dashed line indicates the derived redshift $z = 2.78$ which is different from that of Gonzalez et al. (2010) ($z = 2.78$, red dashed line). The velocity resolution of the CO(1–0) spectrum is 120 km s^{-1} and that of the CO(3–2) spectrum is 60 km s^{-1}.

Conclusion

- Clusters of galaxies acting as gravitational lenses are allowing us to explore the formation of galaxies at an very large distances and detail.